Published in final edited form as:

Nat Rev Methods Primers. 2021 ; 1(51): . doi:10.1038/s43586-021-00047-w.

Atom probe tomography

Baptiste Gault[1,2,✉], **Ann Chiaramonti**[3,✉], **Oana Cojocaru-Mirédin**[4], **Patrick Stender**[5], **Renelle Dubosq**[6], **Christoph Freysoldt**[1], **Surendra Kumar Makineni**[7], **Tong Li**[8], **Michael Moody**[9], **Julie M. Cairney**[10,11]

[1]Max-Planck-Institut für Eisenforschung, Düsseldorf, Germany.

[2]Department of Materials, Royal School of Mines, Imperial College, London, UK.

[3]National Institute of Standards and Technology, Applied Chemicals and Materials Division, Boulder, CO, USA.

[4]I. Institute of Physics (IA), RWTH Aachen University, Aachen, Germany.

[5]Institute of Materials Science, University of Stuttgart, Stuttgart, Germany.

[6]Department of Earth and Environmental Sciences, University of Ottawa, Ottawa, Ontario, Canada.

[7]Department of Materials Engineering, Indian Institute of Science, Bangalore, India.

[8]Institute for Materials, Ruhr-Universität Bochum, Bochum, Germany.

[9]Department of Materials, University of Oxford, Oxford, UK.

[10]Australian Centre for Microscopy and Microanalysis, University of Sydney, Sydney, New South Wales, Australia.

[11]School of Aerospace, Mechanical and Mechatronic Engineering, University of Sydney, Sydney, New South Wales, Australia.

Abstract

Atom probe tomography (APT) provides three-dimensional compositional mapping with sub-nanometre resolution. The sensitivity of APT is in the range of parts per million for all elements, including light elements such as hydrogen, carbon or lithium, enabling unique insights into the composition of performance-enhancing or lifetime-limiting microstructural features and making APT ideally suited to complement electron-based or X-ray-based microscopies and spectroscopies. Here, we provide an introductory overview of APT ranging from its inception as an evolution of field ion microscopy to the most recent developments in specimen preparation, including for nanomaterials. We touch on data reconstruction, analysis and various applications, including in the geosciences and the burgeoning biological sciences. We review the underpinnings

✉ b.gault@mpie.de; chiaramonti@nist.gov.

Author contributions Introduction (B.G.); Experimentation (P.S., S.K.M., B.G. and C.F.); Results (M.M. and B.G.); Applications (J.M.C., M.M., O.C.-M., A.C., R.D., T.L. and B.G.); Reproducibility and data deposition (B.G.); Limitations and optimizations (B.G.); Outlook (B.G., O.C.-M., P.S., R.D., S.K.M., T.L., M.M., A.C., J.M.C. and C.F.); Overview of the Primer (B.G. and A.C.).

Competing interests

The authors declare no competing interests.

of APT performance and discuss both strengths and limitations of APT, including how the community can improve on current shortcomings. Finally, we look forwards to true atomic-scale tomography with the ability to measure the isotopic identity and spatial coordinates of every atom in an ever wider range of materials through new specimen preparation routes, novel laser pulsing and detector technologies, and full interoperability with complementary microscopy techniques.

Atom probe tomography (APT) provides three-dimensional (3D) compositional mapping of materials with sub-nanometre spatial resolution[1] and, in principle, no lower or upper limits of elemental mass[2]. The mass resolution is generally sufficient to distinguish each isotope of each of the detected elements. This information is used to infer how the distribution of certain elements affects the properties of a material, to guide the design of new materials or to better predict when a material will fail over time in service. It can also reveal the material's history or that of the geological region where it was found. Typical bulk materials have complex, hierarchical structures on multiple scales, as depicted in FIG. 1a. This applies to human-made and natural solid materials — including engineering alloys, semiconductor devices and minerals. In crystalline solids, atoms are organized on a lattice that can be populated by `solutes` substituting for solvent atoms on the lattice or located in between lattice atoms, that is, interstitially. The crystal contains atomic and `microstructural imperfections` including lattice defects such as `vacancies`, `dislocations`, `stacking faults` and `twins`, and `grain boundaries`, as well as `secondary phases and phase boundaries`, or voids, for example. Multiple stable and metastable phases may also be present in the material. In addition, a material has an interface with its operating environment, where a range of interactions can modify the `composition` and microstructure, resulting in, for example, cracks or oxidation. Other materials can be amorphous with different defects. Some devices are fabricated with well-defined structures, such as thin films with stacks of layers of an expected composition and numerous interfaces.

APT stems from field ion microscopy (FIM)[3,4], and, before this, from field electron emission microscopy[5]. The elegance of the FIM and field electron emission microscopy techniques lies in their simplicity: a high voltage applied to a needle-shaped specimen generates an intense electrostatic field — the same effect underpinning the lightning-rod effect[6]. The needle is positioned in front of an ion detector, which can be a phosphorescent screen or a particle detector. A negative electrostatic field can cause the emission of electrons. Reverting the `polarity` enables two distinct phenomena: `field ionization`, whereby atoms near the specimen's surface can be ionized, and `field evaporation`, whereby atoms that constitute the surface of the specimen can be ionized and desorbed. The specimen itself acts as a `projection optic`, with no additional lenses. The charged particles are projected nearly radially during the early stages of the flight, and their trajectory is defined only by electrostatics[7]. The tip-shaped specimen has an end radius typically below 100 nm, which makes the projection highly divergent and provides a magnification in the range of 10^6. Interatomic distances, typically 10^{-10} m, hence become 10^{-4} m, which is discernible by the human eye. FIM provided the first direct images of surface atoms in the 1950s[8]. The atom probe combined this imaging with a `time-of-flight mass spectrometer`[2] to provide analytical capabilities. The name 'atom

probe' was seemingly coined as a counterpart to another materials analysis technique, the electron probe microanalyser, which uses X-rays to provide micrometre-scale compositional mapping. However, 'atom probe' is misleading; the ions that allow us to probe the material are the primary beam produced by and from the specimen, whereas other techniques typically have an external primary illuminating source, for instance light or electrons in the most common microscopy techniques. Early atom probes allowed for depth profiling[9]. Step-changes in the design[10,11] led to the '3D' or 'tomographic' atom probe, with the implementation of a position-sensitive detector[12,13]. Thorough historical perspectives are available on the development of the technique[14,15].

Not all microstructural features can be analysed by APT. Primarily a compositional mapping tool, crystallographic lattice features such as vacancies and structural defects such as dislocations, faults and boundaries cannot be readily imaged. However, chemical segregation leading to compositional heterogeneity at these structural defects often reveals their presence[16–20]. The strengths of APT complement other microscopy and microanalysis techniques. Among a wide arsenal that allows for nanoscale imaging and analysis, FIG. 1b maps some techniques that are commonly used with APT, along with the typical imaged/analysed feature size and compositional sensitivity. In FIG. 1b, between scanning electron microscopy (SEM) and (scanning) transmission electron microscopy ((S)TEM), with energy-dispersive X-ray spectroscopy and electron energy loss spectroscopy, and secondary-ion mass spectrometry (SIMS), APT occupies a unique space in terms of combining a high sensitivity in the range of tens of parts per million and a feature size below 1 nm. APT is also inherently 3D, which is not the case for the other techniques shown in FIG. 1b.

The higher throughput and wider applicability in APT instrument design, as well as improvements in specimen preparation and transfer techniques, has led to an international expansion of APT, with 100 equipped groups in 2020, at shared facilities across the world[21] and at internationally leading materials companies. In this Primer, we cover the fundamentals of the technique, specimen preparation and data processing, show examples of applications and discuss reproducibility issues and the intrinsic limitations of the technique. We finish by discussing prospective new technique developments and the research frontier of the burgeoning cryogenic APT for the fields of soft matter and liquids.

Experimentation

This section describes the general aspects of atom probe experimentation. It covers the set-up contained in the ultra-high vacuum chamber, some of the practical aspects of the fundamental scientific principles enabling the technique and the preparation of specimens suitable for atom probe analysis.

Atom probe design

There are numerous common traits in the design of modern atom probes (FIG. 2a). Here, we describe some generalities as review articles and textbooks are available for more details[14,15,22,23]. The analysis takes place in an ultra-high vacuum chamber, with pressures in the range of 10^{-8} to 10^{-9} Pa. The specimen is mounted on a stage that is cooled to

cryogenic temperatures in the range of 20–80 K, typically by the combination of a cold finger at the end of a closed-circuit helium-based cryogenic cooler with a resistive heater that regulates the temperature. The stage holds the specimen in front of a counter-electrode located a few tens of microns to a few millimetres away and is connected to a direct current high-voltage power supply, commonly of up to 15 kV. In the most frequently found commercial design, the local electrode atom probe (LEAP)[22,24], the stage can move in three dimensions to facilitate specimen alignment in front of a microelectrode with an aperture diameter of ~40 μm. Prototypes using a similar assembly had previously been designed[25,26], but the high throughput of the LEAP instrument, which allows for loading multiple specimens at once to analyse them successively, significantly facilitated the spread of the technique. Note that commercial equipment is identified here to adequately specify the experimental conditions and does not imply any endorsement by the National Institute of Standards and Technology (NIST) that it is the best for the purpose.

The field evaporation and subsequent measurement of the time of flight of each ion is triggered either by pulsing the high voltage (to vary the electric field) or by laser pulses (to vary the temperature). In the former case, negative high-voltage pulses lasting a few nanoseconds[27,28] with an amplitude of 10–25% of the applied direct current voltage are transmitted onto the counter-electrode. In the latter case, a pulsed-laser beam is focused towards the specimen apex. Whereas early designs of atom probes used a nanosecond pulsed laser[29,30], state-of-the-art instruments use pulses in the picosecond to femtosecond range[31–33] with wavelengths typically in the near-ultraviolet (near 350 nm). Research instruments can also be equipped with laser sources with a variable wavelength[34,35].

Beyond the counter-electrode on the path of the ions, ion optical devices are sometimes used[36,37], with the most popular so far being the reflectron[38–40]. A reflectron is the equivalent of an electrostatic mirror that bends the ion trajectories, as shown in FIG. 2b. It offers the possibility to extend the time of flight of the ions and, hence, the relative precision of the measurement and the mass resolution[41].

Finally, 10–50 cm away from the specimen is the single-particle `delay-line detector`, which combines an assembly of microchannel plates and an anode. The microchannel plates convert the impact of a single ion into hundreds of thousands of electrons[42]. The anode collects the electrons and, on state-of-the-art atom probes, contains three delay lines[43,44]. The electronic signals detected at each end of each delay line are processed to calculate the impact position. In cases where multiple ions strike the detector nearly simultaneously, the signals from the third line are used to help disambiguate the signals on the other lines to maximize the accuracy of the positioning information recorded[43]. The processing of the signals, their recording and the association of an impact position with a time of flight for each detected ion are done digitally, either during the acquisition or during post-processing of the data.

Field evaporation

Metals.—APT is underpinned by the fact that an intense electrostatic field can cause the desorption and ionization of atoms from the surface of a material in a field evaporation process[45,46]. This requires that a critical field, termed the evaporation field, is reached.

Field-evaporated ions are accelerated by the electric field away from the specimen's surface. Field evaporation is primarily a thermally assisted process[47], even though there have been reports of field evaporation via an ion tunnelling process[48]. The prevalent theory states that the departing ion is singly charged and, during the early stages of the flight, is further ionized as one or more electrons tunnel back into the specimen[49] (FIG. 2c). The probability of these post-ionization events is directly related to the successive ionization energies of each atom and the strength of the electric field. The ratio of the charge states of the various species present in the specimen can therefore be used as a proxy to estimate the intensity of the electric field[50–53].

Non-conductors.—The mechanisms discussed above have been established in the study of metals. Several differences appear in semiconductors and insulators (BOX 1; FIG. 2d). One difference is a high fraction of multiple events where more than one ion is detected after a single high-voltage or laser pulse, with these multiple events having two origins. First, following the field evaporation of a surface atom, the charges at the surface rearrange to maintain the screening of the electrostatic field, as recently imaged by FIM[54], which can lead to the rapid field evaporation of neighbouring atoms. This seems to occur more for materials that are less electroconductive, which may be due to differences in carrier density or mobility. For some semiconductor materials, for instance thermoelectrics, the proportion of multiple events was extraordinarily high[55,56], suggesting that materials properties play a crucial role in how the bonds break during APT experiments. Second, the high fraction of `molecular ions` increases the likelihood of dissociation.

Advanced analyses of the APT data containing a high proportion of molecular ions and/or multiple events can provide information about which species are most susceptible to simultaneous evaporation and information about dissociation pathways[57,58]. These issues affect, for instance, carbides[59], leading to known issues in the quantification of carbon in steels[60]. These analytical problems arise as a result of the functional properties of the surface, such as the band gap, low effective mass of electrons or high anharmonicity of chemical bonds (equivalent to a high Grüneisen parameter), in part modified by the intense electrostatic field.

Whereas many details of the physics of the field evaporation of insulators and semiconductors remain elusive, there are indications[61,62] of similarities with processes in metals. Although maybe not quantitatively transferable, the dependencies of the charge states of the emitted ions as a function of the electric field[30,63,64] and the relative stability of molecular ions[65] appear to follow the same trend.

There are numerous reports of the influence of the field evaporation conditions on the resulting analytical performance of APT[64,66–70], and in BOX 2 we provide some guidelines to help optimize data quality.

Specimen preparation

From bulk materials.—The preparation of specimens suitable for APT can be seen as a (dark) art. Field ion evaporation requires electrostatic fields in the order of ~10 V nm^{-1} in order to selectively and sequentially remove surface atoms. To achieve the fields required,

atom probe specimens are formed in the shape of a sharp needle, with an apex radius in the range of ~100 nm. An analytical model, $F = V/kr$, relating the surface electrostatic field, F, to the end radius, r, and applied voltage, V, through a field reduction/field factor, k, has been derived from simple electrostatics[6] and typical k values ranging from 2 to 8 (REFS[71,72]). A modest applied high voltage, in the order of 10^3 V, can be used achieve the necessary electrostatic field. Historically, before the advent of focused ion beam (FIB) milling systems, metallic specimens were prepared from a wire or a small matchstick-shaped blank and turned into a needle by electrochemical polishing with various alkaline or acidic solutions[73,74], or, specifically for noble metals, molten salts[73]. The blank is moved through a thin layer of the solution in order to progressively reduce the cross-section. At the point of rupture, the end radius or tip apex was often below 100 nm. Targeting specific microstructural features, however, was challenging and could only be achieved via successive observations by transmission electron microscopy (TEM) followed by pulsed electropolishing, for example[75,76].

Instrumental to routine targeted preparation was the development of liquid-metal ion sources[77] and the development of dual-beam SEM/FIB systems, which are now used to prepare multiple site-specific atom probe specimens in a single session[78]. SEM is used to identify a region of interest and the FIB is used to is prepare the specimen itself. The current established protocol is briefly outlined in FIG. 3a and discussed as follows: first, a cantilever 15–20 μm long is cut with the FIB from the material sample's surface; second, using the in situ gas injection system, the micromanipulator is attached to the wedge, which is cut free and lifted out; third, the wedge is attached to a support, most often a `micro-tip coupon`[79] or a TEM half-grid, and sliced; fourth, each slice is then turned into a needle-shaped APT specimen through a series of sequentially smaller annular milling routines in the FIB. The final end apex radius is approximately 100 nm depending on the material of interest. Whereas FIBs typically use a liquid-metal gallium source, plasma-based sources have been used with increased success[20,80–82]. Alternatives and variations around this principle have been proposed and are thoroughly reviewed elsewhere[83,84].

For site-specific sample preparation, microstructural features of interest are identified by using, for instance, backscattered imaging, electron backscattered diffraction, electron-channelling contrast imaging or energy-dispersive X-ray spectroscopy in the SEM system[85]. Additional information can be gathered by inspecting the APT specimen by TEM[86] using an appropriately-sized TEM grid as a support[87], as outlined in FIG. 3b. In this case, a feature is identified by SEM and marked by electron beam or ion beam deposition inside the SEM/FIB system. The marked region is extracted, and a slice is attached to a partly electropolished half-grid[88]. The slices are sharpened and the feature of interest positioned within 200 nm of the apex. The final specimens are subjected to milling with a low acceleration voltage (2–5 kV) to remove the regions of the materials damaged by the energetic incoming ions.

From nanostructures.—APT analyses of nanostructures such as nanoparticles or nanowires require dedicated specimen preparation approaches[89]. Direct deposition of nanoparticles onto pre-sharpened specimens in vacuum[90] or electrophoresis in solution[91,92] has led to successful analysis. The second approach is illustrated in FIG. 4a, where the

specimen is inserted into a drop of solution containing nanoparticles and, by applying voltage pulses, negatively charged nanoparticles are attracted to the positively charged needle. The number of deposited layers is controlled by adjusting the concentration, pulse amplitude or duration. TEM shows one to two layers of nanoparticles deposited on the support needle in FIG. 4b. This method is suitable for nanoparticles of 1–60 nm and is limited by the size of the support needle. FIGURE 4c exemplifies successful APT analyses of silver atoms of 8–10 nm (in grey) forming the core of nanoparticles and palladium (in yellow) forming a shell, with two different sets of nanoparticles imaged with various core-shell thicknesses. A range of other nanostructures have been successfully analysed following this preparation approach[91,93–95]. The main drawback is a low yield and poor data quality because the particles are only loosely bonded to the support needle and complete nanoparticles can simply detach. A similar method based on the use of a pre-sharpened metallic needle has enabled the analysis of various materials ranging from metallic multilayers[96,97] to polymer films[98] or self-assembled monolayers[99,100].

Flat-top silicon micro-tips, individual needles or TEM half-grids have been used as supports with, for instance, a single nanoparticle or nanowire placed on the surface using a micromanipulator or a microgripper to grab individual[101,102] or agglomerated[103] nanoparticles (FIG. 4d). Nanowires have been grown[104,105] and particles deposited by inert gas condensation directly on coupons or flat substrates with a geometry suitable for APT[106,107] (FIG. 4e). Subsequent deposition of a protective metal film such as chromium or platinum can help ensure adhesion during preparation and analysis[101,108] and prevent damage from the gallium ion beam. The methods shown in FIG. 4a–e enable the analysis of complete nanoparticles. However, agglomerated particles can simultaneously evaporate, causing problems with the APT data reconstruction and interpretation, and they are not amenable to all particle sizes or composition. So far, the community has not established clear guidelines regarding which approach to use to obtain optimal results for a specific sample nature and geometry.

An alternative approach is to embed spatially separated nanoparticles in a metal or oxide matrix and then prepare the specimen by traditional FIB lift-out. In FIG. 4f, a drop of a diluted solution containing nanoparticles is deposited on a flat substrate, subsequently coated with a metal film and, finally, lifted out by a FIB. Here, the wedge is rotated by 90° to prepare the APT specimen with the particle/substrate interface aligned along the specimen's main axis[109]. This method has enabled analysis of silica-supported (SBA-15) particles and carbon nanotubes[110–114]. However, sputter or electron-beam-assisted deposition often leads to a non-conformal coating that may leave voids at the interface between nanoparticles and substrate, which lowers the specimen survival rate and can lead to severe trajectory aberrations in the reconstructed data[115]. Larson et al.[115] used atomic layer deposition to produce a void-free and highly conformal film to sandwich nanoparticles (FIG. 4g) followed by lift-out and sharpening (FIG. 4h). Kim et al.[116] used electrodeposition to embed the nanoparticles in a metallic matrix (FIG. 4i): FIG. 4j shows a TEM image in which palladium nanoparticles were successfully embedded in a nickel matrix and no voids were observed, and FIG. 4k shows the corresponding APT data set. This approach is versatile and has enabled the analysis of nanosheets[117], nanowires and nanorods[118] as well as nanoparticles. However, it may not be as advantageous for surface-sensitive nanoparticles

as the techniques shown in FIG. 4f,g: the solution used for the electrodeposition can then react with the surface and modify the nanoparticles.

Recent instrument design developments

Most atom probes in operation worldwide are commercial instruments. CAMECA currently leads the market with the LEAP and, to a lesser extent, the EIKOS series. A start-up company (INSPICO) has recently started commercially manufacturing instruments. Some groups develop their own instruments for a bespoke set-up or to pioneer the implementation of new capabilities such as detectors or extreme vacuum levels, for instance. Since its introduction in 2015, the current leading commercial instrument is the LEAP 5000 series. This combines the `local electrode` concept with a micrometre-size laser spot size, with 10-ps laser pulses in the near-ultraviolet (355 nm) to minimize thermal tailing effects, as already demonstrated in the earlier generation LEAP 4000 instrument. The current detection efficiency, defined as the fraction of field-evaporated ions that are detected and counted, reaches 80%. The voltage pulsing repetition rate reaches 500 kHz, and in laser mode 1 MHz, promising faster measurements. In reality, the evaporation behaviour of the material and the geometry of the specimen dictate the optimal conditions and, hence, acquisition time.

APT specimens are small, with a high surface to volume ratio, and materials can be reactive so their transport through air can modify their composition and change their survivability during the analysis. Worldwide, there are increased efforts regarding sample preparation, transport, processing and handling in protective atmospheres or under cryogenic conditions. This was, in part, inspired by approaches developed in the biological sciences where the sample environment can be crucial. These new workflows are particularly critical, for example, for liquid materials or air-sensitive samples likely to react with oxygen, and involve cryogenic vacuum transfer solutions. Custom-designed or commercial (Leica, Quorum, Ferrovac) enclosed, controlled environmental transport systems, termed ‘suitcases’, have been adapted or developed to enable controlled specimen transfer into the atom probe[119–121] from the FIB. These suitcases can reach high or ultra-high vacuum conditions and can typically be cooled down to liquid nitrogen temperature. These cryogenic capabilities have enabled the analysis of hydrogen/deuterium-charged specimens[120,122,123], frozen liquids[124,125] and hydrated porous specimens[126]. There are also reports of the importance of using cryogenic cooling during the final stages of specimen preparation[127–129] or for full lift-outs[126,130] to avoid introduction of spurious species and limit damage, or to maintain sample hydration. These approaches fit within the effort to facilitate correlative microscopy (BOX 3), which combines specific techniques to deliver a more complete set of information on a material, and thereby enable scientists to derive well-founded conclusions.

Results

Following specimen preparation and setting up the experiment in order to perform an APT analysis, the collected data need to be extracted and processed. The raw data consist of a sequence of 2D detector–space coordinates, and the corresponding time of flight of every ion is measured over the course of the experiment. This section goes step by step into

the data ‘reconstruction’ process to transform the raw data into a real-space point cloud representation of the specimen, within which both the 3D position and the chemical identity of every detected ion have been determined. The processing of the data is similar on commercial and bespoke instruments.

Mass spectrometry

The first step in the data processing workflow is to assign a chemical identity to each ion. The time of flight can be converted into the mass to charge state ratio through a simple equation relating the kinetic energy of the ion, $1/2mv^2$, to its potential energy, neV where m is the mass, v is the ion velocity, n is the unit charge of the ion, e is the elementary charge of an electron and V is the applied acceleration voltage. At a given acceleration voltage, an ion’s kinetic energy is related to its mass (a heavy ion travels more slowly than a lighter ion) and its charge (a doubly charged ion acquires twice the energy of a singly charged ion). A couple of calibration and correction steps for the difference in flight length as a function of detector coordinates are commonly applied[131]. A histogram, better known as a mass spectrum, is generated; an example for a steel sample is shown in FIG. 5a,b. Each peak or series of peaks is related to the detection of specific types of ion. Each peak in the mass spectrum, and therefore every detected ion contributing to this peak, is assigned a chemical identity. This process is known as `mass peak ranging`. The boundaries (lower and higher mass to charge values of each individual mass peak) are defined to associate a range of mass to charge with a single element or a combination of elements, and the discrete counts in the peak are then calculated through integration[132]. Ranging allows for measuring the composition, and each ion that has been identified is assigned a certain volume to contribute to the 3D reconstruction.

The resolution is such that individual isotope peaks are routinely resolvable. The ability to resolve different isotopes and to locate them individually within the microstructure also enables some unique insights into various investigations, such as the age and history of ancient geological materials[133] or the role of irradiation-induced transmutation in the microstructural degradation of components in nuclear reactors[134,135].

Typically, ions are detected in the 1+ or 2+ charge states, but higher charge states can also be observed depending on the element and the intensity of the electric field[49]. Molecular ions are also commonly detected. For example, in the mass spectrum resulting from the analysis of a steel shown in FIG. 5a, $^{12}C_2^{2+}$ and $^{56}Fe^{14}N^{+}$ are observed. In most cases, all isotopes are expected to be detected in their natural abundances. However, rare exceptions may exist for elements that have undergone biotic fractionation or elements subject to nuclear reactions. Detection of higher charge states and complex ions complicates the ranging process as it increases the likelihood of peak overlap, because the detection of two or more distinct types of ion with the same mass to charge state ratio will contribute to the same peak in the mass spectrum. For example, in FIG. 5a (inset), the peak at 14 Da could potentially be assigned to $^{14}N^{+}$ or $^{28}Si^{2+}$. If this peak was to incorporate only silicon, then we would also expect to see adjacent peaks at 14.5 Da and 15 Da corresponding to $^{29}Si^{2+}$ and $^{30}Si^{2+}$, and expect that the ratio of the peak heights to one another would match the ratio of their respective natural isotopic abundances. Such isotopic fingerprints provide

confidence that peak identities have been correctly assigned during the ranging process. Furthermore, the existence of adjacent peaks owing to the detection of isotopes provides a route for estimating the relative contributions of different ionic species to the same overlapping peak[136]. Additional discussion on these aspects can be found in the Limitations and optimizations section.

3D reconstruction

APT, like FIM, is a point projection microscope, wherein the specimen acts as the projection optic, with no additional lenses. The typical configuration of the atom probe is depicted in FIG. 5c: ions are emitted by the specimen with a radius, R, of less than 100 nm, and fly over a distance, L, of between 80 and 200 mm to the detector with a diameter of 35–90 mm. The trajectory of the evaporated ions towards the detector is determined by the electric field generated by the specimen and is therefore influenced by the electrostatic environment, which includes both the surrounding instrumentation and the shape of the specimen itself. Although initially near-radial, the ions' trajectories are curved towards the centre of the detector and the projected image is subject to what is known as `image compression`. Importantly, provided that the ions fly in a field-free tube, the trajectory of the ion is not dependent on the ion's mass or charge, or the specific value of the voltage[7]. The resulting magnification onto the detector is in the order of 10^6. Multiple projection models have been shown to reflect well the imaged emitter's surface onto the detector, including a `quasi-stereographic projection` and azimuthal equidistant projections[137–139]. FIGURE 5d shows the results from projection models used to describe the ion projection in APT. Ultimately, the interest of using a projection law is that it is not necessary to calculate the trajectory of each ion from the detector back to the specimen, and one can then use one of these projection laws as an approximation to relate a set of detector coordinates $(X_{\mathrm{D}}^{i}, Y_{\mathrm{D}}^{i})$ to a unique position at the specimen's surface. Even though it is not the most accurate[137,139], the most commonly implemented projection is quasi-stereographic, and the image compression factor, ξ, is experiment-dependent with a value generally between one and two (REFS[72,140,141])

Assuming a projection model, the generation of the 3D atom by atom images is a two-step process. First, based on their impact coordinates, each ion striking the detector $(X_{\mathrm{D}}^{i}, Y_{\mathrm{D}}^{i})$ is 'de-magnified' using a reverse-projection model to position them back to their original real-space location within the specimen (x^i, y^i, z^i)[141,142]. The key assumption of the current implementations of the reverse-projection approach is that the geometry of the atom probe specimen always takes the form of a perfect hemispherical cap on a truncated cone and that the radius of this cap is known at every point in the experiment. As material is removed from the specimen during the experiment, the tip becomes increasingly blunt. The implication is that the magnification is not constant throughout the analysis and that the accurate reverse projection of each ion from detector space to real space requires an instantaneous estimate of the end-form radius of the specimen at the moment of every detection event. This is usually achieved either by monitoring the evolution of the voltage applied throughout the experiment, given that $R^i = V^i/(Fk)$, or by using an assumed specimen shape to derive an estimate of the contribution of each ion to the blunting of the tip[141,143]. Either of

these approaches involves several parameters, such as the strength of the field, F, and the geometric field factor, k, or the shank angle of the specimen.

The second step is the calculation of the depth coordinate. The conventional algorithm assumes that the first detected ion is evaporated from a hemispherical surface, $R^{i=1}$, and that the depth of this emitting surface moves down by an increment $\Delta_z^{i=1}$ that is proportional to the volume occupied by an individual atom within the material's lattice[141,142]. The need to assign a realistic volume is why the ions must each be identified through ranging prior to reconstructing the point cloud. Indeed, a volume is assigned to each detected and ranged atom, and that volume is considered proportionally larger to account for the limited detection efficiency. The depth increment represents the thickness of the volume of the preceding detected atom if spread across the entire surface of the specimen that is within the field of view of the detector. In general, for the ith detected ion, this increment is additive, incorporating contributions from every previously detected ion in the sequence. Finally, the z coordinate of an ion is the cumulative sum of these increments added to the z position from the reverse projection. This is summarized in Fig. 5e.

Calibration, or incorporation of physical data about the specimen obtained through a correlative or complementary technique, plays an important role in ensuring the accuracy of subsequent spatial measurements made within the APT reconstruction (BOX 4). This is especially important as there is not necessarily a unique set of reconstruction parameters leading to a specific reconstruction. An example of a reconstruction is shown in FIG. 6a, where elemental identity, in this case aluminium, zirconium, magnesium and copper, was first assigned through ranging of the mass spectrum. The point cloud was then built and calibrated based on the known spacing of the (002) planes in one of the grains.

Data visualization and analysis

Visualization of APT reconstructions can offer immediate and striking insights into the microstructure of a complex material. For example, the points pertaining to atoms of different species can be selectively displayed to reveal their respective spatial distribution, as shown in FIG. 6b where chromium partitioning to the γ phase and aluminium to the γ' phase can be seen visually. Following the reconstruction process, some of the most unique and powerful analyses that can be undertaken have roots in the fundamental nature of the 3D atom by atom APT reconstructions. For example, changes in chemical composition can be characterized along a specific direction within a region of interest in order to calculate a 1D composition profile, for example to quantify segregation at a microstructural feature of interest such as a grain boundary, as seen in FIG. 6c. More advanced APT data analysis can be broadly divided into two classes based upon either `voxelization` of the data or the interrogation of interatomic distances.

Voxel-based methods.—Voxel-based methods segment the data set into an array of cubes of equal volume or number of atoms. The content of each voxel is then inspected, enabling a wide variety of visualization and analysis. Possibly the most commonly used voxel-based analysis is the `iso-surface` that links together an array of adjacent voxels based on a threshold criterion. Two examples are displayed in FIG. 6b for aluminium

and boron. The threshold can either be a molar fraction or a number density of a chosen element (or elements)[144]. A molar fraction threshold leads to an `iso-concentration` or composition surface encompassing regions within the point cloud that contain more than a certain molar ratio expressed in atomic per cent, whereas an element number density threshold is an iso-density surface expressed in atoms per cubic nanometre. The type of iso-surface and the value of the threshold are selected by the user based on what they wish to visualize. Features revealed by iso-concentration or iso-density surfaces may not be similar. In particular, variations in point density are typically associated with local magnifications (see below) and, hence, with microstructural features that do not necessarily show compositional variations, for example grain boundaries[145,146]. With careful adjustment of the threshold, the user can define the interface between contiguous microstructural regions, for example a second-phase precipitate and the surrounding matrix, or two adjacent layers in a multilayer device. This provides a means to both isolate regions of the data for more targeted analysis, as shown in the inset of FIG. 6d, and characterize the chemistry at and in the vicinity of the interface. Statistical measurements, such as voxel-concentration frequency distributions, can also identify and, to some extent quantify, subtle chemical inhomogeneity within the microstructure[147–149].

The compositional evolution of interfaces delineated by iso-surfaces can be derived from a profile calculated in the form of a proximity histogram, better known as a proxigram[150,151], which represents chemical concentration as a function of the distance normal to the iso-surface. The proxigram shown in FIG. 6d provides similar information to that of a 1D composition profile but facilitates the analysis of curved and/or enclosed interfaces. This approach is not without issues[152] but it readily enables an average measurement across numerous disconnected surfaces such as a population of second-phase precipitates. Concentration profiles can be further extended to actually quantify the elemental excess number of atoms segregated to a surface[153,154]. Voxelization also provides a means to create a 2D map or 3D visualization of how concentration and density fluctuate throughout the reconstruction. To this end, a fixed voxel size can be advantageously replaced by local meshing on which the composition or excess can be efficiently mapped[155,156], revealing and quantifying patterns in the segregation that can be associated with grain boundary curvature[157], faceting[19] or the presence of linear defects at low-angle grain boundaries, for instance[158].

Interatomic distance-based methods.—Other approaches involve the direct measurement of interatomic distances and enable the interrogation of the local neighbourhood surrounding each atom. The simplest of such analyses is a nearest-neighbour analysis[159,160]. By examining the distribution of distances separating a solute atom from its first, second, third or *n*th nearest solute neighbour, in comparison with the same measurement undertaken on a complementary randomized system, the presence of subtle fluctuations such as the very onset of nanoscale clustering effects[161] (FIG. 6e) and interactions at longer distances can be used to deduce the matrix composition[162,163]. Radial or pair distribution functions[164–166] revealing specific interactions between solutes can also be extracted from integrating the average 3D neighbourhood of each selected solute atom within the reconstruction.

A unique feature of APT is to characterize solute clusters identified based on interatomic distance. The most widely used approach is known as the ‘maximum separation’ algorithm[167,168]. This assumes that the distance separating two nearest-neighbour solutes within a cluster is less than between two nearest-neighbour solute atoms within the matrix. Hence, a maximum distance, d_{max}, can be assigned such that any pair of solute atoms within this separation are considered to be clustered together. Further, if one of these pairs is also clustered to another solute, then all three can be defined as being in the same cluster. In this way, a larger distinct network of linked solutes can be built that, ultimately, defines a population of clusters. This initially excludes solvent atoms from the cluster definition. However, in a second stage these can be incorporated into the analysis in processes known as ‘enveloping’ and ‘erosion’[168,169]. Once clusters have been identified, various measurements can be applied to characterize each one individually in terms of size, shape, composition, structure and so on[170,171]. As such, statistical analyses can be generated to describe a population of clusters and identify correlations between physical characteristics. Typically, a comparison with a randomly labelled data set is needed to differentiate non-random clustering from the clusters that might be expected even if the solute was randomly distributed. Other algorithms have been developed[161,172], underpinned by different cluster definitions based on concentration[173], higher-order nearest-neighbour distances[159,160,174], Gaussian mixture models[175] and more[1,176,177]. These methods have been authoritatively reviewed previously[161,172].

Ultimately, results from applying either of these approaches must be considered very carefully, particularly when claiming quantitativeness and reproductibility[178]. Objectively defining the extent of a nanoscale cluster of atoms within a reconstruction remains a challenge, whichever approach is used. In particular, even though the APT reconstruction can be highly accurate, it is nevertheless both imperfect and incomplete. The inherent premise upon which the approach is based is not amenable to certain situations; for example, delineating the clusters from the matrix becomes difficult if the solute concentrations are relatively close to that of the matrix. The difference in the evaporation field between the solutes and the matrix, and the dependence of this critical field on the local neighbourhood, also introduce aberrations in the trajectories that break neighbourhood relationships. For example, two nearest neighbours at the specimen surface are unlikely to be so in the reconstructed data if they are both high-field solutes[179]. Finally, the main source of error is likely the parameter selection, which has the potential to considerably affect the resulting analysis[180]. Protocols exist, but none is universally applicable or adopted as a community standard. Selecting parameters by defining a heuristic[69,170,181,182], including using statistical methods[175], has been proposed, but the outcome of applying cluster-finding algorithms remains highly dependent on user input and expertise level[178,180]. Alternative approaches using radial distribution functions to extract the typical characteristics of a population of solute clusters or precipitates[183] have also been proposed, with the option to select parameters.

Structural analysis.—For some alloys, the APT reconstruction can retain elements of the crystallography from the original sample[184], as illustrated in FIG. 6a. This partial information appears as sets of atomic planes in certain regions of the data, most often

associated with the projection of lattice planes with low Miller indices parallel to the local tangent to the reconstructed emitting surface. Means to extract quantitative information from this crystallographic information have been developed based on direct Fourier transforms[185], 3D Hough transforms[186,187] and techniques based on radial distribution functions165 including spatial distribution maps (SDMs)[188–190].

The Fourier transform is akin to performing diffraction from the 3D distribution of atoms in the reconstructed volume. It makes use of a voxelized reciprocal space and calculates the contribution of all points in the real space to this particular location in the reciprocal space. The presence of sets of planes results in loci of high intensity in the reciprocal space at a distance to the central spot inversely proportional to the distance in the real space. This approach enables multiple sets of planes to be characterized at once, and the angle between sets of planes can be directly estimated as they are maintained through application of the Fourier transform. The 3D Hough transform provides a similar set of information but is more computationally intensive, as the computation is done completely in real space and looks for planar features positioned at all possible polar and azimuthal angles.

A SDM is built using a sphere, typically 2 nm in diameter, located on a first atom within the input point cloud, and all atoms within this sphere are copied into an output. The sphere is then moved onto the next atom in the input data and these new neighbouring atoms are copied into the output. This procedure is reproduced for all atoms in the input data, and the output hence depicts the average 3D atomic neighbourhood around each atom within the input data set. If the dimensionality of the data was reduced to one, then this would result in a radial distribution function. SDMs are displayed either as a histogram of atomic offsets in z along a specific direction (z-SDM) or as a 2D map showing the average density of atoms within the plane of the reference atoms (xy-SDM). The peak to peak distance in the z-SDM indicates inter-planar spacing and measures the interatomic separation along the direction perpendicular to the planes. Being computationally expensive, SDMs are usually only used in regions of the data where planes are resolvable[188–190]. If angles between a set of planes and a reference plane can be deduced from another SDM implementation[190,191], the procedure is typically not performed because of the computational cost.

The term atom probe crystallography was coined to refer to the use of this type of structural information to provide additional information on the analysed material[158,184]. The main applications of these approaches, in particular the Fourier transform and SDMs, have been to facilitate the calibration of tomographic reconstruction[192] and assess the spatial resolution of APT[193,194]. The high computational cost and mostly manual operations to extract information and interpret the data may explain why the approach is not more widely used despite great potential[191].

Applications

3D compositional data provided by atom probes are highly complementary to, for instance, the high spatial resolution 2D images obtained from TEM. Atomic maps provide valuable information about the common microstructural features in engineering materials, most of which involve variations in the local composition and can often be examined within the size scale of a typical atom probe data set volume. These

microstructural features include precipitates or clusters, solid solutions and/or ordered structures, grain/phase boundaries, dislocations and point defects/vacancies. Numerous reviews detail the applications of APT to characterize, for example, aluminium alloys[161,195], nickel-based superalloys[196–198], intermetallics[199], steel[200,201], high-entropy alloys[202], nuclear materials[203–205] and, beyond metallurgical systems, thermoelectric materials[206], semiconducting devices for microelectronics[207–209] or light emission[210] and geological materials[211,212]. Here, we give some details of what information APT provides in these various contexts.

Solid solutions—With access to a large enough 3D data set, the statistical approaches discussed above provide information on the arrangement of solutes atoms in a solid solution. These insights enable the study of interactions between atoms from a single species or from one species to one or more species. In solid solutions that are not in an equilibrium state, it is common to observe certain species being preferentially located at shorter distance from one another compared with a random distribution, as illustrated in FIG. 6e. There are many examples of the use of APT to study the early stage of decomposition of a solid solution in metals[166,195,213–216] or dopant distributions in semiconductors[160,217,218], sometimes in conjunction with $SIMS_{219}$. Short-range order can be detected in principle, but, depending on the solute concentration, the results may be obfuscated by the effect of the combination of detector efficiency and the spatial resolution within the APT data[1,220].

Precipitation

Precipitation of a secondary phase from a metastable solid solution is a common strategy to modify properties of materials. APT is commonly used to provide the composition of precipitates, as shown in FIG. 6a,b. APT can also be used to study compositional gradients in the vicinity of grain boundaries or interphase interfaces, as in FIG. 6c for instance, which can help to understand their growth or migration behaviour. Differences in the field evaporation properties between the matrix and the precipitate can affect the measured size and composition[221], and should be considered when interpreting data. Gradients can originate from coarse binning of data or from data voxelization[144,152] and, again, great care should be taken during data interpretation. The study of precipitation has been at the core of APT research for decades and many of the aforementioned review articles are focused on this subject.

Grain boundaries and interfaces

Grain boundaries and interfaces are important factors in relating a material’s properties to its microstructure. Their precise influence often depends on their composition, which, in turn, depends on their crystallographic nature[18]. It is common for certain elements to segregate to grain boundaries and interfaces, typically driven by the minimization of the system’s free energy. This segregation can be beneficial or detrimental, depending on the desired set of physical properties. For instance, grain boundaries affect electronic transport and therefore underpin the performance of multi-crystalline photovoltaic materials[222–224] or thin film interfaces. Several studies have focused on using APT in correlation with electron beam induced current[225,226]. APT has also been applied in microelectronics and memory[227–232],

light-emitting devices[233–235], photovoltaics[236–238] or magnetic reading/recording[96,239,240] and thermoelectrics[206,241–243], amongst others.

The inherently 3D nature of APT data offers a unique opportunity for measuring segregation at grain boundaries and interfaces. Targeted analysis provides quantitative information about the extent of segregation either in the form of an atomic fraction or an `interfacial excess`[244]. This is exemplified in BOX 3 (see the figure, parts **a** and **b**) for correlative microscopy in a solar cell material, where grain boundary segregation of sodium passivates the existing detrimental charge defects. This is also displayed in BOX 3 (see the figure, parts **c** and **d**) for an intermetallic phase where the formation of the twin boundary locally changes the composition, thereby modifying the magnetic domain structure and underpinning promising magnetic properties[245]. In FIG. 6c, boron appears almost completely segregated at the grain boundary, and is typically added to nickel-based superalloys to strengthen grain boundaries.

It is possible to map the extent of segregation across certain surfaces[155] in two dimensions and relate it to the grain boundary type[246]. Segregation mapping reveals that, whereas special boundaries such as twins tend to have lower segregation levels than high-angle boundaries, the segregation behaviour at high-angle boundaries is highly spatially variable even across a single boundary[155]. Grain boundaries have a distinct structure and composition, and can undergo phase-like transitions, called complexion transitions, that occur under conditions distinct from phase transformations[247]. Taking advantage of these processes to tailor alloy properties is the focus of much contemporary research[201]. APT, combined with TEM, has been used to identify complexions such as segregation-induced faceting transitions[19,248,249] and spinodal-like fluctuations[250].

Dislocations, stacking faults and twins

Dislocations are linear defects that accommodate strain in crystalline materials. It is common for dislocations to be surrounded by an excess of certain solute species known as a Cottrell atmosphere. The solute can affect the mobility of dislocations and have an effect on the mechanical behaviour. APT provided the first direct observations of Cottrell atmospheres, first for carbon in steel[251] and later in many other systems such as boron in FeAl[252] and arsenic in silicon[253]. A dislocation with segregation is shown in BOX 3 (see the figure, part **f**). Dislocations can also form loops with segregation at specific edges or facets[254,255], for instance. The 3D nature of the data allows the mapping of segregation along the dislocation line[256,257], sometimes referred to as the ‘line excess’. It has been found that this segregation varies along the line of a defect[258], presumably owing to the different local crystallographic environment. The atom probe has also been used to demonstrate the existence of linear complexions — chemically and structurally distinct regions located inside a linear defect[259] — and to study other structural defects, such as stacking faults[260–263], anti-phase boundaries[264,265] or (nano) twins[266–268], and twin boundaries[269–271].

Microstructural degradation processes

An important application of APT has been to understand the microstructural evolution leading to the degradation of a material’s properties that limit their service lifetime, such

as for materials used for nuclear power generation. Handling radioactive materials can be challenging. To shield the user from the source of radiation, dedicated facilities such as 'hot' FIBs and atom probes are available in the UK (Oxford), France (Rouen, CEA Saclay), the USA (Idaho National Laboratory) and Japan (CRIEPI), amongst others. Studies on nuclear materials include the formation of secondary phases in materials already in service or in candidate materials[203,272–274], welds in engineering parts[275,276], and the oxidation and corrosion of pipes and fuel cladding[277–281]. Research in the area of fuel and waste is also burgeoning[282,283]. In these systems, a significant challenge is the detection of very light elements, including helium[284] and hydrogen.

Beyond just nuclear materials, spatially resolved characterization of hydrogen has been a long-standing frontier in microscopy and microanalysis. Hydrogen is known to embrittle and cause catastrophic failure in many materials, but is also a strong focus for clean energy storage and carbon emission-free mobility. However, its distribution within material structures is difficult to determine. Although hydrogen is readily detected in APT, it is challenging to establish whether the hydrogen originates from the specimen itself or is residual hydrogen from within the vacuum chamber. Isotopic labelling has been proposed as an approach to circumvent this issue. Samples are charged with deuterium, which serves as a marker for hydrogen. This approach has successfully detected hydrogen trapping[285,286], although quantification is not straightforward[287] and will depend on the analysis conditions[288,289]. In order to minimize diffusion of hydrogen out of the specimen, it is also necessary to keep the sample cold between charging and analysis. The study of hydrogen by APT has been facilitated in the past few years by developments in specimen transfer under cryogenic conditions. APT has shown that hydrogen can be trapped at grain boundaries, phase boundaries and dislocations[120,122,123,290], and there have been several studies reporting the analysis of hydrides and their growth mechanisms[291–293].

Geology

Whereas early applications of APT to geological materials were studies of metallic meteorites[294] and metamorphic magnetite crystals[295], the technique rose to prominence with its application in geochronology[133,296]. Today, a large proportion of the published work using APT on geological materials falls within geochronology, extraterrestrial materials and economic geology, but the technique is rapidly spreading into a broad range of minerals of interest in chemical geology, petrology, mineralogy and economic geology, as recently reviewed in detail[211,297].

In geochronology, APT is used to investigate the nanoscale distribution of radiogenic isotopes, such as uranium and lead, in accessory minerals (for example, zircon, monazite, titanite, baddeleyite)[133,298,299]. The reliability of accessory minerals as geochronometers relies on the assumption that trace elements diffuse negligible distances through the crystal lattice. Geochronology studies reveal that deformational and metamorphic events can allow the diffusion of radiogenic isotopes, leading to local changes in the isotopic ratios. The diffused atoms form nanoscale clusters[212,300,301], and the characterization of these clusters has the potential to be used to resolve the timing of the cluster-forming geological events. These studies have improved our understanding of the mechanisms for parent–daughter

isotopic mobility and yielded important information about the formation and evolution of the Earth's crust[302].

APT has also been used to study extraterrestrial and terrestrial proxy materials such as accessory minerals from lunar soil samples and meteorites (for example, ilmenite, zircon, baddeleyite, nanodiamonds and refractory metal nuggets) to resolve the timing of planetary events and better understand the formation of planetary crusts[294,303,304]. These works have allowed determination of the timing of lunar transient thermal episodes[305], characterization of the composition and texture of space weathering products[306], constraining the processes driving the migration of early solar system materials in the protoplanetary disk[307] and determination of the astrophysical origins of meteorites[308].

In the field of economic geology, APT has mostly been applied to ore minerals such as pyrite and arsenopyrite to investigate the mechanisms of precious metal and base metal incorporation and mobility[309,310.] The characterization of metal occurrences within their host minerals provides key information for understanding the fluid–rock interactions and crystal growth kinetics[311] that lead to the formation of viable economic deposits. Recent studies that have used APT for the study of ore minerals have made significant advances towards understanding the paragenesis of ore deposits including Carlin-type gold[312], orogenic gold[309], porphyry copper–gold313 and platinum group alloy deposits[314].

Other interdisciplinary studies include investigations on the interaction between trace elements, fluids and crystal defects and their effect on mineral physical properties[315,] characterization of the composition and structure of minerals to understand fundamental processes associated with phase formation in, for example, feldspar[304,316], vapour-phase mineral deposition, glass corrosion and magma unmixing[317,318]. Studies also include assessment of the mechanisms for dissolution/precipitation on mineral surfaces[319,320], element diffusion during deformation, metamorphism and metasomatism used to shed light on interface reactions, and mineral intergrowth and exsolution processes[316,321–326]. These insights can only be gained through APT, with its high elemental sensitivity combined with 3D imaging at sub-nanometre spatial resolution.

Beyond bulk materials

In addition to understanding the structure of the bulk of materials, understanding surfaces is also of great interest especially, for example, for chemical conversion systems such as catalysts and electrocatalysts that are involved in renewable energy generation. Most devices use nanoparticles to increase their surface to volume ratio and maximize their activity. To optimize the catalytic performance of these nanostructured materials, one must have a detailed understanding of the atomic-scale microstructure on surfaces, near-surfaces and where internal defects and interfaces intersect the surface. APT and related techniques have long been used in surface science and catalysis based on the hypothesis that the near-spherical cap at the end of the needle-shaped specimen is akin to an individual nanoparticle327–330. Upon adapting the specimen preparation strategies to protect catalytically active surfaces from ion or electron beam damage, APT can potentially provide the distribution of elements within microporous and nanoporous materials such as zeolites[331,332], metallic–organic frameworks[333] and nanoporous metals[334,335]. APT has also

been used to study the intermediate species formed at the surface of thin-film catalysts at different stages of the oxygen evolution reaction[336–338].

Biological and organic materials

The study of organic matter with atom probes is considered an emerging application area. The most significant contributions to date have been in the study of biominerals, which are solid, mostly inorganic and readily amenable to atom probe analysis, as first demonstrated by Gordon and Joester[339]. Subsequently, atom probe data have revealed the nanoscale distribution of important elements such as magnesium and fluorine in dental enamel[340,341], and have added to the understanding of the nanoscale structure of the shells of marine organisms[342,343] and various studies on apatite, bone[344,345] or biogenic carbonates[346,347].

Soft materials can be much more challenging to examine as they can be unstable in the high-vacuum environments encountered in atom probes and in FIB systems. There have been several reports of the analysis of carbon-based molecules[348–350], polymers[98] and self-assembled monolayers formed directly on metallic specimens[99,100,351,352]. Although interesting results were obtained pertaining to the field evaporation behaviour of organics, much more is required to understand the intricacies of the analysis of organics by APT[353–355].

Soft biological materials are normally hydrated but dried proteins have been deposited and imaged by FIM and analysed by APT, including DNA[356], ferritin[357–359] and amyloid fibrils[360]. Different approaches to maintain the proteins in their pristine, hydrated state include freeze-drying[361], fixing in resin[359,362] and freezing[125,130]. Freeze-drying removes the water and greatly modifies the original structure. Fixing can be an alternative but can alter the sample on a molecular level and disrupt the distribution of ionic species. In an approach similar to fixation, Sundell et al.[363] examined an antibody protein by using a sol-gel method to embed individual proteins in an amorphous solid silica matrix, followed by a standard FIB lift-out. The hydration shell around the molecule was completely replaced with silica and the shape of the features in the 3D reconstructions showed good agreement with the crystal structure in the protein databank. Cryogenic developments for APT specimen preparation and transfer, recently reviewed by McCarroll et al.[364], have the potential for cryogenic preservation. However, more developments are needed to maintain the hydration shell around proteins and determine more specifically what APT can bring to the biological sciences.

Reproducibility and data deposition

Standards and community-led protocols—Although APT is fast-growing, it remains a rather immature field compared with other analysis techniques. Similar to many relatively small communities that grew from isolated groups, defining a common vocabulary across APT researchers is sometimes arduous, and using standard protocols even harder. Nomenclature for the technique itself in published works over just the past 2 years includes 3D-AP, 3-DAP, 3D-APT, TAP, LEAP or AP microscopy, which makes it confusing to outsiders and often confuses the technique with the instrument. This does not happen with TEM, SEM or SIMS. Historically, each group had its own software toolbox. Although

sharing good practice was not prioritized, recently created geology-focused groups365 have published the first article on how to appropriately report APT in scientific publications.

The evolution of the commercial landscape and the fast spread of the LEAP has accelerated the change towards more homogeneity with common tools and an, albeit imperfect, terminology. For example, commercial software is now used by most across the community. In addition, there was a reckoning of the importance of creating active subgroups within the International Field Emission Society (IFES) to build a common structure across research groups, and thus the situation is evolving as we write. For instance, although newly developed tools often are primarily used within individual groups, there are continuous efforts to share tools that are very often open-source and document their usage and application[136,366–371] — a list of software toolsfor APT analysis is available. This is, in part, related to the efforts of the APT Technical Committee. Another example, although in existence for over a decade, is a standards committee to establish a common vocabulary; a first-term compliant definition has been submitted to the International Organization for Standardization (ISO). For those involved, defining one term represents more than 150 emails exchanged over nearly 2 years, giving an indication of how titanic the task will be in the coming years. These efforts will make `round robin experiments` more common. Currently, there are only a few examples[178,372] facilitating exchange of good practice and comparison of results on common grounds and accelerating progress.

There are also critical questions that arise from performing experimental sciences that the APT community has not yet fully addressed. APT is a destructive technique, so we have to assume that the specimen was representative of the material, and when comparing across multiple specimens from different locations in the same sample we must assume that they are similar. There is a need to improve on the statistical analyses of the data and ensure comparability. Experimental set-ups and data outputs are not yet standardized, even though there are efforts in this direction coordinated by the Technical Committee of the IFES, which proposed the use of an HDF5-based file structure (APT-HDF5 file specification).

Although there are currently no minimum reporting requirements when conducting and reporting on APT measurements, some forays have been made in this direction by Blum et al. for geological materials analysed by APT[365], and this part of the community is pushing to establish this as standard practice. It should be emphasized that generalizing this practice would be extremely beneficial to the community as a whole, especially considering the variability in the processed data demonstrated by a recent interlaboratory experiment on a reference zircon[372]. No public or standard location or repository currently exists for APT data, even though there were early efforts by groups in, for example, Sydney[369] and Colorado[373].

These are critical issues that are yet unaddressed and on which the community needs to progress. For example, virtual workshops or dedicated symposia at targeted scientific meetings could encourage the adoption of standard procedures and practices.

Limitations and optimizations

Spatial resolution and performance—APT is often presented as a microscopy technique, so naturally the question regarding its actual spatial resolution arises. For a conventional microscopy technique, the `Rayleigh criterion` is commonly used, corresponding to when the diffraction-limited image of two point sources can no longer be separated. In APT, an equivalent is not, strictly speaking, accessible: the reconstructed position of the ion is subject to error but is not diffraction-limited. Over the years, several criteria have been reported based on a statistical analysis of the reconstructed atomic planes, either in real or reciprocal space[188,193,194,374]. These studies were performed on pure materials, with depth resolutions reported down to 20pm (REF.[375]) for aluminium or 60 pm (REF.[193]) for tungsten, and lateral resolutions in the range of 200pm, with variations associated with the materials[193,194,376] and the set of atomic planes considered, as well as the experimental conditions[194,377].

None of these investigations informs on the smallest feature size that can be confidently analysed, which is more intimately related to the imaging process. The magnification in APT is associated with the distribution of the electrostatic field at scales ranging from the mesoscale to the near-atomic scale, and some aberrations are inherent to the physics of the field evaporation process.

On the mesoscale, the magnification is related to the specimen itself[7] and several projection laws can describe the projection rather well[137–139]. However, the parameters associated with the projection differ from specimen to specimen[378], evolve over the course of an experiment[379] and, ultimately, also depend on the analysis conditions[380]. This is unlike most other microscopy techniques. In addition, as the magnification is related to the local curvature, and the field evaporation probability is dependent on the local atomic neighbourhood, inhomogeneities in the specimen's composition in the near-surface region lead to the development of local curvatures and changes in magnification. This is apparent in experimental detector maps, as shown in FIG. 7a, in which dense regions correspond to precipitates sitting at a grain boundary and within each grain, as delineated by white circles and ellipses. FIGURE 7b explains schematically why the image of a precipitate on the detector can be larger or smaller depending on its evaporation field relative to the surrounding matrix, which leads to compression or divergence of the ion trajectories.

At the near-atomic scale, the distribution of the electrostatic field in the vicinity of the surface is highly dependent on the neighbourhood of the departing partly charged atom or ion[381], which has been studied extensively by electrostatic simulations[382] and density-functional theory-based calculations[383,384.] Gradients of electrostatic field can also modify the path followed by the departing particle, causing, for instance, short-range rolling motion of atoms on their neighbours before desorbing, making the ion start its flight from a close-by position to where the atom initially was inside the material.

These effects combine to blur the atomic positions following reconstruction and result in a limited spatial resolution, which depends on the species considered and on the population of particles that is being imaged. De Geuser and Gault recently reviewed the literature comparing small-angle scattering techniques and APT on a range of precipitate-strengthened

alloys[1]. Small-angle scattering, using either X-rays or neutrons as a source, in principle has no limits to the minimum size of particles that can be detected, and the size distribution extracted from the fitting procedure is not affected by a spatial resolution. The reported feature size by APT and small-angle scattering is plotted in FIG. 7c, along with (in grey) the expected size for an effective spatial resolution of 0.25–1.25 nm. The actual resolution is probably somewhere between these boundaries, but pinpointing to a single value is problematic as it intrinsically depends on the analysed material system, and particularly the size and composition of the microstructural features of interest. Ultimately, the problem does not lie in APT's capacity to detect these particles — ions from these are emitted and detected — but the resolution limit implies that their size and composition can no longer be directly measured.

Interfaces such as grain boundaries are important microstructural feature analysed by APT. There have been numerous studies comparing the chemical or compositional width of an interface with its structural width, which may be different. Structural discontinuity was shown to introduce trajectory aberrations even without segregation[145,146]. Correlative studies with TEM performed directly on an atom probe specimen[18], including at high resolution[19], have highlighted that the common assumption of a width of 0.5 nm is close to the values obtained from experiments only for the structural width of a boundary. Recently, APT measured segregation of a similar width for a transformation interface analysed along a specific set of atomic planes[154]. Yet, typically, the chemical widths of grain boundaries and interfaces very even along a single boundary[385–387], and the limited spatial resolution of APT can limit the precision of the measurement to 1–2 nm full width at half-maximum[154].

Sensitivity and analytical performance

APT is a mass spectrometry technique, which naturally leads to the question of its sensitivity and the precision of the measured composition. There have been efforts in recent years to define statistically meaningful metrics to assess APT sensitivity[23] but they have not been adopted across the entire community. Here, we only discuss some aspects affecting the sensitivity without dwelling on a specific metric, to give a sense of the important parameters that need to be monitored.

More conventional mass spectrometry techniques, such as inductively-coupled plasma mass spectrometry or SIMS, typically analyse large volumes of materials of several cubic microns to cubic millimetres, and hence contain more than 10^9 ions. APT volumes are minuscule in comparison, with ion counts in the tens to hundreds of million ions. This is a first limitation when looking for trace elements (see additional discussion of limitations to species detection in BOX 5). When these are agglomerated within the material, their local concentration can be high enough to be detected.

Error estimations

There are numerous reports of imprecisions in the composition, and species-specific losses, when comparing the overall composition from APT with that obtained from other bulk techniques[60,66]. The precision is often assumed to simply be that of the counting statistics — the larger the measured number of ions N, the more precise the measurement:

$$\sigma_i = \sqrt{\frac{C_i \times (1 - C_i)}{N}}$$

where σ_i is the precision and C_i is the atomic fraction of element i. When it comes to reporting the local composition, for example in a profile, only the counting statistic is typically quoted for precision. Danoix et al.[388] showed that the detection efficiency could be accounted for, but would not change the error estimation if it is assumed to be the same across all species, which is an approximation. There are also known dependencies of the measured composition on the experimental conditions, which can often be traced by changes in the electrostatic field[66,67,389]. This can become crucial when considering error estimations, for example when reporting on the concentration of hydrogen within materials[289,390.]

As per the spatial precision, there have been reports and discussions on the possible migration of atoms at the surface prior to field evaporation on a local scale[46,47] or at the mesoscale[391,392], as well as high-field solutes being retained on the surface while neighbouring atoms from multiple lower layers field evaporate[393,394]. However, data representation continues to be based on a point cloud that implies an almost infinite precision of the reconstructed position. Most composition profiles will only display errors for the composition and not for the measured distance, which is problematic, particularly as some of the errors can be induced by user selection of grid and delocalization parameters[144,152]. Local changes in the field evaporation properties can also affect the reported size of the imaged microstructural feature[395,396]. Although there are proposed protocols to correct the distance or the data reconstruction[397,] they are scarcely used and, ultimately, rely on another set of assumptions, and may therefore not represent a significant advance after all. Ultimately, the community must accept that APT is extremely valuable despite its intrinsic limitations and include these in the discussion of results, including precision and accuracy.

Outlook

The outlook for the future of APT is bright, and it may be possible to finally achieve true atomic-scale tomography[398] with the ability to measure the isotopic identity and spatial coordinates of every atom in a material of interest. This would require that every atom is unambiguously counted and identified, with accurate and precise spatial reconstruction of its original location in the specimen with true atomic resolution. Ideally, such a method would be applicable to any material that can be fashioned into a suitably shaped specimen, whether solid or liquid, soft or hard, organic or inorganic. Finally, all of this information should be collected in large, experimentally relevant volumes. APT would then be close to being a standard reference technique for measurement of chemical composition as, in the most fundamental sense, it is simply counting individual atoms. Uniquely, and unlike other standardized methods used to measure chemical composition, it can provide this information on highly local, arbitrarily shaped and oriented analysis volumes.

We are not there yet, but this lofty goal guides the technique's progress. Below, we discuss recent advances in some of these areas including standards, experimental hardware, data analysis, simulation, reconstruction, sample preparation and handling, and integration of complementary and correlative analytical techniques.

Hardware

Some of the most exciting recent developments in hardware have come in the form of either combining other instruments with the atom probe itself or integrating an atom probe into working versions of other analytical tools. These can aid in specimen preparation, provide additional data to inform reconstruction and analysis, give complementary measurements or provide correlative information for multimodal microscopy studies. For example, atom probe instruments have recently been successfully integrated with both SEM and FIBs[399–401]. A start-up at the University of Stuttgart (INSPICO High Resolution Analysis) is developing a modular instrument directly attached to a FIB enabling direct transfer from electron and ion imaging to APT analysis. Dedicated chambers are also in development or operation to perform chemical reactions at the specimen's surface and probe its response[402,403]. In a similar vein, an in situ micro-photoluminescence bench that can be operated during atom probe analysis has recently come online[404] with the ability to interpret optical data through analysis of the 3D chemical structure. Finally, there are ambitious projects underway to integrate an atom probe directly into the pole gap of a TEM system as a module[405,406] or via a dedicated holder following earlier designs[407].

Similarly, there has been great progress with integration of sensitive-atmosphere specimen preparation and handling capability with atom probe instruments[364,408]. These include cryogenic specimen preparation, handling and transfer[119,130,409,410] as well as in situ environmental treatment cells[402,411] for performing studies related to hydrogen embrittlement, phase transformations and catalysis.

There have been recent developments that make use of ionizing radiation to enable new pulsing paradigms. Ultra-fast femtosecond-pulsed extreme ultraviolet radiation[412,413] has been used to trigger alternative field ion emission schemes such as photoexcitation or photoionization[414], or to enable a more localized heating mechanism with the aim of eliminating some of the uncertainty associated with the current state-of-the-art near-ultraviolet laser pulsing. Finally, detectors that will not only detect every emitted ion but unambiguously identify its isotopic species have recently been experimentally demonstrated[415,416]. Some recent advances on atom probe detectors are discussed in BOX 6.

Revisiting FIM

FIM, the predecessor to APT, does not suffer from the spatial resolution limitations of APT as atoms are imaged prior to departing the sample surface. Indeed, aberrations occur in the early stages of the ionic flight. The magnification in FIM can still be affected by local variations in curvature, and the contrast in field ion imaging is not yet fully understood. To date, there have been several efforts to revive FIM[417] as one more way to complement APT[402]. First, 3D FIM was introduced[418,419], and multiple digital image processing routines developed to extract atomic positions and build atomically resolved tomograms[420–422]. New

imaging simulations have also been proposed[422], aiming in part to explain the nature of the observed contrast using density-functional theory to model the image gas ion current based on the local density of state of the surface atoms under an intense electric field[179]. To support these insights, FIM was performed within APT and filtering routines deployed on the time-of-flight mass spectrometry data to distinguish the mass to charge ratio of the field-evaporated surface atoms from the high background caused by the ionization of the imaging gas[179]. This first study of analytical FIM demonstrated a higher spatial resolution than APT and the ability to image segregation at structural defects with atomic resolution. Today, analytical FIM is in its infancy and will require hardware and software developments to make it an established technique[423].

Moving the state of the art

Much work remains to be done in the area of data analysis, simulation and reconstruction. Most fundamentally, a better and more thorough understanding of the field evaporation process is required. Great progress has been made in recent years[384,424] with regard to understanding the fundamental physics of evaporation and bond breaking on surfaces under a high field (BOX 7). Modelling and simulations have brought many insights and understanding of the origins and influence of aberrations on APT data[382,425–427], yet it is critical that more is done in the future to advance our understanding of field evaporation physics, which in part underpins aberrations.

In contrast to TEM, there are no current ways to correct trajectory aberrations by implementing or improving ion optical devices. The limit originates from the field evaporation process and the influence of the atomic neighbourhood on the evaporation field — both locally in a random solid solution and on a mesoscale for a particle in a matrix. To better understand trajectory aberrations, a full simulation of an atom probe specimen of arbitrary composition and relevant size under high applied field with appropriate timescales would require linking time-dependent density-functional theory with molecular dynamics, for example. This will surely become an active area of research as computational resources continue to improve in the future.

Intensive research continues to develop new reconstruction approaches to mitigate, and perhaps eventually eliminate, the effects of the assumptions and approximations that underpin the state-of-the-art algorithms[428]. For instance, given its inherent simplicity, the point-projection algorithm described above is surprisingly robust. However, its limitations are well documented and can be prohibitive for certain analyses. Some of the most promising of these algorithms use complementary simulations of how the applied electric field evolves with the shape of the specimen to predict the path of the ions to the detector and, ultimately, to guide their reverse projection back into the reconstructed image[429–432]. Correlative experimental protocols also enable the determination of the actual shape of the emitter using scanning probe microscopy[433] or electron tomography[434]. Combined with shape predictions of specimens, it may be possible to retrieve the necessary information from the APT experiment alone[380,435]. Approaches are also being pursued to derive a specimen’s shape from simulations[426,429]. These new methods demonstrate increasing capability and viability and are likely to play a significant role in the future of APT.

However, for now, the reverse-projection algorithm remains by far the most implemented model and imperfect data already provide much-needed information.

Finally, the data streams coming out of future APT experiments will be larger and integrate signals from simultaneous microscopies and spectroscopies, providing more information than human expertise alone can analyse. The field is poised to benefit from advances in artificial intelligence for automated analyses as well as to find features buried in noisy data. Forays have already been made across the data processing workflow by using machine learning approaches for identification of cluster or phases, patterns in detector maps and peaks in mass spectra[146,175,436–438]. An added benefit will be the improved reproducibility of data analyses, which currently suffers from the lack of established standards.

Liquids and soft matter

Liquids are a new frontier for APT application, as controlled field evaporation of water ice formed directly on field emitters had been reported[439–442] without solutions. Adineh et al.[443] have proposed an approach to encapsulate liquids on a metal tip using graphene, preventing sublimation. Qiu et al.[444] used this encapsulation approach to study a solution containing a gold nanoparticle. Their results suggest the robustness of this strategy.
The recent development of cryogenic FIB sample preparation and cryogenic ultra-high vacuum sample transfer offers additional potential for encapsulation in liquid solutions with controlled freezing rates. Several groups have analysed specimens from water layers on hydrated porous nanostructured materials kept frozen via a complete cold chain through to analysis[124–126,130], including challenging site-specific specimen preparation by lift-out at cryogenic temperature via redeposition to weld the lifted out wedge onto the support[130].

Cryogenic FIB sample preparation also helps characterize beam-sensitive, organic-containing materials[129], which leads to how APT can be applied to biological materials beyond what has been achieved so far[340,341,361,362,445,446]. Only careful fast cryogenic freezing can retain the original biological structure in a solid state. When cooled slowly, ice will crystallize and the associated volume expansion destroys the delicate structure of biological matter. However, when cooled fast enough, water can transform directly to a metastable vitreous ice phase that preserves the specimen’s original structure. Further work is required to develop workflows that allow the preparation of vitreous biological matter, such as tissue, cell components or solutions containing biological molecules.

Closing remarks

Going forwards, there must be confidence in APT’s ability to provide ground truth data and make absolute measurements of specimen shape with a high degree of certainty, and of chemical composition down to individual isotopes[437]. Improvements in the fundamental understanding of the field ion emission process are required for both of these aspects, and to determine oxidation states for the detected ions[320]. Modelling and simulation of the evaporation process needs to mature to where it can inform reconstruction so that experimental errors can be substantially reduced and, more importantly, accurately quantified. There must be developments in the areas of handling and analysis of heretofore ‘impossible’ materials, which include materials as simple as pure water ice. Forays into

novel areas must be accompanied by the development of standards to ensure the reliability and repeatability of data acquisition and interpretation beyond what is routinely done in the field. This is necessary to communicate with industries increasingly applying APT to solve technological problems, such as performing failure analysis of memory devices or batteries.

Acknowledgements

This Primer was a collaborative effort and, even though the authors tried to be inclusive of all perspectives on various aspects of atom probe tomography (APT) research, it reflects our experiences and some articles likely escaped our attention. Apologies to those forgotten — it was not intentional. B.G. is thankful to past and present members of the Atom Probe group at Max-Planck-Institut für Eisenforschung (MPIE) and financial support from the European Research Council (ERC) (ERC-CoG-SHINE-771602), the Max-Planck Society, the BMBF (Federal Ministry of Education and Research), the Deutsche Forschungsgemeinsschaft (DFG) including for the Leibniz Prize, the Volkswagen Stiftung, the Alexander von Humboldt Stiftung and the Engineering and Physical Sciences Research Council (EPSRC) (and some companies). J.M.C. is grateful to the Australian Research Council (ARC) for her Future Fellowship. O.C.-M. is grateful for funding from the BMWi EFFCIS II and DFG 917 Nanoswitches. T.L. thanks the DFG for financial support (project number 407513992). R.D. acknowledges NSERC (Natural Sciences and Engineering Research Council of Canada) for her doctoral postgraduate scholarship (PGS-D). P.S. is grateful for funding from the BMBF (VIP 03V0756). S.K.M. acknowledges financial support from AVH and funding from the DFG SFB-TR103 project A4. M.M. acknowledges financial support EPSRC grants EP/M022803/1 and EP/S021663/1.

Glossary

Solutes
Atoms of a species different from the main constituent atoms, which correspond to the solvent in a mixture. Solutes, often called dopants in electronic materials, are added to modify the material’s properties

Microstructural imperfections
Irregularities in the arrangement of atoms in a crystal, often modifying a material’s physical properties. These include lattice defects as well as inclusions of isolated or clustered foreign atoms, second phases or particles forming in a matrix of the main constituting element (solvent)

Vacancies
Atoms missing from one of the crystal lattice sites forming a point defect

Dislocations
Linear crystal defects typically associated with the plastic deformation of a material. There are two main types of dislocation, edge and screw. A single defect can exhibit both characteristics in different parts along the dislocation line. Mobile (glissile) and immobile (sessile) dislocations both exist. In the case of an edge dislocation, the addition of an extra half-plane of atoms in the structure results in a compressive stress on one side of the dislocation and a tensile stress on the other. Segregation of solute elements to the dislocation helps reduce the free energy associated with these defects

Stacking faults
Local changes in the stacking sequence of atomic layers in a crystal

Twins

Two crystals with a defined crystallographic relationship with each other, formed typically by a cooperative displacement of atoms along a specific plane referred to as a twin boundary, which can be caused by plastic deformation. The organization of atoms on either side of the twin boundary can be such that they are mirror images of each other, or follow a specific rational twin law. Twin boundaries are often considered low-energy

Grain boundaries
Junctions of two crystals (most crystalline materials are made of an ensemble of individual crystals, referred to as grains). The local discontinuity of the atomic arrangement makes grain boundaries loci of interest for microstructure design. Segregation of solutes typically happens to minimize the system's free energy, and grain boundaries assist with heterogeneous nucleation of secondary phases, for instance. The grain boundary energy depends on the magnitude of the change in orientation between the two grains as well as the crystallographic plane at the junction of the two grains

Secondary phases and phase boundaries
Solids formed by a mixture of species can adopt one or more thermodynamic phases, which can sometimes co-exist. The formation of such secondary phases can be hindered by the kinetics, often associated with lattice diffusion and thermal activation. The discontinuity in the crystal lattice introduced by the presence of this second phase forms a phase boundary. The difference in the lattice unit cell can make secondary phases only partially or completely incoherent with the host lattice. Often, there exists a relationship in the crystalline orientation between the matrix and the secondary phase particle

Composition
The relative quantity of atoms of a species with respect to all atoms of all the detected species given in atomic per cent

Polarity
Here, the electrical polarity, used to represent the electric positive (+) or negative (−) sign of the electrical potential at the ends of an electrical circuit

Field ionization
A physical phenomenon whereby atoms or molecules can be ionized because of an intense electric field

Field evaporation
A physical phenomenon whereby atoms constituting a material can be removed in the form of ions because of an intense electric field

Projection optic
In microscopy, the transfer of the image of an object onto a surface through an optical system that can contain lenses or mirrors, for instance

Time-of-flight mass spectrometer
A spectrometer that exploits the proportionality of an ion's mass to charge ratio with its time of flight from a source to a particle detector to deduce the nature of atomic or molecular ions

Reflectron
An electrostatic mirror that can be flat or concave helping to correct spread in the time of flight associated with energy deficits by allowing adjustment of the ions' flight distance proportionally to their incoming energy

Delay-line detector
A type of particle detector where the particle impact location on the detector's surface is deduced from the difference in the arrival time of electrical signals at the two ends of a line, that is, a wire. Delay-line detectors typically contain two or three lines to obtain the lateral and vertical coordinates of the impact position, with the signals forming the third line used to disambiguate combinations of signals coming from multiple impacts

Molecular ions
Ions containing more than one atom (as opposed to atomic ions) that have, overall, lost one or more electrons. Molecular ions are usually metastable, but some are sufficiently long-lived to be detected

Micro-tip coupon
A support for lift-out specimen preparation, typically made of silicon processed by a reactive ion and/or chemical etching.

Local electrode
A conical microelectrode implemented on the commercial local electrode atom probe (LEAP), positioned approximately 40 μm away from the specimen, enabling a strong localized increase in the electric field at the apex of the specimen. The implementation of such microelectrodes enabled mounting multiple specimens at once into the instrument and, then, analysis in succession

Mass peak ranging
The definition of the lower and higher mass to charge values of each individual mass peak in the mass spectrum to associate the mass to charge with one element or a combination of atoms from one or multiple elements

Image compression
An atom probe-specific term describing the angular compression associated with the ion projection; that is, the ratio of the crystallographic angle to the imaged angle

Quasi-stereographic projection
A model of point projection of a sphere onto a plane, which is bijective and preserves angles but neither distances nor areas. The standard projection has the projection point and the projection plane diametrically opposed. In a quasi-stereographic projection, this is not necessarily the case.

Voxelization
In an atom probe, the conversion of the three-dimensional point cloud into an array or grid of volumetric elements containing a certain number of atoms of a certain size. Following

voxelization, the number of atoms of each defined species can be used to calculate a local composition, and is usually subject to a smoothing process termed delocalization

Iso-surface
A three-dimensional surface representing points of a given threshold value of composition, concentration or density within the 3D point cloud. The iso-surface is built from the grid of voxels and, hence, subject to the delocalization

Iso-concentration
The concentration is a quantity per unit volume expressed in atoms per cubic nanometre, for instance, equivalent to a density. Owing to trajectory aberrations and reconstruction issues, volume estimations from reconstructed atom probe data are typically not precise

Interfacial excess
The number of excess atoms of a certain species per unit area of an interface

Round robin experiment
A set of interlaboratory measurements independently performed that allows for direct comparison of analyses and results, and that can help guide establishing best practice

Rayleigh criterion
The shortest distance below which the diffraction-limited image of two point sources can no longer be separated

References

1. De Geuser F & Gault B Metrology of small particles and solute clusters by atom probe tomography. Acta Mater. 188, 406–415 (2020).
2. Müller EW, Panitz JA, McLane SB & Müller EW Atom-probe field ion microscope. Rev. Sci. Instrum. 39, 83–86 (1968).
3. Muller EW Oberflachenwanderung von Wolfram auf dem eigenen Kristallgitter [German]. Z. Fur Phys. 126, 642–665 (1949).
4. Müller EW & Bahadur K Field ionization of gases at a metal surface and the resolution of the field ion microscope. Phys. Rev. 102, 624–631 (1956).
5. Müller EW Experiments of the theory of electron emission under the influence of high field strength. Phys. Z. 37, 838–842 (1936).
6. Durand E Electrostatique Et Magnétostatique [French] (Masson & Cie, Libraires De L'académie De Médecine, 1953).
7. Smith R & Walls JM Ion trajectories in field-ion microscope. J. Phys. D-Applied Phys. 11, 409–419 (1978).
8. Müller EW Atoms visualized. Sci. Am. 196, 113–122 (1957).
9. Müller EW Atom-probe field ion microscope. Naturwissenschaften 57, 222–230 (1970).
10. Panitz JA The 10 cm atom probe. Rev. Sci. Instrum. 44, 1034 (1973).
11. Waugh AR, Boyes ED & Southon MJ Field-desorption microscopy and the atom probe. Nature 253, 342–343 (1975).
12. Cerezo A, Godfrey TJ & Smith GDW Application of a position-sensitive detector to atom probe microanalysis. Rev. Sci. Instrum. 59, 862 (1988).
13. Blavette D, Bostel A, Sarrau JM, Deconihout B & Menand A An atom probe for three-dimensional tomography. Nature 363, 432–435 (1993).

14. Kelly TF & Miller MK Invited review article: Atom probe tomography. Rev. Sci. Instrum. 78, 31101 (2007). This article is a thorough introductory review article on APT, with an emphasis on its historical developments.
15. Miller MK The development of atom probe field-ion microscopy. Mater. Charact. 44, 11–27 (2000).
16. Cadel E, Fraczkiewicz A & Blavette D Atomic scale observation of Cottrell atmospheres in B-doped FeAl (B2) by 3D atom probe field ion microscopy. Mater. Sci. Engin. A 309, 32–37 (2001).
17. Wilde J, Cerezo A & Smith GDW Three-dimensional atomic-scale mapping of a Cottrell atmosphere around a dislocation in iron. Scr. Mater. 43, 39–48 (2000).
18. Herbig M et al. Atomic-scale quantification of grain boundary segregation in nanocrystalline material. Phys. Rev. Lett. 112, 126103 (2014). [PubMed: 24724663]
19. Liebscher CH et al. Strain-induced asymmetric line segregation at faceted Si grain boundaries. Phys. Rev. Lett. 121, 15702 (2018).
20. Gault B et al. Interfaces and defect composition at the near-atomic scale through atom probe tomography investigations. J. Mater. Res. 33, 4018–4030 (2018).
21. Ringer SP & Apperley MH Networking strategies of the microscopy community for improved utilisation of advanced instruments: (1) The Australian Microscopy and Microanalysis Research Facility (AMMRF). Comptes Rendus Phys. 15, 269–275 (2014).
22. Larson DJ Local Electrode Atom Probe Tomography: A User's Guide (Springer, 2013).
23. Lefebvre-Ulrikson W, Vurpillot F & Sauvage X Atom Probe Tomography: Put Theory into Practice (Academic, 2016).
24. Kelly TF et al. First data from a commercial local electrode atom probe (LEAP). Microsc. Microanal. 10, 373–383 (2004). [PubMed: 15233856]
25. Nishikawa O, Ohtani Y, Maeda K, Watanabe M & Tanaka K Development of the scanning atom probe and atomic level analysis. Mater. Charact. 44, 29–57 (2000).
26. Grennan-Heaven N, Cerezo A, Godfrey TJJ & Smith GDW Design of a scanning atom probe with improved mass resolution using post deceleration. Ultramicroscopy 107, 59–60 (2006).
27. Kelly TF, Camus PP, Larson DJ, Holzman LM & Bajikar SS On the many advantages of local-electrode atom probes. Ultramicroscopy 62, 29–42 (1996). [PubMed: 22666915]
28. Ravelo B & Vurpillot F Analysis of excitation pulsed signal propagation for atom probe tomography system. Prog. Electromagn. Res. Lett. 47, 61–70 (2014).
29. Kellogg GL & Tsong TT Pulsed-laser atom-probe field-ion microscopy. J. Appl. Phys. 51, 1184 (1980).
30. Cerezo A, Grovenor CRM & Smith GDW Pulsed laser atom probe analysis of semiconductor materials. J. Microscopy 141, 155–170 (1986).
31. Gault B et al. Design of a femtosecond laser assisted tomographic atom probe. Rev. Sci. Instrum. 77, 43705 (2006).
32. Bunton JH, Olson JD, Lenz DR & Kelly TF Advances in pulsed-laser atom probe: instrument and specimen design for optimum performance. Microsc. Microanal. 13, 418–427 (2007). [PubMed: 18001508]
33. Schlesiger R et al. Design of a laser-assisted tomographic atom probe at Munster University. Rev. Sci. Instrum. 81, 43703 (2010).
34. Houard J, Vella A, Vurpillot F & Deconihout B Conditions to cancel the laser polarization dependence of a subwavelength tip. Appl. Phys. Lett. 94, 121905 (2009).
35. Koelling S et al. In-situ observation of non-hemispherical tip shape formation during laser-assisted atom probe tomography. J. Appl. Phys. 109, 104909 (2011).
36. Poschenrieder WP Multiple-focusing time of flight mass spectrometers. Part I. TOFMS with equal momentum acceleration. Int. J. Mass. Spectrom. Ion. Phys. 6, 413–426 (1971).
37. Bostel A & Yavor M Patent Application Publication Pub. No.: US 2010/0223698 A1 (2010).
38. Mamyrin BA, Karataev VI, Shmikk DV & Zagulin VA Mass-reflectron a new nonmagnetic time-of-flight high-resolution mass-spectrometer. Zhurnal Eksp. I Teor. Fiz. 64, 82–89 (1973).

39. Bemont E et al. Effects of incidence angles of ions on the mass resolution of an energy compensated 3D atom probe. Ultramicroscopy 95, 231–238 (2003). [PubMed: 12535569]
40. Panayi P A reflectron for use in a three-dimensional atom probe. Great Britain Patent No. GB2426120A (2006).
41. Clifton P, Gribb T, Gerstl S, Ulfig RM & Larson DJ Performances advantages of a modern, ultra-high mass resolution atom probe. Microsc. Microanal. 14, 454–455 (2008).
42. Deconihout B, Gerard P, Bouet M & Bostel A Improvement of the detection efficiency of channel plate electron multiplier for atom probe application. Appl. Surf. Sci. 94–5, 422–427 (1996).
43. Jagutzki O et al. Multiple hit readout of a microchannel plate detector with a three-layer delay-line anode. IEEE Trans. Nucl. Sci. 49, 2477–2483 (2002).
44. Da Costa G, Vurpillot F, Bostel A, Bouet M & Deconihout B Design of a delay-line position-sensitive detector with improved performance. Rev. Sci. Instrum. 76, 13304 (2005).
45. Brandon DG On field evaporation. Philos. Mag. 14, 803–820 (1966).
46. Waugh AR, Boyes ED & Southon MJ Investigations of field evaporation with field desorption microscope. Surf. Sci. 61, 109–142 (1976).
47. Wada M On the thermally activated field evaporation of surface atoms. Surf. Sci. 145, 451–465 (1984).
48. Menand A & Kingham DR Evidence for the quantum mechanical tunnelling of boron ions. J. Phys. C Solid. State Phys. 18, 4539–4547 (1985).
49. Kingham DR The post-ionization of field evaporated ions: a theoretical explanation of multiple charge states. Surf. Sci. 116, 273–301 (1982).
50. Kellogg GL Determining the field emitter temperature during laser irradiation in the pulsed laser atom probe. J. Appl. Phys. 52, 5320 (1981).
51. Kellogg GL Measurement of the charge state distribution of field evaporated ions: evidence for post-ionization. Surf. Sci. 120, 319–333 (1982).
52. Marquis EA & Gault B Determination of the tip temperature in laser assisted atom-probe tomography using charge state distributions. J. Appl. Phys. 104, 84914 (2008).
53. Shariq A et al. Investigations of field-evaporated end forms in voltage- and laser-pulsed atom probe tomography. Ultramicroscopy 109, 472–479 (2009). [PubMed: 19062187]
54. Katnagallu S et al. Impact of local electrostatic field rearrangement on field ionization. J. Phys. D Appl. Phys. 51, 105601 (2018).
55. Zhu M et al. Unique bond breaking in crystalline phase change materials and the quest for metavalent bonding. Adv. Mater. 30, 1706735 (2018).
56. Yu Y, Cagnoni M, Cojocaru-Mirédin O & Wuttig M Chalcogenide thermoelectrics empowered by an unconventional bonding mechanism. Adv. Funct. Mater. 30, 1904862 (2020).
57. Yao L, Gault B, Cairney JM & Ringer SP On the multiplicity of field evaporation events in atom probe: a new dimension to the analysis of mass spectra. Philos. Mag. Lett. 90, 121–129 (2010).
58. Saxey DW Correlated ion analysis and the interpretation of atom probe mass spectra. Ultramicroscopy 111, 473–479 (2011). [PubMed: 21159435]
59. Peng Z et al. Unraveling the metastability of Cn2+ (n = 2–4) clusters. J. Phys. Chem. Lett. 10, 581–588 (2019). [PubMed: 30673242]
60. Sha W et al. Some aspects of atom-probe analysis of Fe–C and Fe–N systems. Surf. Sci. 266, 416–423 (1992).
61. Silaeva EP et al. Do dielectric nanostructures turn metallic in high-electric DC fields? Nano Lett. 14, 6066–6072 (2014). [PubMed: 25271987]
62. Karahka M & Kreuzer HJ Field evaporation of oxides: a theoretical study. Ultramicroscopy 132, 54–59 (2013). [PubMed: 23318144]
63. Kellogg G Field evaporation of silicon and field desorption of hydrogen from silicon surfaces. Phys. Rev. B 28, 1957–1964 (1983).
64. Müller M, Saxey DW, Smith GDW & Gault B Some aspects of the field evaporation behaviour of GaSb. Ultramicroscopy 111, 487–492 (2011). [PubMed: 21159438]
65. Zanuttini D et al. Simulation of field-induced molecular dissociation in atom-probe tomography: identification of a neutral emission channel. Phys. Rev. A 95, 61401 (2017).

66. Miller MK An atom probe study of the anomalous field evaporation of alloys containing silicon. J. Vac. Sci. Technol. 19, 57 (1981).
67. Yao L, Cairney JM, Zhu C & Ringer SP Optimisation of specimen temperature and pulse fraction in atom probe microscopy experiments on a microalloyed steel. Ultramicroscopy 111, 648–651 (2011). [PubMed: 21247701]
68. Mancini L et al. Composition of wide bandgap semiconductor materials and nanostructures measured by atom probe tomography and its dependence on the surface electric field. J. Phys. Chem. C. 118, 24136–24151 (2014).
69. Kolli RP & Seidman DN Comparison of compositional and morphological atom-probe tomography analyses for a multicomponent Fe–Cu steel. Microsc. Microanal. 13, 272–284 (2007). [PubMed: 17637076]
70. Tang F, Gault B, Ringer SP & Cairney JM Optimization of pulsed laser atom probe (PLAP) for the analysis of nanocomposite Ti–Si–N films. Ultramicroscopy 110, 836–843 (2010). [PubMed: 20417033]
71. Huang M, Cerezo A, Clifton PH & Smith GDW Measurements of field enhancement introduced by a local electrode. Ultramicroscopy 89, 163–167 (2001). [PubMed: 11770742]
72. Loi ST, Gault B, Ringer SP, Larson DJ & Geiser BP Electrostatic simulations of a local electrode atom probe: the dependence of tomographic reconstruction parameters on specimen and microscope geometry. Ultramicroscopy 132, 107–113 (2013). [PubMed: 23294557]
73. Miller MK & Smith GDW Atom Probe Microanalysis: Principles and Applications to Materials Problems (Materials Research Society, 1989).
74. Melmed AJ The art and science and other aspects of making sharp tips. J. Vac. Sci. Technol. B 9, 601–608 (1991).
75. Papazian JM The preparation of field-ion-microscope specimens containing grain boundaries. J. Microsc. 94, 63–67 (1971).
76. Nordén H & Bowkett KM Electron microscope holders for viewing thin wire specimens and field-ion microscope tips. J. Sci. Instrum. 44, 238–240 (1967).
77. Waugh AR, Payne S, Worrall GM & Smith GDW In-situ ion milling of field-ion specimens using a liquid-metal ion-source. J. Phys. 45, 207–209 (1984).
78. Thompson K et al. In situ site-specific specimen preparation for atom probe tomography. Ultramicroscopy 107, 131–139 (2007). [PubMed: 16938398]
79. Thompson K, Larson DJ & Ulfig RM Pre-sharpened and flat-top microtip coupons: a quantitative comparison for atom-probe analysis studies. Microsc. Microanal. 11, 882–883 (2005).
80. Estivill R, Audoit G, Barnes J-P, Grenier A & Blavette D Preparation and analysis of atom probe tips by xenon focused ion beam milling. Microsc. Microanal. 22, 576–582 (2016). [PubMed: 27056544]
81. Eder K, Bhatia V, Van Leer B & Cairney JM Using a plasma fib equipped with Xe, N_2, O_2 and Ar for atom probe sample preparation—ion implantation and success rates. Microsc. Microanal. 25, 316–317 (2019).
82. Halpin JE et al. An in-situ approach for preparing atom probe tomography specimens by xenon plasma-focussed ion beam. Ultramicroscopy 202, 121–127 (2019). [PubMed: 31005819]
83. Miller MK, Russell KF & Thompson GB Strategies for fabricating atom probe specimens with a dual beam FIB. Ultramicroscopy 102, 287–298 (2005). [PubMed: 15694675]
84. Prosa TJ & Larson DJ Modern focused-ion-beam-based site-specific specimen preparation for atom probe tomography. Microsc. Microanal. 23, 194–209 (2017). [PubMed: 28162119] This article reviews methods for specimen preparation primarily using the FIB.
85. Makineni SK et al. Correlative microscopy — novel methods and their applications to explore 3D chemistry and structure of nanoscale lattice defects: a case study in superalloys. JOM 70, 1736–1743 (2018).
86. Herbig M Spatially correlated electron microscopy and atom probe tomography: current possibilities and future perspectives. Scr. Mater. 148, 98–105 (2018).
87. Felfer PJ, Alam T, Ringer SP & Cairney JM A reproducible method for damage-free site-specific preparation of atom probe tips from interfaces. Microsc. Res. Tech. 75, 484–491 (2012). [PubMed: 21956865]

88. Herbig M, Choi P & Raabe D Combining structural and chemical information at the nanometer scale by correlative transmission electron microscopy and atom probe tomography. Ultramicroscopy 153, 32–39 (2015). [PubMed: 25723104]
89. Felfer P et al. New approaches to nanoparticle sample fabrication for atom probe tomography. Ultramicroscopy 159, 413–419 (2015). [PubMed: 25980894]
90. Lovall D, Buss M, Andres R & Reifenberger R Resolving the atomic structure of supported nanometer-size Au clusters. Phys. Rev. B Condens. Matter Mater. Phys. 58, 15889–15896 (1998).
91. Li T et al. Atomic imaging of carbon-supported Pt, Pt/Co, and Ir@Pt nanocatalysts by atom-probe tomography. ACS Catal. 4, 695–702 (2014).
92. Tedsree K et al. Hydrogen production from formic acid decomposition at room temperature using a Ag–Pd core-shell nanocatalyst. Nat. Nanotechnol. 6, 302–307 (2011). [PubMed: 21478867]
93. Yu KMK et al. Non-syngas direct steam reforming of methanol to hydrogen and carbon dioxide at low temperature. Nat. Commun. 3, 1230 (2012). [PubMed: 23187630]
94. Eley C et al. Nanojunction-mediated photocatalytic enhancement in heterostructured CdS/ZnO, CdSe/ZnO, and CdTe/ZnO nanocrystals. Angew. Chem. Int. Ed. 126, 7972–7976 (2014).
95. Raghuwanshi M, Cojocaru-Mirédin O & Wuttig M Investigating bond rupture in resonantly bonded solids by field evaporation of carbon nanotubes. Nano Lett. 20, 116–121 (2020). [PubMed: 31804085]
96. Ene CB, Schmitz G, Kirchheim R & Hütten A Stability and thermal reaction of GMR NiFe/Cu thin films. Acta Mater. 53, 3383–3393 (2005).
97. Stender P, Balogh Z & Schmitz G Triple line diffusion in nanocrystalline Fe/Cr and its impact on thermal stability. Ultramicroscopy 111, 524–529 (2011). [PubMed: 21146307]
98. Prosa T, Kostrna Keeney S & Kelly TF Local electrode atom probe analysis of poly(3-alkylthiophene)s. J. Microsc. 237, 155–167 (2010). [PubMed: 20096046]
99. Gault B et al. Atom probe microscopy of self-assembled monolayers: preliminary results. Langmuir 26, 5291–5294 (2010). [PubMed: 20297779]
100. Stoffers A, Oberdorfer C & Schmitz G Controlled field evaporation of fluorinated self-assembled monolayers. Langmuir 28, 56–59 (2012). [PubMed: 22136132]
101. Devaraj A et al. Visualizing nanoscale 3D compositional fluctuation of lithium in advanced lithium-ion battery cathodes. Nat. Commun. 6, 8014 (2015). [PubMed: 26272722]
102. Diercks D, Gorman BP, Cheung CL & Wang G Techniques for consecutive TEM and atom probe tomography analysis of nanowires. Microsc. Microanal. 15, 254–255 (2009).
103. Xiang Y et al. Long-chain terminal alcohols through catalytic CO hydrogenation. J. Am. Chem. Soc. 135, 7114–7117 (2013). [PubMed: 23634891]
104. Perea DE, Wijaya E, Lensch-Falk JL, Hemesath ER & Lauhon LJ Tomographic analysis of dilute impurities in semiconductor nanostructures. J. Solid. State Chem. 181, 1642–1649 (2008).
105. Du S et al. Full tip imaging in atom probe tomography. Ultramicroscopy 124, 96–101 (2013). [PubMed: 23142750]
106. Yang Q et al. Atom probe tomography of Au–Cu bimetallic nanoparticles synthesized by inert gas condensation. J. Phys. Chem. C. 123, 26481–26489 (2019).
107. Yang Q et al. A combined approach for deposition and characterization of atomically engineered catalyst nanoparticles. Catal. Struct. React. 1, 125–131 (2015).
108. Barroo C, Akey AJ & Bell DC Aggregated nanoparticles: sample preparation and analysis by atom probe tomography. Ultramicroscopy 218, 113082 (2020). [PubMed: 32731130]
109. Felfer P, Benndorf P, Masters A, Maschmeyer T & Cairney JM Revealing the distribution of the atoms within individual bimetallic catalyst nanoparticles. Angew. Chem. Int. Ed. 53, 11190–11193 (2014).
110. Raine E et al. Synthesis and characterization of platinum nanoparticle catalysts capped with isolated zinc species in SBA-15 cChannels: the wall effect. ACS Appl. Nano Mater. 1, 6603–6612 (2018).
111. Yu B et al. Enhanced propylene oxide selectivity for gas phase direct propylene epoxidation by lattice expansion of silver atoms on nickel nanoparticles. Appl. Catal. B Env. 243, 304–312 (2019).

112. Jiang K et al. Highly selective oxygen reduction to hydrogen peroxide on transition metal single atom coordination. Nat. Commun. 10, 3997 (2019). [PubMed: 31488826]
113. Wang Z et al. Acidity enhancement through synergy of penta- and tetra-coordinated aluminum species in amorphous silica networks. Nat. Commun. 11, 225 (2020). [PubMed: 31932684]
114. Wilde P et al. Insights into the formation, chemical stability, and activity of transient NiyP@NiO_x core-shell heterostructures for the oxygen evolution reaction. ACS Appl. Energy Mater. 3, 2304–2309 (2020).
115. Larson DJ et al. Encapsulation method for atom probe tomography analysis of nanoparticles. Ultramicroscopy 159, 420–426 (2015). [PubMed: 25748692]
116. Kim S-H et al. A new method for mapping the three-dimensional atomic distribution within nanoparticles by atom probe tomography (APT). Ultramicroscopy 190, 30–38 (2018). [PubMed: 29680520]
117. Kim S-H et al. Direct imaging of dopant and impurity distributions in 2D MoS_2. Adv. Mater. 32, 1907235 (2020).
118. Lim J et al. Atomic-scale mapping of impurities in partially reduced hollow TiO_2 nanowires. Angew. Chem. Int. Ed. 59, 5651–5655 (2020).
119. Perea DE, Gerstl SSA, Chin J, Hirschi B & Evans JE An environmental transfer hub for multimodal atom probe tomography. Adv. Struct. Chem. Imaging 3, 12 (2017). [PubMed: 28529842]
120. Chen Y-S et al. Direct observation of individual hydrogen atoms at trapping sites in a ferritic steel. Science 355, 1196–1199 (2017). [PubMed: 28302855]
121. Stephenson LT et al. The Laplace project: an integrated suite for correlative atom probe tomography and electron microscopy under cryogenic and UHV conditions. PLoS ONE 13, e0209211 (2018). [PubMed: 30576351]
122. Chen Y-S et al. Observation of hydrogen trapping at dislocations, grain boundaries, and precipitates. Science 367, 171–175 (2020). [PubMed: 31919217]
123. Breen AJ et al. Solute hydrogen and deuterium observed at the near atomic scale in high-strength steel. Acta Mater. 188, 108–120 (2020).
124. Schwarz TM et al. Field evaporation and atom probe tomography of pure water tips. Sci. Rep. 10, 20271 (2020). [PubMed: 33219263] This article is a first thorough report on the analysis of thick layers of ice, liquid-metal interfaces and solutions.
125. El-Zoka AA et al. Enabling near-atomic-scale analysis of frozen water. Sci. Adv. 6, eabd6324 (2020). [PubMed: 33277259]
126. Perea DE et al. Tomographic mapping of the nanoscale water-filled pore structure in corroded borosilicate glass. npj Mater. Degrad. 4, 1–7 (2020).
127. Chang Y et al. Ti and its alloys as examples of cryogenic focused ion beam milling of environmentally-sensitive materials. Nat. Commun. 10, 942 (2019). [PubMed: 30808943]
128. Lilensten L & Gault B New approach for FIB-preparation of atom probe specimens for aluminum alloys. PLoS ONE 15, e0231179 (2020). [PubMed: 32240256]
129. Rivas NA et al. Cryo-focused ion beam preparation of perovskite based solar cells for atom probe tomography. PLoS ONE 15, e0227920 (2020). [PubMed: 31945119]
130. Schreiber DK, Perea DE, Ryan JV, Evans JE & Vienna JD A method for site-specific and cryogenic specimen fabrication of liquid/solid interfaces for atom probe tomography. Ultramicroscopy 194, 89–99 (2018). [PubMed: 30092393]
131. Sebastian JT, Hellman OC & Seidman DN New method for the calibration of three-dimensional atom-probe mass spectra. Rev. Sci. Instrum. 72, 2984–2988 (2001).
132. Hudson D, Smith GDW & Gault B Optimisation of mass ranging for atom probe microanalysis and application to the corrosion processes in Zr alloys. Ultramicroscopy 111, 480–486 (2011). [PubMed: 21163577]
133. Valley JW et al. Hadean age for a post-magma-ocean zircon confirmed by atom-probe tomography. Nat. Geosci. 7, 219–223 (2014).
134. Lloyd MJ et al. Decoration of voids with rhenium and osmium transmutation products in neutron irradiated single crystal tungsten. Scr. Mater. 173, 96–100 (2019).

135. Edmondson PD, Gault B & Gilbert MR An atom probe tomography and inventory calculation examination of second phase precipitates in neutron irradiated single crystal tungsten. Nucl. Fusion. 60, 126013 (2020).
136. London AJ, Haley D & Moody MP Single-Ion deconvolution of mass peak overlaps for atom probe microscopy. Microsc. Microanal. 23, 300–306 (2017). [PubMed: 28300014]
137. Wilkes TJ, Smith GDW & Smith DA On the quantitative analysis of field ion micrographs. Metallography 7, 403–430 (1974).
138. Cerezo A, Warren PJ & Smith GDW Some aspects of image projection in the field-ion microscope. Ultramicroscopy 79, 251–257 (1999).
139. De Geuser F & Gault B Reflections on the projection of ions in atom probe tomography. Microsc. Microanal. 23, 238–246 (2017). [PubMed: 28148309]
140. Blavette D, Sarrau JM, Bostel A & Gallot J Direction and depth of atom probe analysis. Rev. Phys. Appl. 17, 435–440 (1982).
141. Bas P, Bostel A, Deconihout B & Blavette D A general protocol for the reconstruction of 3D atom probe data. Appl. Surf. Sci. 87–88, 298–304 (1995).
142. Gault B et al. Advances in the reconstruction of atom probe tomography data. Ultramicroscopy 111, 448–457 (2011). [PubMed: 21146931]
143. Jeske T & Schmitz G Nanoscale analysis of the early interreaction stages in Al/Ni. Scr. Mater. 45, 555–560 (2001).
144. Hellman OC, du Rivage JB & Seidman DN Efficient sampling for three-dimensional atom probe microscopy data. Ultramicroscopy 95, 199–205 (2003). [PubMed: 12535565]
145. Oberdorfer C, Eich SM & Schmitz G A full-scale simulation approach for atom probe tomography. Ultramicroscopy 128, 55–67 (2013). [PubMed: 23500891]
146. Wei Y et al. 3D nanostructural characterisation of grain boundaries in atom probe data utilizing machine learning methods. PLoS ONE 14, e022504 (2019).
147. Camus E & Abromeit C Analysis of conventional and 3-dimensional atom-probe data for multiphase materials. J. Appl. Phys. 75, 2373–2382 (1994).
148. Moody MP, Stephenson LT, Liddicoat PV & Ringer SP Contingency table techniques for three dimensional atom probe tomography. Microsc. Res. Tech. 70, 258–268 (2007). [PubMed: 17279508]
149. Moody MP, Stephenson LT, Ceguerra AV & Ringer SP Quantitative binomial distribution analyses of nanoscale like-solute atom clustering and segregation in atom probe tomography data. Microsc. Res. Tech. 71, 542–550 (2008). [PubMed: 18425800]
150. Hellman OC, Vandenbroucke JA, Rüsing J, Isheim D & Seidman DN Analysis of three-dimensional atom-probe data by the proximity histogram. Microsc. Microanal. 6, 437–444 (2000). [PubMed: 11003678]
151. Felfer P & Cairney J Advanced concentration analysis of atom probe tomography data: local proximity histograms and pseudo-2D concentration maps. Ultramicroscopy 189, 61–64 (2018). [PubMed: 29626834]
152. Martin TL et al. Insights into microstructural interfaces in aerospace alloys characterised by atom probe tomography. Mater. Sci. Technol. 32, 232–241 (2016).
153. Hellman OC & Seidman DN Measurement of the Gibbsian interfacial excess of solute at an interface of arbitrary geometry using three-dimensional atom probe microscopy. Mater. Sci. Eng. 327, 24–28 (2002).
154. Jenkins BM et al. Reflections on the analysis of interfaces and grain boundaries by atom probe tomography. Microsc. Microanal. 26, 247–257 (2020). [PubMed: 32186276]
155. Felfer P, Scherrer B, Demeulemeester J, Vandervorst W & Cairney JM Mapping interfacial excess in atom probe data. Ultramicroscopy 159, 438–444 (2015). [PubMed: 26346774]
156. Peng Z et al. An automated computational approach for complete in-plane compositional interface analysis by atom probe tomography. Microsc. Microanal. 25, 389–400 (2019). [PubMed: 30722805]
157. Yao L, Ringer SP, Cairney JM & Miller MK The anatomy of grain boundaries: their structure and atomic-level solute distribution. Scr. Mater. 69, 622–625 (2013).

158. Araullo-Peters VJ et al. Atom probe crystallography: atomic-scale 3-D orientation mapping. Scr. Mater. 66, 907–910 (2012).
159. Stephenson LT, Moody MP, Liddicoat PV & Ringer SP New techniques for the analysis of fine-scaled clustering phenomena within atom probe tomography (APT) data. Microsc. Microanal. 13, 448–463 (2007). [PubMed: 18001511]
160. Philippe T et al. Clustering and nearest neighbour distances in atom-probe tomography. Ultramicroscopy 109, 1304–1309 (2009). [PubMed: 19592168]
161. Dumitraschkewitz P, Gerstl SSA, Stephenson LT, Uggowitzer PJ & Pogatscher S Clustering in age-hardenable aluminum alloys. Adv. Eng. Mater. 20, 1800255 (2018). This article reviews and compares cluster-finding techniques, therein applied to aluminium alloys.
162. De Geuser F & Lefebvre W Determination of matrix composition based on solute-solute nearest-neighbor distances in atom probe tomography. Microsc. Res. Tech. 74, 257–263 (2011). [PubMed: 20623755]
163. Morsdorf L, Emelina E, Gault B, Herbig M & Tasan CC Carbon redistribution in quenched and tempered lath martensite. Acta Mater. 205, 116521 (2020).
164. Sudbrack C, Noebe R & Seidman D Direct observations of nucleation in a nondilute multicomponent alloy. Phys. Rev. B 73, 212101 (2006).
165. Haley D, Petersen T, Barton G & Ringer SP Influence of field evaporation on radial distribution functions in atom probe tomography. Philos. Mag. 89, 925–943 (2009).
166. De Geuser F, Lefebvre W & Blavette D 3D atom probe study of solute atoms clustering during natural ageing and pre-ageing of an Al–Mg–Si alloy. Philos. Mag. Lett. 86, 227–234 (2006).
167. Hyde JM & English CA An analysis of the structure of irradiation induced Cu-enriched clusters in low and high nickel welds. Mater. Res. Soc. Symp. Proc. 650, R6.6 (2001).
168. Miller MK & Kenik EA Atom probe tomography: a technique for nanoscale characterization. Microsc. Microanal. 8, 1126–1127 (2002).
169. Vaumousse D, Cerezo A & Warren PJ A procedure for quantification of precipitate microstructures from three-dimensional atom probe data. Ultramicroscopy 95, 215–221 (2003). [PubMed: 12535567]
170. Marceau RKW, Stephenson LT, Hutchinson CR & Ringer SP Quantitative atom probe analysis of nanostructure containing clusters and precipitates with multiple length scales. Ultramicroscopy 111, 738–742 (2011). [PubMed: 21215521]
171. Karnesky RA, Sudbrack CK & Seidman DN Best-fit ellipsoids of atom-probe tomographic data to study coalescence of γ' (L12) precipitates in Ni–Al–Cr. Scr. Mater. 57, 353–356 (2007).
172. Marquis EA & Hyde JM Applications of atom-probe tomography to the characterisation of solute behaviours. Mater. Sci. Eng. R. Rep. 69, 37–62 (2010).
173. Lefebvre W et al. 3DAP measurements of Al content in different types of precipitates in aluminium alloys. Surf. Interface Anal. 39, 206–212 (2007).
174. Ghamarian I & Marquis EA Hierarchical density-based cluster analysis framework for atom probe tomography data. Ultramicroscopy 200, 28–38 (2019). [PubMed: 30822614]
175. Zelenty J, Dahl A, Hyde J, Smith GDW & Moody MP Detecting clusters in atom probe data with Gaussian mixture models. Microsc. Microanal. 23, 269–278 (2017). [PubMed: 28441977]
176. Felfer P, Ceguerra AV, Ringer SP & Cairney JM Detecting and extracting clusters in atom probe data: a simple, automated method using Voronoi cells. Ultramicroscopy 150, 30–36 (2015). [PubMed: 25497494]
177. Vincent GB, Proudian AP & Zimmerman JD Three dimensional cluster analysis for atom probe tomography using Ripley's K-function and machine learning. Ultramicroscopy 220, 113151 (2021). [PubMed: 33152650]
178. Marquis EA et al. A round robin experiment: analysis of solute clustering from atom probe tomography data. Microsc. Microanal. 22, 666–667 (2016). [PubMed: 27329314]
179. Katnagallu S et al. Imaging individual solute atoms at crystalline imperfections in metals. N. J. Phys. 21, 123020 (2019).

180. Hyde JM, Marquis EA, Wilford KB & Williams TJ A sensitivity analysis of the maximum separation method for the characterisation of solute clusters. Ultramicroscopy 111, 440–447 (2011). [PubMed: 21227588]
181. Williams CA et al. Defining clusters in APT reconstructions of ODS steels. Ultramicroscopy 132, 271–278 (2013). [PubMed: 23333081]
182. Cerezo A & Davin L Aspects of the observation of clusters in the 3-dimensional atom probe. Surf. Interface Anal. 39, 184–188 (2007).
183. Zhao H, Gault B, Ponge D, Raabe D & De Geuser F Parameter free quantitative analysis of atom probe data by correlation functions: application to the precipitation in Al–Zn–Mg–Cu. Scr. Mater. 154, 106–110 (2018).
184. Gault B, Moody MP, Cairney JM & Ringer PS Atom probe crystallography. Mater. Today 15, 378–386 (2012).
185. Vurpillot F, De Geuser F, Da Costa G & Blavette D Application of Fourier transform and autocorrelation to cluster identification in the three-dimensional atom probe. J. Microsc. 216, 234–240 (2004). [PubMed: 15566495]
186. Yao L et al. Crystallographic structural analysis in atom probe microscopy via 3D Hough transformation. Ultramicroscopy 111, 458–463 (2011). [PubMed: 21146305]
187. Araullo-Peters VJ et al. A new systematic framework for crystallographic analysis of atom probe data. Ultramicroscopy 154, 7–14 (2015). [PubMed: 25747179]
188. Geiser BP et al. Spatial distribution maps for atom probe tomography. Microsc. Microanal. 13, 437–447 (2007). [PubMed: 18001510]
189. Boll T, Al-Kassab T, Yuan Y & Liu ZG Investigation of the site occupation of atoms in pure and doped TiAl/Ti3Al intermetallic. Ultramicroscopy 107, 796–801 (2007). [PubMed: 17482365]
190. Moody MP, Gault B, Stephenson LT, Haley D & Ringer SP Qualification of the tomographic reconstruction in atom probe by advanced spatial distribution map techniques. Ultramicroscopy 109, 815–824 (2009). [PubMed: 19362421]
191. Moody MP, Tang F, Gault B, Ringer SP & Cairney JM Atom probe crystallography: characterization of grain boundary orientation relationships in nanocrystalline aluminium. Ultramicroscopy 111, 493–499 (2011). [PubMed: 21146304]
192. Gault B et al. Advances in the calibration of atom probe tomographic reconstruction. J. Appl. Phys. 105, 34913 (2009).
193. Vurpillot F, Da Costa G, Menand A & Blavette D Structural analyses in three-dimensional atom probe: a Fourier approach. J. Microsc. 203, 295–302 (2001). [PubMed: 11555147]
194. Gault B et al. Spatial resolution in atom probe tomography. Microsc. Microanal. 16, 99–110 (2010). [PubMed: 20082732]
195. Ringer SP Advanced nanostructural analysis of aluminium alloys using atom probe tomography. Mater. Sci. Forum 519–521, 25–34 (2006).
196. Blavette D, Cadel E & Deconihout B The role of the atom probe in the study of nickel-based superalloys. Mater. Charact. 44, 133–157 (2000).
197. Blavette D, Cadel E, Pareige C, Deconihout B & Caron P Phase transformation and segregation to lattice defects in Ni-base superalloys. Microsc. Microanal. 13, 464–483 (2007). [PubMed: 18001512]
198. Seidman DN, Sudbrack CK & Yoon KE The use of 3-D atom-probe tomography to study nickel-based superalloys. JOM 58, 34–39 (2006).
199. Klein T, Clemens H & Mayer S Advancement of compositional and microstructural design of intermetallic γ-TiAl based alloys determined by atom probe tomography. Materials (Basel). 9, 755 (2016). [PubMed: 28773880]
200. Borchers C & Kirchheim R Cold-drawn pearlitic steel wires. Prog. Mater. Sci. 82, 405–444 (2016).
201. Raabe D et al. Grain boundary segregation engineering in metallic alloys: a pathway to the design of interfaces. Curr. Opin. Solid. State Mater. Sci. 18, 253–261 (2014).
202. Manzoni AM & Glatzel U New multiphase compositionally complex alloys driven by the high entropy alloy approach. Mater. Charact. 147, 512–532 (2019).

203. Marquis EA et al. Nuclear reactor materials at the atomic scale. Mater. Today 12, 30–37 (2009).
204. Marquis EA et al. On the current role of atom probe tomography in materials characterization and materials science. Curr. Opin. Solid. State Mater. Sci. 17, 217–223 (2013).
205. Ardell AJ & Bellon P Radiation-induced solute segregation in metallic alloys. Curr. Opin. Solid. State Mater. Sci. 20, 115–139 (2016).
206. Yu Y et al. Revealing nano-chemistry at lattice defects in thermoelectric materials using atom probe tomography. Mater. Today 32, 260–274 (2020).
207. Giddings AD et al. Industrial application of atom probe tomography to semiconductor devices. Scr. Mater. 148, 82–90 (2018).
208. Vandervorst W et al. Dopant, composition and carrier profiling for 3D structures. Mater. Sci. Semicond. Process. 62, 31–48 (2017).
209. Chang AS & Lauhon LJ Atom probe tomography of nanoscale architectures in functional materials for electronic and photonic applications. Curr. Opin. Solid. State Mater. Sci. 22, 171–187 (2018).
210. Rigutti L, Bonef B, Speck J, Tang F & Oliver RA Atom probe tomography of nitride semiconductors. Scr. Mater. 148, 75–81 (2017).
211. Saxey DW, Moser DE, Piazolo S, Reddy SM & Valley JW Atomic worlds: current state and future of atom probe tomography in geoscience. Scr. Mater. 148, 115–121 (2018). This brief critical review article discusses the application of APT to geological materials, and what the technique can provide in this context.
212. Verberne R et al. The geochemical and geochronological implications of nanoscale trace-element clusters in rutile. Geology 48, 1126–1130 (2020).
213. Marceau RKW, Sha G, Lumley RN & Ringer SP Evolution of solute clustering in Al–Cu– Mg alloys during secondary ageing. Acta Mater. 58, 1795–1805 (2010).
214. Medrano S et al. Cluster hardening in Al–3Mg triggered by small Cu additions. Acta Mater. 161, 12–20 (2018).
215. Bachhav M, Robert Odette G & Marquis EA α′ precipitation in neutron-irradiated Fe–Cr alloys. Scr. Mater. 74, 48–51 (2014).
216. Li T et al. New insights into the phase transformations to isothermal ω and ω-assisted α in near β-Ti alloys. Acta Mater. 106, 353–366 (2016).
217. Cojocaru-Miredin O, Cadel E, Vurpillot F, Mangelinck D & Blavette D Three-dimensional atomic-scale imaging of boron clusters in implanted silicon. Scr. Mater. 60, 285–288 (2009).
218. Duguay S et al. Evidence of atomic-scale arsenic clustering in highly doped silicon. J. Appl. Phys. 106, 106102 (2009).
219. Ronsheim P et al. Impurity measurements in silicon with D-SIMS and atom probe tomography. Appl. Surf. Sci. 255, 1547–1550 (2008).
220. Marceau RKW, Ceguerra AV, Breen AJ, Raabe D & Ringer SP Quantitative chemical-structure evaluation using atom probe tomography: short-range order analysis of Fe–Al. Ultramicroscopy 157, 12–20 (2015). [PubMed: 26000963]
221. Marquis EA & Vurpillot F Chromatic aberrations in the field evaporation behavior of small precipitates. Microsc. Microanal. 14, 561–570 (2008). [PubMed: 18986609]
222. Thompson K, Booske JH, Larson DJ & Kelly TF Three-dimensional atom mapping of dopants in Si nanostructures. Appl. Phys. Lett. 87, 52108 (2005).
223. Schwarz T et al. Correlative transmission Kikuchi diffraction and atom probe tomography study of Cu(In,Ga)Se2 grain boundaries. Prog. Photovolt. Res. Appl. 26, 196–204 (2018).
224. Schwarz T, Lomuscio A, Siebentritt S & Gault B On the chemistry of grain boundaries in CuInS2 films. Nano Energy 76, 105081 (2020).
225. Stoffers A et al. Complex nanotwin substructure of an asymmetric Σ9 tilt grain boundary in a silicon polycrystal. Phys. Rev. Lett. 115, 235502 (2015). [PubMed: 26684123]
226. Raghuwanshi M, Wuerz R & Cojocaru-Mirédin O Interconnection between trait, structure, and composition of grain boundaries in Cu(In,Ga)Se2 thin-film solar cells. Adv. Funct. Mater. 30, 1–9 (2020).

227. Dyck O et al. Accurate quantification of Si/SiGe interface profiles via atom probe tomography. Adv. Mater. Interfaces 4, 1700622 (2017).
228. Mangelinck D et al. Atom probe tomography for advanced metallization. Microelectron. Eng. 120, 19–33 (2014).
229. Panciera F et al. Three dimensional distributions of arsenic and platinum within NiSi contact and gate of an n-type transistor. Appl. Phys. Lett. 99, 51911 (2011).
230. Panciera F et al. Ni(Pt)-silicide contacts on CMOS devices: impact of substrate nature and Pt concentration on the phase formation. Microelectron. Eng. 120, 34–40 (2014).
231. Shimizu Y et al. Impact of carbon coimplantation on boron behavior in silicon: carbon–boron coclustering and suppression of boron diffusion. Appl. Phys. Lett. 98, 232101 (2011).
232. Inoue K et al. Dopant distributions in n-MOSFET structure observed by atom probe tomography. Ultramicroscopy 109, 1479–1484 (2009). [PubMed: 19775815]
233. Tang F et al. Indium clustering in *a*-plane InGaN quantum wells as evidenced by atom probe tomography. Appl. Phys. Lett. 106, 072104 (2015).
234. Galtrey MJ et al. Three-dimensional atom probe studies of an $In_xGa_{1-x}N$/GaN multiple quantum well structure: assessment of possible indium clustering. Appl. Phys. Lett. 90, 61903 (2007).
235. Riley JR et al. Three-dimensional mapping of quantum wells in a GaN/InGaN core-shell nanowire light-emitting diode array. Nano Lett. 13, 4317–4325 (2013). [PubMed: 23919559]
236. Gorman BP et al. in 2011 37th IEEE Photovoltaic Specialists Conf. 3357–3359 (IEEE, 2011).
237. Dietrich J et al. Origins of electrostatic potential wells at dislocations in polycrystalline Cu(In,Ga)Se2 thin films. J. Appl. Phys. 115, 103507 (2014).
238. Cojocaru-Mirédin O et al. Interface engineering and characterization at the atomic-scale of pure and mixed ion layer gas reaction buffer layers in chalcopyrite thin-film solar cells. Prog. Photovoltaics Res. Appl. 23, 705–716 (2014).
239. Larson DJ, Petford-Long AK, Ma YQ & Cerezo A Information storage materials: nanoscale characterisation by three-dimensional atom probe analysis. Acta Mater. 52, 2847–2862 (2004).
240. Vovk V, Schmitz G, Hutten A & Heitmann S Mismatch-induced recrystallization of giant magneto-resistance (GMR) multilayer systems. Acta Mater. 55, 3033–3047 (2007).
241. Gault B et al. High-resolution nanostructural investigation of Zn4Sb3 alloys. Scr. Mater. 63, 784–787 (2010).
242. Yu Y et al. Ag-segregation to dislocations in PbTe-based thermoelectric materials. ACS Appl. Mater. Interfaces 10, 3609–3615 (2018). [PubMed: 29309116]
243. Gomell L et al. Properties and influence of microstructure and crystal defects in Fe2VAl modified by laser surface remelting. Scr. Mater. 193, 153–157 (2021).
244. Krakauer BW & Seidman DN Absolute atomic-scale measurements of the Gibbsian interfacial excess of solute at internal interfaces. Phys. Rev. B 48, 6724–6727 (1993).
245. Jia Y et al. L10 rare-earth-free permanent magnets: the effects of twinning versus dislocations in Mn–Al magnets. Phys. Rev. Mater. 4, 094402 (2020).
246. Herbig M et al. Grain boundary segregation in Fe–Mn–C twinning-induced plasticity steels studied by correlative electron backscatter diffraction and atom probe tomography. Acta Mater. 83, 37–47 (2015).
247. Cantwell PR et al. Grain boundary complexion transitions. Annu. Rev. Mater. Res. 50, 465–492 (2020).
248. Peter NJ et al. Segregation-induced nanofaceting transition at an asymmetric tilt grain boundary in copper. Phys. Rev. Lett. 121, 255502 (2018). [PubMed: 30608793]
249. Zhao H et al. Interplay of chemistry and faceting at grain boundaries in a model Al alloy. Phys. Rev. Lett. 124, 106102 (2020). [PubMed: 32216435]
250. Kwiatkowski da Silva A et al. Phase nucleation through confined spinodal fluctuations at crystal defects evidenced in Fe–Mn alloys. Nat. Commun. 9, 1137 (2018). [PubMed: 29555984]
251. Chang L, Barnard SJ & Smith GDW in Gilbert R. Speich Symp. Proc.: Fundamentals of Aging and Tempering in Bainitic and Martensitic Steel Products (eds Krauss G & Repas PE) 19–28 (Iron and Steel Society, 1992).

252. Blavette D, Cadel E, Fraczkeiwicz A & Menand A Three-dimensional atomic-scale imaging of impurity segregation to line defects. Science 286, 2317–2319 (1999). [PubMed: 10600736]
253. Thompson K, Flaitz PL, Ronsheim P, Larson DJ & Kelly TF Imaging of arsenic Cottrell atmospheres around silicon defects by three-dimensional atom probe tomography. Science 317, 1370–1374 (2007). [PubMed: 17823348]
254. Hoummada K, Mangelinck D, Gault B & Cabié M Nickel segregation on dislocation loops in implanted silicon. Scr. Mater. 64, 378–381 (2011).
255. Zhou X et al. The hidden structure dependence of the chemical life of dislocations. Sci. Adv. 7, eabf0563 (2021). [PubMed: 33863726]
256. Williams CA, Hyde JM, Smith GDW & Marquis EA Effects of heavy-ion irradiation on solute segregation to dislocations in oxide-dispersion-strengthened Eurofer 97 steel. J. Nucl. Mater. 412, 100–105 (2011).
257. Bachhav M, Yao L, Robert Odette G & Marquis EA Microstructural changes in a neutron-irradiated Fe–6 at.%Cr alloy. J. Nucl. Mater. 453, 334–339 (2014).
258. Felfer P, Ceguerra A, Ringer S & Cairney J Applying computational geometry techniques for advanced feature analysis in atom probe data. Ultramicroscopy 132, 100–106 (2013). [PubMed: 23623291]
259. Kuzmina M, Herbig M, Ponge D, Sandlobes S & Raabe D Linear complexions: confined chemical and structural states at dislocations. Science 349, 1080–1083 (2015). [PubMed: 26339026]
260. Abou-Ras D et al. Compositional and electrical properties of line and planar defects in Cu(In,Ga)Se2 thin films for solar cells—a review. Phys. Status Solidi Rapid Res. Lett. 10, 363–375 (2016).
261. Makineni SK et al. On the diffusive phase transformation mechanism assisted by extended dislocations during creep of a single crystal CoNi-based superalloy. Acta Mater. 155, 362–371 (2018).
262. Cadel E, Lemarchand D, Gay A-S, Fraczkiewicz A & Blavette D Atomic scale investigation of boron nanosegregation in FeAl intermetallics. Scr. Mater. 41, 421–426 (1999).
263. Herschitz R & Seidman DN Atomic resolution observations of solute-atom segregation effects and phase transitions in stacking faults in dilute cobalt alloys—I. Experimental results. Acta Metall. 33, 1547–1563 (1985).
264. Makineni SK et al. Elemental segregation to antiphase boundaries in a crept CoNi-based single crystal superalloy. Scr. Mater. 157, 62–66 (2018).
265. Gomell L et al. Chemical segregation and precipitation at anti-phase boundaries in thermoelectric Heusler-Fe2VAl. Scr. Mater. 186, 370–374 (2020).
266. Marceau RKW et al. Multi-scale correlative microscopy investigation of both structure and chemistry of deformation twin bundles in Fe–Mn–C steel. Microsc. Microanal. 19, 1581–1585 (2013). [PubMed: 24103578]
267. Barba D et al. On the composition of microtwins in a single crystal nickel-based superalloy. Scr. Mater. 127, 37–40 (2017).
268. Antonov S, Li B, Gault B & Tan Q The effect of solute segregation to deformation twin boundaries on the electrical resistivity of a single-phase superalloy. Scr. Mater. 186, 208–212 (2020).
269. Palanisamy D, Raabe D & Gault B Elemental segregation to twin boundaries in a MnAl ferromagnetic Heusler alloy. Scr. Mater. 155, 144–148 (2018).
270. Palanisamy D, Raabe D & Gault B On the compositional partitioning during phase transformation in a binary ferromagnetic MnAl alloy. Acta Mater. 174, 227–236 (2019).
271. He J et al. On the atomic solute diffusional mechanisms during compressive creep deformation of a Co–Al–W–Ta single crystal superalloy. Acta Mater. 184, 86–99 (2020).
272. Auger P, Pareige P, Welzel S & Van Duysen JC Synthesis of atom probe experiments on irradiation-induced solute segregation in French ferritic pressure vessel steels. J. Nucl. Mater. 280, 331–344 (2000).
273. Miller MK, Sokolov MA, Nanstad RK & Russell KF APT characterization of high nickel RPV steels. J. Nucl. Mater. 351, 187–196 (2006).

274. Williams CA, Marquis EA, Cerezo A & Smith GDW Nanoscale characterisation of ODS-Eurofer 97 steel: an atom-probe tomography study. J. Nucl. Mater. 400, 37–45 (2010).
275. Hyde JM, Ellis D, English CA & Williams TJ in Institution of Chemical Engineers Symposium Series (eds Rosinski S, Grossbeck M, Allen T & Kumar A) 262–288 (ASTM International, 2000).
276. Takeuchi T et al. Effects of neutron irradiation on microstructures and hardness of stainless steel weld-overlay cladding of nuclear reactor pressure vessels. J. Nucl. Mater. 449, 273–276 (2014).
277. Meisnar M, Moody M & Lozano-Perez S Atom probe tomography of stress corrosion crack tips in SUS316 stainless steels. Corros. Sci. 98, 661–671 (2015).
278. Lozano-Perez S, Kruska K, Iyengar I, Terachi T & Yamada T The role of cold work and applied stress on surface oxidation of 304 stainless steel. Corros. Sci. 56, 78–85 (2012).
279. Schreiber DK et al. Examinations of oxidation and sulfidation of grain boundaries in alloy 600 exposed to simulated pressurized water reactor primary water. Microsc. Microanal. 19, 676–687 (2013). [PubMed: 23590826]
280. Hudson D & Smith GDW Initial observation of grain boundary solute segregation in a zirconium alloy (ZIRLO) by three-dimensional atom probe. Scr. Mater. 61, 411–414 (2009).
281. Dong Y, Motta AT & Marquis EA Atom probe tomography study of alloying element distributions in Zr alloys and their oxides. J. Nucl. Mater. 442, 270–281 (2013).
282. Gin S, Ryan JV, Schreiber DK, Neeway J & Cabié M Contribution of atom-probe tomography to a better understanding of glass alteration mechanisms: application to a nuclear glass specimen altered 25years in a granitic environment. Chem. Geol. 349–350, 99–109 (2013).
283. He LF et al. Bubble formation and Kr distribution in Kr-irradiated UO_2. J. Nucl. Mater. 456, 125–132 (2015).
284. Edmondson PD, Parish CM, Zhang Y, Hallén A & Miller MK Helium entrapment in a nanostructured ferritic alloy. Scr. Mater. 65, 731–734 (2011).
285. Gemma R, Al-Kassab T, Kirchheim R & Pundt A Studies on hydrogen loaded V–Fe8 at% films on Al2O3 substrate. J. Alloy. Compd. 446–447, 534–538 (2007).
286. Takahashi J, Kawakami K, Kobayashi Y & Tarui T The first direct observation of hydrogen trapping sites in TiC precipitation-hardening steel through atom probe tomography. Scr. Mater. 63, 261–264 (2010).
287. Mouton I et al. Quantification challenges for atom probe tomography of hydrogen and deuterium in Zircaloy-4. Microsc. Microanal. 25, 481–488 (2018).
288. Chang YH et al. Quantification of solute deuterium in titanium deuteride by atom probe tomography with both laser pulsing and high-voltage pulsing: Influence of the surface electric field. N. J. Phys. 21, 053025 (2019).
289. Breen AJ, Stephenson LT, Sun B, Li Y & Kasian O Solute hydrogen and deuterium observed at the near atomic scale in high-strength steel. Acta Mater. 188, 108–120 (2020).
290. Takahashi J, Kawakami K & Kobayashi Y Origin of hydrogen trapping site in vanadium carbide precipitation strengthening steel. Acta Mater. 153, 193–204 (2018).
291. Breen AJ et al. Atomic scale analysis of grain boundary deuteride growth front in Zircaloy-4. Scr. Mater. 156, 42–46 (2018).
292. Chang Y et al. Characterizing solute hydrogen and hydrides in pure and alloyed titanium at the atomic scale. Acta Mater. 150, 273–280 (2018).
293. Mouton I et al. Hydride growth mechanism in zircaloy-4: investigation of the partitioning of alloying elements. Materialia 15, 101006 (2021).
294. Miller MK & Russell KF An APFIM investigation of a weathered region of the Santa Catharina meteorite. Surf. Sci. 266, 441–445 (1992).
295. Kuhlman KR, Martens RL, Kelly TF, Evans ND & Miller MK Fabrication of specimens of metamorphic magnetite crystals for field ion microscopy and atom probe microanalysis. Ultramicroscopy 89, 169–176 (2001). [PubMed: 11770743]
296. Valley JW et al. Nano-and micro-geochronology in Hadean and Archean zircons by atom-probe tomography and SIMS: new tools for old minerals. Am. Mineral. 100, 1355–1377 (2015).

297. Reddy SM et al. Atom probe tomography: development and application to the geosciences. Geostand. Geoanalytical Res. 44, 5–50 (2020).
298. Fougerouse D et al. Nanoscale distribution of Pb in monazite revealed by atom probe microscopy. Chem. Geol. 479, 251–258 (2018).
299. Piazolo S et al. Deformation-induced trace element redistribution in zircon revealed using atom probe tomography. Nat. Commun. 7, 10490 (2016). [PubMed: 26868040]
300. Peterman EM et al. Nanoscale processes of trace element mobility in metamorphosed zircon. Contrib. Mineral. Petrol. 174, 92 (2019).
301. Blum TB et al. in Microstructural Geochronology: Planetary Records Down to Atom Scale Ch. 16 (eds, Moser DE, Corfu F, Darling JR, Reddy SM & Tait K) 327–350 (American Geophysical Union, 2018).
302. Arcuri GA, Moser DE, Reinhard DA, Langelier B & Larson DJ Impact-triggered nanoscale Pb clustering and Pb loss domains in Archean zircon. Contrib. Mineral. Petrol. 175, 59 (2020).
303. Moser DE et al. Decline of giant impacts on Mars by 4.48 billion years ago and an early opportunity for habitability. Nat. Geosci. 12, 522–527 (2019).
304. White LF et al. Nanoscale chemical characterisation of phase separation, solid state transformation, and recrystallization in feldspar and maskelynite using atom probe tomography. Contrib. Mineral. Petrol. 173, 87 (2018).
305. Blum TB et al. A nanoscale record of impact-induced Pb mobility in lunar zircon. Microsc. Microanal. 25, 2448–2449 (2019).
306. Greer J et al. Atom probe tomography of space-weathered lunar ilmenite grain surfaces. Meteorit. Planet. Sci. 55, 426–440 (2020).
307. Daly L et al. Nebula sulfidation and evidence for migration of “free-floating” refractory metal nuggets revealed by atom probe microscopy. Geology 45, 847–850 (2017).
308. Lewis JB, Isheim D, Floss C & Seidman DN C12/C13-ratio determination in nanodiamonds by atom-probe tomography. Ultramicroscopy 159, 248–254 (2015). [PubMed: 26095824]
309. Dubosq R, Rogowitz A, Schweinar K, Gault B & Schneider DADAA 2D and 3D nanostructural study of naturally deformed pyrite: assessing the links between trace element mobility and defect structures. Contrib. Mineral. Petrol. 174, 72 (2019).
310. Fougerouse D et al. Time-resolved, defect-hosted, trace element mobility in deformed Witwatersrand pyrite. Geosci. Front. 10, 55–63 (2019).
311. Wu Y-F et al. Gold, arsenic, and copper zoning in pyrite: a record of fluid chemistry and growth kinetics. Geology 47, 641–644 (2019).
312. Gopon P, Douglas JO, Wade J & Moody MP Complementary SEM-EDS/FIB-SEM sample preparation techniques for atom probe tomography of nanophase-Fe0 in apollo 16 regolith sample 61501,22. Microsc. Microanal. 25, 2544–2545 (2019).
313. Cao M et al. Micro- and nano-scale textural and compositional zonation in plagioclase at the Black Mountain porphyry Cu deposit: implications for magmatic processes. Am. Mineral. 104, 391–402 (2019).
314. Parman SW, Diercks DR, Gorman BP & Cooper RF Atom probe tomography of isoferroplatinum. Am. Min. 100, 852–860 (2015).
315. Dubosq R, Rogowitz A, Schneider DA, Schweinar K & Gault B Fluid inclusion induced hardening: nanoscale evidence from naturally deformed pyrite. Contrib. Mineral. Petrol. 176, 15 (2021).
316. Petrishcheva E et al. Spinodal decomposition in alkali feldspar studied by atom probe tomography. Phys. Chem. Miner. 47, 30 (2020). [PubMed: 32624637]
317. Honour VC et al. Compositional boundary layers trigger liquid unmixing in a basaltic crystal mush. Nat. Commun. 10, 4821 (2019). [PubMed: 31645560]
318. Schipper CI et al. Volcanic SiO_2-cristobalite: a natural product of chemical vapor deposition. Am. Mineral. 105, 510–524 (2020).
319. Taylor SD et al. Resolving Iron(II) sorption and oxidative growth on hematite (001) using atom probe tomography. J. Phys. Chem. C. 122, 3903–3914 (2018).

320. Taylor SD et al. Visualizing the iron atom exchange front in the Fe(II)-catalyzed recrystallization of goethite by atom probe tomography. Proc. Natl Acad. Sci. USA 116, 2866–2874 (2019). [PubMed: 30733289]
321. Bloch EM et al. Diffusion of calcium in forsterite and ultra-high resolution of experimental diffusion profiles in minerals using local electrode atom probe tomography. Geochim. Cosmochim. Acta 265, 85–95 (2019).
322. Cukjati JT et al. Differences in chemical thickness of grain and phase boundaries: an atom probe tomography study of experimentally deformed wehrlite. Phys. Chem. Miner. 46, 845–859 (2019).
323. Montalvo SD et al. Nanoscale constraints on the shock-induced transformation of zircon to reidite. Chem. Geol. 507, 85–95 (2019).
324. Rout SS et al. Atom-probe tomography and transmission electron microscopy of the kamacite–taenite interface in the fast-cooled Bristol IVA iron meteorite. Meteorit. Planet. Sci. 52, 2707–2729 (2017).
325. Gamal El Dien H et al. Cr-spinel records metasomatism not petrogenesis of mantle rocks. Nat. Commun. 10, 5103 (2019). [PubMed: 31704918]
326. Genareau K, Perez-Huerta A & Laiginhas F Atom probe tomography analysis of exsolved mineral phases. J. Vis. Exp. 2019, e59863 (2019).
327. Visart de Bocarmé T, Chau T-D & Kruse N Dynamic interaction of CO/H_2O mixtures with gold nanocrystals: real-time imaging and local chemical probing. Surf. Sci. 600, 4205–4210 (2006).
328. Visart de Bocarmé T, Beketov G & Kruse N Water formation from O_2 and H_2 on Rh tips: studies by field ion microscopy and pulsed field desorption mass spectrometry. in. Surf. Interface Anal. 36, 522–527 (2004).
329. Kruse N, Schweicher J, Bundhoo A, Frennet A & Visart de Bocarmé T Catalytic CO hydrogenation: mechanism and kinetics from chemical transients at low and atmospheric pressures. Top. Catal. 48, 145–152 (2008).
330. Barroo C, Akey AJ & Bell DC Atom probe tomography for catalysis applications: a review. Appl. Sci. 9, 2721 (2019).
331. Perea DE et al. Determining the location and nearest neighbours of aluminium in zeolites with atom probe tomography. Nat. Commun. 6, 7589 (2015). [PubMed: 26133270]
332. Schmidt JE, Peng L, Poplawsky JD & Weckhuysen BM Nanoscale chemical imaging of zeolites using atom probe tomography. Angew. Chem. Int. Ed. 57, 10422–10435 (2018).
333. Ji Z, Li T & Yaghi OM Sequencing of metals in multivariate metal–organic frameworks. Science 369, 674–680 (2020). [PubMed: 32764067]
334. El-Zoka AA, Langelier B, Korinek A, Botton GA & Newman RC Nanoscale mechanism of the stabilization of nanoporous gold by alloyed platinum. Nanoscale 10, 4904–4912 (2018). [PubMed: 29480291]
335. El-Zoka AA, Langelier B, Botton GA & Newman RC Enhanced analysis of nanoporous gold by atom probe tomography. Mater. Charact. 128, 269–277 (2017).
336. Li T et al. Atomic-scale insights into surface species of electrocatalysts in three dimensions. Nat. Catal. 1, 300–305 (2018).
337. Kasian O et al. Degradation of iridium oxides via oxygen evolution from the lattice: correlating atomic scale structure with reaction mechanisms. Energy Environ. Sci. 12, 3548–3555 (2019).
338. Schweinar K et al. Probing catalytic surfaces by correlative scanning photoemission electron microscopy and atom probe tomography. J. Mater. Chem. A 8, 388–400 (2019).
339. Gordon LM & Joester D Nanoscale chemical tomography of buried organic-inorganic interfaces in the chiton tooth. Nature 469, 194–197 (2011). [PubMed: 21228873]
340. Gordon LM et al. Amorphous intergranular phases control the properties of rodent tooth enamel. Science 347, 746–750 (2015). [PubMed: 25678658]
341. La Fontaine A et al. Atomic-scale compositional mapping reveals Mg-rich amorphous calcium phosphate in human dental enamel. Sci. Adv. 2, e1601145 (2016). [PubMed: 27617291]
342. Branson O et al. Nanometer-scale chemistry of a calcite biomineralization template: implications for skeletal composition and nucleation. Proc. Natl Acad. Sci. USA 113, 12934 LP–12912939 (2016). [PubMed: 27794119]

343. Eder K, Otter LM, Yang L, Jacob DE & Cairney JM Overcoming challenges associated with the analysis of nacre by atom probe tomography. Geostand. Geoanalytical Res. 43, 385–395 (2019).
344. Langelier B, Wang X & Grandfield K Atomic scale chemical tomography of human bone. Sci. Rep. 7, 1–9 (2017). [PubMed: 28127051]
345. Gordon LM, Tran L & Joester D Atom probe tomography of apatites and bone-type mineralized tissues. ACS Nano 6, 10667–10675 (2012). [PubMed: 23176319]
346. Pérez-Huerta A & Laiginhas F Preliminary data on the nanoscale chemical characterization of the intercrystalline organic matrix of a calcium carbonate biomineral. Minerals 8, 223 (2018).
347. Pérez-Huerta A, Suzuki M, Cappelli C, Laiginhas F & Kintsu H Atom probe tomography (APT) characterization of organics occluded in single calcite crystals: implications for biomineralization studies. C. J. Carbon Res. 5, 50 (2019).
348. Nishikawa O, Taniguchi M, Watanabe S, Yamagishi A & Sasaki T Scanning atom probe study of dissociation of organic molecules on titanium oxide. Jpn. J. Appl. Phys. 45, 1892–1896 (2006).
349. Proudian AP et al. Effect of diels-alder reaction in C60-tetracene photovoltaic devices. Nano Lett. 16, 6086–6091 (2016). [PubMed: 27575667]
350. Proudian AP, Jaskot MB, Diercks DR, Gorman BP & Zimmerman JD Atom probe tomography of molecular organic materials: sub-dalton nanometer-scale quantification. Chem. Mater. 31, 2241–2247 (2019).
351. Eder K et al. A new approach to understand the adsorption of thiophene on different surfaces: an atom probe investigation of self-assembled monolayers. Langmuir 33, 9573–9581 (2017). [PubMed: 28829146]
352. Mohanty SK & Tolochko O An atom probe analysis of self-assembled monolayers: a novel approach to investigate mixed and unmixed self-assembled monolayers (SAMs) on gold. Appl. Surf. Sci. 494, 152–161 (2019).
353. Wang LRC, Kreuzer HJ & Nishikawa O Polythiophene in strong electrostatic fields. Org. Electron. 7, 99–106 (2006).
354. Nickerson BS, Karahka M & Kreuzer HJ Disintegration and field evaporation of thiolate polymers in high electric fields. Ultramicroscopy 159, 173–177 (2015). [PubMed: 25825029]
355. Nishikawa O, Taniguchi M & Saito Y Study of characteristic fragmentation of nanocarbon by the scanning atom probe. J. Vac. Sci. Technol. A 26, 1074 (2008).
356. Graham WR & Hutchins F Field-Ion microscopy of DNA and RNA. Bull. Am. Phys. Soc. 18, 296 (1973).
357. Panitz JA & Giaever I Ferritin deposition on field-emitter tips. Ultramicroscopy 6, 3–6 (1981).
358. Greene M, Prosa TJ, Larson DJ & Kelly TF Focused Ion beam fabrication of solidified ferritin into nanoscale volumes for compositional analysis using time-of-flight mass spectrometry methods. Microsc. Microanal. 16, 1860–1861 (2010).
359. Perea DE et al. Atom probe tomographic mapping directly reveals the atomic distribution of phosphorus in resin embedded ferritin. Sci. Rep. 6, 1–9 (2016). [PubMed: 28442746]
360. Rusitzka KAK et al. A near atomic-scale view at the composition of amyloid-β fibrils by atom probe tomography. Sci. Rep. 8, 1–10 (2018). [PubMed: 29311619]
361. Narayan K, Prosa TJ, Fu J, Kelly TF & Subramaniam S Chemical mapping of mammalian cells by atom probe tomography. J. Struct. Biol. 178, 98–107 (2012). [PubMed: 22245777]
362. Adineh VR, Marceau RKW, Velkov T, Li J & Fu J Near-atomic three-dimensional mapping for site-specific chemistry of ‘Superbugs’. Nano Lett. 16, 7113–7120 (2016). [PubMed: 27650306]
363. Sundell G, Hulander M, Pihl A & Andersson M Atom probe tomography for 3D structural and chemical analysis of individual proteins. Small 15, 1900316 (2019).
364. McCarroll IE, Bagot PAJ, Devaraj A, Perea DE & Cairney JM New frontiers in atom probe tomography: a review of research enabled by cryo and/or vacuum transfer systems. Mater. Today Adv. 7, 100090 (2020). [PubMed: 33103106] This short review article discusses the developments and new applications in cryogenic transfer and cryogenic APT.
365. Blum TB et al. in Microscructural Geochronology: Planetary Records Down to Atom Scale Ch. 18 (eds Moser DE, Corfu F, Darling JR, Reddy SM & Tait K) 369–373 (American Geophysical Union, 2017).

366. Haley D, London AJ & Moody MP Processing APT spectral backgrounds for improved quantification. Microsc. Microanal. 26, 964–977 (2020). [PubMed: 32811592]

367. Kühbach M et al. Building a library of simulated atom probe data for different crystal structures and tip orientations using TAPSim. Microsc. Microanal. 25, 320–330 (2019). [PubMed: 30773167]

368. Cairney JM et al. Mining information from atom probe data. Ultramicroscopy 159, 324–337 (2015). [PubMed: 26095825]

369. Ceguerra AVAV et al. The rise of computational techniques in atom probe microscopy. Curr. Opin. Solid. State Mater. Sci. 17, 224–235 (2013).

370. Kühbach M, Bajaj P, Çelik MH, Jägle EA & Gault B On strong scaling and open source tools for analyzing atom probe tomography data. Preprint at https://arxiv.org/abs/2004.05188 (2020).

371. Keutgen J, London AJ & Cojocaru-Mirédin O Solving peak overlaps for proximity histogram analysis of complex interfaces for atom probe tomography data. Microsc. Microanal. 27, 28–35 (2020).

372. Exertier F et al. Atom probe tomography analysis of the reference zircon GJ-1: an interlaboratory study. Chem. Geol. 495, 27–35 (2018).

373. Diercks DR, Gorman BP & Gerstl SSA An open-access atom probe tomography mass spectrum database. Microsc. Microanal. 23, 664–665 (2017).

374. Kelly TF, Geiser BP & Larson DJ Definition of spatial resolution in atom probe tomography. Microsc. Microanal. 13, 1604–1605 (2007).

375. Gault B et al. Origin of the spatial resolution in atom probe microscopy. Appl. Phys. Lett. 95, 34103 (2009).

376. Cadel E, Vurpillot F, Larde R, Duguay S & Deconihout B Depth resolution function of the laser assisted tomographic atom probe in the investigation of semiconductors. J. Appl. Phys. 106, 44908 (2009).

377. Gault B et al. Influence of the wavelength on the spatial resolution of pulsed-laser atom probe. J. Appl. Phys. 110, 94901 (2011).

378. Hyde JM, Cerezo A, Setna RP, Warren PJ & Smith GDW Lateral and depth scale calibration of the position sensitive atom probe. Appl. Surf. Sci. 76–77, 382–391 (1994).

379. Gault B et al. Dynamic reconstruction for atom probe tomography. Ultramicroscopy 111, 1619–1624 (2011). [PubMed: 21946002]

380. Gault B, La Fontaine A, Moody MP, Ringer SP & Marquis EA Impact of laser pulsing on the reconstruction in an atom probe tomography. Ultramicroscopy 110, 1215–1222 (2010). [PubMed: 20471173]

381. Moore AJW & Spink JA Influence of surface coordination on field evaporation processes in tungsten. Surf. Sci. 44, 198–212 (1974).

382. Vurpillot F & Oberdorfer C Modeling atom probe tomography: a review. Ultramicroscopy 159, 202–216 (2015). [PubMed: 25720335] This article presents an overview of image simulations and field evaporation modelling techniques.

383. Sanchez CG, Lozovoi AY & Alavi A Field-evaporation from first-principles. Mol. Phys. 102, 1045–1055 (2004).

384. Ashton M, Mishra A, Neugebauer J & Freysoldt C Ab initio description of bond breaking in large electric fields. Phys. Rev. Lett. 124, 176801 (2020). [PubMed: 32412263] This article presents a new development of density-functional theory and its application to describe the field evaporation process ab initio.

385. Prokoshkina D, Esin VA, Wilde G & Divinski SV Grain boundary width, energy and self-diffusion in nickel: effect of material purity. Acta Mater. 61, 5188–5197 (2013).

386. Mistler RE & Coble RL Grain-boundary diffusion and boundary widths in metals and ceramics. J. Appl. Phys. 45, 1507–1509 (1974).

387. Chellali MR et al. Triple junction transport and the impact of grain boundary width in nanocrystalline Cu. Nano Lett. 12, 3448–3454 (2012). [PubMed: 22657752]

388. Danoix F, Grancher G, Bostel A & Blavette D Standard deviations of composition measurements in atom probe analyses. Part I conventional 1D atom probe. Ultramicroscopy 107, 734–738 (2007). [PubMed: 17493755]
389. Gault B et al. Behavior of molecules and molecular ions near a field emitter. N. J. Phys. 18, 33031 (2016).
390. Sundell G, Thuvander M & Andrén H-O Hydrogen analysis in APT: methods to control adsorption and dissociation of H2. Ultramicroscopy 132, 285–289 (2013). [PubMed: 23489909]
391. Gault B, Danoix F, Hoummada K, Mangelinck D & Leitner H Impact of directional walk on atom probe microanalysis. Ultramicroscopy 113, 182–191 (2012).
392. Wang SC & Tsong TT Field and temperature-dependence of the directional walk of single adsorbed W-atoms on the W(110) plane. Phys. Rev. B 26, 6470–6475 (1982).
393. Marquis EA, Geiser BP, Prosa TJ & Larson DJ Evolution of tip shape during field evaporation of complex multilayer structures. J. Microsc. 241, 225–233 (2011). [PubMed: 21118216]
394. Felfer PJ et al. A new approach to the determination of concentration profiles in atom probe tomography. Microsc. Microanal. 18, 359–364 (2012). [PubMed: 22300727]
395. Sauvage X et al. Solid state amorphization in cold drawn Cu/Nb wires. Acta Mater. 49, 389–394 (2001).
396. Gault B et al. Atom probe tomography and transmission electron microscopy characterisation of precipitation in an Al–Cu–Li–Mg–Ag alloy. Ultramicroscopy 111, 683–689 (2011). [PubMed: 21239117]
397. De Geuser F et al. An improved reconstruction procedure for the correction of local magnification effects in three-dimensional atom-probe. Surf. Interface Anal. 39, 268–272 (2007).
398. Kelly TF, Miller MK, Rajan K & Ringer SP Atomic-scale tomography: a 2020 vision. Microsc. Microanal. 19, 652–664 (2013). [PubMed: 23668837]
399. Kirchhofer R, Diercks DR & Gorman BP Electron diffraction and imaging for atom probe tomography. Rev. Sci. Instrum. 89, 053706 (2018). [PubMed: 29864799]
400. Schmitz G & Stender P Description: Method for preparation of needle tip for atom probe tomography, involves guiding through hole of planar drain electrode into measuring position based on measured coordinates of sample for performing tomography by manipulator. German patent DE102011119164 (2013).
401. Stender P, Ott J, Balla I & Schmitz G in NIST Special Publication 2100–03: Proc. Int. Conf. Atom Probe Tomography and Microscopy (APT&M 2018) (ed. NIST) 111 (NIST Special Publications, 2018).
402. Lambeets SV et al. Nanoscale perspectives of metal degradation via in situ atom probe tomography. Top. Catal. 63, 1606–1622 (2020).
403. Dumpala S, Broderick SR, Bagot PAJ & Rajan K An integrated high temperature environmental cell for atom probe tomography studies of gas-surface reactions: instrumentation and results. Ultramicroscopy 141, 16–21 (2014). [PubMed: 24704605]
404. Houard J et al. A photonic atom probe coupling 3D atomic scale analysis with in situ photoluminescence spectroscopy. Rev. Sci. Instrum. 91, 083704 (2020). [PubMed: 32872963]
405. Gorman B Hardware engineering for an APT in a TEM objective lens. Microsc. Microanal. 26, 2614–2615 (2020).
406. Kelly T, Dunin-Borkowski R & Meyer J Project Tomo: toward atomic-scale analytical tomography. Microsc. Microanal. 26, 2618–2621 (2020).
407. Walck SD & Hren JJ FIM/IAP/TEM studies of hydrogen in metals. J. Phys. 45, 355–360 (1984).
408. Medeiros JM et al. Robust workflow and instrumentation for cryo-focused ion beam milling of samples for electron cryotomography. Ultramicroscopy 190, 1–11 (2018). [PubMed: 29655973]
409. Gerstl SSA, Tacke S, Chen Y-S, Wagner J & Wepf R Enabling atom probe analyses of new materials classes with vacuum-cryo-transfer capabilities. Microsc. Microanal. 23, 612 (2017).
410. Stephenson LT et al. The Laplace project: an integrated suite for preparing and transferring atom probe samples under cryogenic and UHV conditions. PLoS ONE 13, 1–13 (2018).
411. Bagot PAJ, Visart de Bocarmé T, Cerezo A & Smith GDW 3D atom probe study of gas adsorption and reaction on alloy catalyst surfaces I: instrumentation. Surf. Sci. 600, 3028–3035 (2006).

412. Chiaramonti AN et al. A three-dimensional atom probe microscope incorporating a wavelength-tuneable femtosecond-pulsed coherent extreme ultraviolet light source. MRS Adv. 4, 2367–2375 (2019).
413. Chiaramonti AN et al. Field Ion emission in an atom probe microscope triggered by femtosecond-pulsed coherent extreme ultraviolet light. Microsc. Microanal. 26, 258–266 (2020). [PubMed: 32160938]
414. Viswanathan B, Drachsel W, Block JH & Tsong TT Photon enhanced field ionization on semiconductor surfaces. J. Chem. Phys. 70, 2582 (1979).
415. Suttle J et al. A superconducting ion detection scheme for atom probe tomography. APS March Meeting Abstracts 2016, Y7.003 (2016).
416. Bacchi C et al. Development of an energy-sensitive detector for the atom probe tomography. Preprint at https://arxiv.org/abs/2103.04765 (2021).
417. Vurpillot F et al. True atomic-scale imaging in three dimensions: a review of the rebirth of field-ion microscopy. Microsc. Microanal. 23, 1–11 (2017). [PubMed: 28162123]
418. Vurpillot F, Gilbert M & Deconihout B Towards the three-dimensional field ion microscope. Surf. Interface Anal. 39, 273–277 (2007).
419. Wille C, Al-Kassab T, Heinrich A & Kirchheim R in IVNC 2006/IFES 2006 17–18 (IEEE, 2006).
420. Dagan M, Gault B, Smith GDW, Bagot PAJ & Moody MP Automated atom-by-atom three-dimensional (3D) reconstruction of field ion microscopy data. Microsc. Microanal. 23, 255–268 (2017). [PubMed: 28318483]
421. Katnagallu S et al. Advanced data mining in field ion microscopy. Mater. Charact. 146, 307–318 (2018).
422. Klaes B et al. A model to predict image formation in the three-dimensional field ion microscope. Comput. Phys. Commun. 260, 107317 (2020).
423. Katnagallu S, Morgado FFF, Mouton I, Gault B & Stephenson LT Three-dimensional atomically-resolved analytical imaging with a field ion microscope. Preprint at https://arxiv.org/abs/2103.11010 (2021).
424. Silaeva EP, Uchida K, Suzuki Y & Watanabe K Energetics and dynamics of laser-assisted field evaporation: time-dependent density functional theory simulations. Phys. Rev. B Condens. Matter Mater. Phys. 92, 15540 (2015).
425. Vurpillot F, Bostel A & Blavette D Trajectory overlaps and local magnification in three-dimensional atom probe. Appl. Phys. Lett. 76, 3127–3129 (2000).
426. Oberdorfer C, Eich SM, Lütkemeyer M & Schmitz G Applications of a versatile modelling approach to 3D atom probe simulations. Ultramicroscopy 159, 184–194 (2015). [PubMed: 25736966]
427. Oberdorfer C et al. Influence of surface relaxation on solute atoms positioning within atom probe tomography reconstructions. Mater. Charact. 146, 324–335 (2018).
428. Larson DJ, Gault B, Geiser BP, De Geuser F & Vurpillot F Atom probe tomography spatial reconstruction: status and directions. Curr. Opin. Solid. State Mater. Sci. 17, 236–247 (2013). This critical review provides a perspective on the tomographic reconstruction process.
429. Beinke D, Oberdorfer C & Schmitz G Towards an accurate volume reconstruction in atom probe tomography. Ultramicroscopy 165, 34–41 (2016). [PubMed: 27062338]
430. Rolland N et al. An analytical model accounting for tip shape evolution during atom probe analysis of heterogeneous materials. Ultramicroscopy 159, 195–201 (2015). [PubMed: 25818366]
431. Fletcher C, Moody MP & Haley D Towards model-driven reconstruction in atom probe tomography. J. Phys. D. Appl. Phys. 53, 475303 (2020).
432. Beinke D et al. Extracting the shape of nanometric field emitters. Nanoscale 12, 2820–2832 (2020). [PubMed: 31961355]
433. Fleischmann C, Paredis K, Melkonyan D & Vandervorst W Revealing the 3-dimensional shape of atom probe tips by atomic force microscopy. Ultramicroscopy 194, 221–226 (2018). [PubMed: 30216823]

434. Haley D, Petersen T, Ringer SP & Smith GDW Atom probe trajectory mapping using experimental tip shape measurements. J. Microsc. 244, 170–180 (2011). [PubMed: 22004277]
435. Fletcher C, Moody MP & Haley D Fast modelling of field evaporation in atom probe tomography using level set methods. J. Phys. D Appl. Phys. 52, 435305 (2019).
436. Wei Y et al. Machine-learning-based atom probe crystallographic analysis. Ultramicroscopy 194, 15–24 (2018). [PubMed: 30036832]
437. Meisenkothen F, Samarov DV, Kalish I & Steel EB Exploring the accuracy of isotopic analyses in atom probe mass spectrometry. Ultramicroscopy 216, 113018 (2020). [PubMed: 32526558]
438. Madireddy S et al. Phase segmentation in atom-probe tomography using deep learning-based edge detection. Sci. Rep. 9, 1–10 (2019). [PubMed: 30626917]
439. Stintz A & Panitz JA Imaging atom-probe analysis of an aqueous interface. J. Vac. Sci. Technol. Vacuum Surf. Film. 9, 1365–1367 (1991).
440. Stintz A & Panitz JA Isothermal ramped field-desorption of water from metal-surfaces. J. Appl. Phys. 72, 741–745 (1992).
441. Pinkerton TD et al. Electric field effects in ionization of water-ice layers on platinum. Langmuir 15, 851–855 (1999).
442. Stuve EM Ionization of water in interfacial electric fields: an electrochemical view. Chem. Phys. Lett. 519–520, 1–17 (2012).
443. Adineh VR et al. Graphene-enhanced 3D chemical mapping of biological specimens at near-atomic resolution. Adv. Funct. Mater. 28, 1801439 (2018). This article reports a new approach to enable the analysis of biological samples by APT, discussing aspects of what the technique can bring.
444. Qiu S et al. Direct imaging of liquid–nanoparticle interfaces with atom probe tomography. J. Phys. Chem. C 124, 19389–19395 (2020).
445. Panitz JA In search of the chimera: molecular imaging in the atom-probe. Micros. Microanal. 11, 92–93 (2005).
446. Graham WR, Hutchinson F & Reed DA Field ion microscope images of DNA and other organic molecules. J. Appl. Phys. 44, 5155–5159 (1973).
447. Kim SH et al. Characterization of Pd and Pd@Au core-shell nanoparticles using atom probe tomography and field evaporation simulation. J. Alloy. Compd. 831, 154721 (2020).
448. Sha G et al. Segregation of solute elements at grain boundaries in an ultrafine grained Al–Zn–Mg–Cu alloy. Ultramicroscopy 111, 500–505 (2011). [PubMed: 21159437]
449. Kontis P et al. Atomic-scale grain boundary engineering to overcome hot-cracking in additively-manufactured superalloys. Acta Mater. 177, 209–221 (2019).
450. Zhao H et al. Segregation assisted grain boundary precipitation in a model Al–Zn–Mg–Cu alloy. Acta Mater. 156, 318–329 (2018).
451. Ashcroft N & Mermin D Solid State Physics (Thomson Learning, 1976).
452. Gault B, Moody MP, Cairney JM & Ringer SP Atom Probe Microscopy Vol. 160 (Springer, 2012).
453. Tsong TT Field penetration and band bending for semiconductor of simple geometries in high electric-fields. Surf. Sci. 81, 1–18 (1979).
454. Miller MK & Forbes RG Atom-Probe Tomography (Springer, 2014).
455. Many A, Goldstein Y & Grover NB Semiconductor Surfaces (North-Holland, 1965).
456. Mönch W Semiconductor Surfaces and Interfaces 2nd edn (Springer, 1995).
457. Cerezo A, Grovenor CRM & Smith GDW Pulsed laser atom probe analysis of GaAs and InAs. Appl. Phys. Lett. 46, 567 (1985).
458. Robins ES, Lee MJG & Langlois P Effect of optical diffraction on laser heating of a field emitter. Can. J. Phys. 64, 111 (1986).
459. Houard J, Vella A, Vurpillot F & Deconihout B Three-dimensional thermal response of a metal subwavelength tip under femtosecond laser illumination. Phys. Rev. B 84, 33405 (2011).
460. Sundaram SK & Mazur E Inducing and probing non-thermal transitions in semiconductors using femtosecond laser pulses. Nat. Mater. 1, 217–224 (2002). [PubMed: 12618781]

461. Tsong T Pulsed-laser-stimulated field ion emission from metal and semiconductor surfaces: a time-of-flight study of the formation of atomic, molecular, and cluster ions. Phys. Rev. B 30, 4946–4961 (1984).
462. Tsong TT & Liou Y Cluster-ion formation in pulsed-laser-stimulated field desorption of condensed materials. Phys. Rev. B 32, 4340–4357 (1985).
463. Cojocaru-Mirédin O et al. Characterization of grain boundaries in Cu(In,Ga)Se2 films using atom-probe tomography. IEEE J. Photovolt. 1, 207–212 (2011).
464. Cojocaru-Mirédin O, Choi P, Wuerz R & Raabe D Atomic-scale distribution of impurities in CuInSe2-based thin-film solar cells. Ultramicroscopy 111, 552–556 (2011). [PubMed: 21288643]
465. Blum I et al. Dissociation dynamics of molecular ions in high DC electric field. J. Phys. Chem. A 120, 3654–3662 (2016). [PubMed: 27136453]
466. Tsong TT & Cole MW Dissociation of compound ions in a high electric field: atomic tunneling, orientational, and isotope effects. Phys. Rev. B 35, 66 (1987).
467. Forbes RG Field evaporation theory: a review of basic ideas. Appl. Surf. Sci. 87–88, 1–11 (1995).
468. Vurpillot F, Houard J, Vella A & Deconihout B Thermal response of a field emitter subjected to ultra-fast laser illumination. J. Phys. D Appl. Phys. 42, 125502 (2009).
469. Cerezo A, Smith GDW & Clifton PH Measurement of temperature rises in the femtosecond laser pulsed three-dimensional atom probe. Appl. Phys. Lett. 88, 154103 (2006).
470. Sha G, Cerezo A & Smith GDW Field evaporation behavior during irradiation with picosecond laser pulses. Appl. Phys. Lett. 92, 43503 (2008).
471. Müller M, Gault B, Smith GDW & Grovenor CRM Accuracy of pulsed laser atom probe tomography for compound semiconductor analysis. J. Phys. Conf. Ser. 326, 12031 (2011).
472. Mazumder B, Vella a, Deconihout B & Al-Kassab T Evaporation mechanisms of MgO in laser assisted atom probe tomography. Ultramicroscopy 111, 571–575 (2011). [PubMed: 21159439]
473. Rice KP, Chen Y, Prosa TJ & Larson DJ Implementing transmission electron backscatter diffraction for atom probe tomography. Microsc. Microanal. 22, 583–588 (2016). [PubMed: 27329309]
474. Babinsky K, De Kloe R, Clemens H & Primig S A novel approach for site-specific atom probe specimen preparation by focused ion beam and transmission electron backscatter diffraction. Ultramicroscopy 144, 9–18 (2014). [PubMed: 24815026]
475. Breen AJ et al. Correlating atom probe crystallographic measurements with transmission Kikuchi diffraction data. Microsc. Microanal. 23, 279–290 (2017). [PubMed: 28288697]
476. Loberg B & Norden H Observations of the field-evaporation end form of tungsten. Ark. Fys. 39, 383–395 (1968).
477. Ceguerra AV, Breen AJ, Cairney JM, Ringer SP & Gorman BP Integrative atom probe tomography using scanning transmission electron microscopy-centric atom placement as a step toward atomic-scale tomography. Microsc. Microanal. 27, 140–148 (2021). [PubMed: 33468273]
478. Mouton I et al. Toward an accurate quantification in atom probe tomography reconstruction by correlative electron tomography approach on nanoporous materials. Ultramicroscopy 182, 112–117 (2017). [PubMed: 28668736]
479. Arslan I, Marquis EA, Homer M, Hekmaty MA & Bartelt NC Towards better 3-D reconstructions by combining electron tomography and atom-probe tomography. Ultramicroscopy 108, 1579–1585 (2008). [PubMed: 18620812]
480. Diercks DR & Gorman BP Self-consistent atom probe tomography reconstructions utilizing electron microscopy. Ultramicroscopy 195, 32–46 (2018). [PubMed: 30179773]
481. Costa GD et al. Advance in multi-hit detection and quantization in atom probe tomography. Rev. Sci. Instrum. 83, 123709 (2012). [PubMed: 23277998]
482. Peng Z et al. On the detection of multiple events in atom probe tomography. Ultramicroscopy 189, 54–60 (2018). [PubMed: 29614395]
483. Thuvander M, Kvist A, Johnson LJS, Weidow J & Andrén H-O Reduction of multiple hits in atom probe tomography. Ultramicroscopy 132, 81–85 (2013). [PubMed: 23294556]

484. Meisenkothen F, Steel EB, Prosa TJ, Henry KT & Prakash Kolli R Effects of detector dead-time on quantitative analyses involving boron and multi-hit detection events in atom probe tomography. Ultramicroscopy 159, 101–111 (2015). [PubMed: 26342554]

485. La Fontaine A et al. Interpreting atom probe data from chromium oxide scales. Ultramicroscopy 159, 354–359 (2015). [PubMed: 25796357]

486. Allegrini F, Wimmer-Schweingruber RF, Wurz P & Bochsler P Determination of low-energy ion-induced electron yields from thin carbon foils. Nucl. Instrum. Methods Phys. Res. Sect. B Beam Interact. Mater. At. 211, 487–494 (2003).

487. Ohkubo M, Shigetomo S, Ukibe M, Fujii G & Matsubayashi N Superconducting tunnel junction detectors for analytical sciences. IEEE Trans. Appl. Supercond. 24, 2400208 (2014).

488. Shiki S et al. Kinetic-energy-sensitive mass spectrometry for separation of different ions with the same m/z value. J. Mass. Spectrom. 43, 1686–1691 (2008). [PubMed: 18698555]

489. Keller H, Klingelhöfer G & Kankeleit E A position sensitive microchannelplate detector using a delay line readout anode. Nucl. Inst. Methods Phys. Res. A 258, 221–224 (1987).

490. Müller EW Field desorption. Phys. Rev. 102, 618–624 (1956).

491. Gomer R Field-emission, field-ionization, and field desorption. Surf. Sci. 299, 129–152 (1994).

492. Haydock R & Kingham DR Post-Ionization of field-evaporated Ions. Phys. Rev. Lett. 44, 1520–1523 (1980).

493. Forbes RG Field electron and ion emission from charged surfaces: a strategic historical review of theoretical concepts. Ultramicroscopy 95, 1–18 (2003). [PubMed: 12535541]

494. Neugebauer J & Scheffler M Theory of adsorption and desorption in high electric-fields. Surf. Sci. 287–288, 572–576 (1993).

495. Kreuzer HJ, Wang LC & Lang ND Self-consistent calculation of atomic adsorption on metals in high electric-fields. Phys. Rev. B 45, 12050–12055 (1992).

496. McMullen ER & Perdew JP Theory of field evaporation of the surface layer in jellium and other metals. Phys. Rev. B 36, 2598 (1987).

497. Schmidt WA, Ernst N & Suchorski Y Local electric-fields at individual atomic surface sites—field-ion appearance energy measurements. Appl. Surf. Sci. 67, 101–110 (1993).

498. Zanuttini D et al. Electronic structure and stability of the SiO^{2+} dications produced in tomographic atom probe experiments. J. Chem. Phys. 147, 164301 (2017). [PubMed: 29096513]

499. Zanuttini D et al. . Dissociation of GaN2+ and AlN2+ in APT: analysis of experimental measurements. J. Chem. Phys. 149, 134311 (2018). [PubMed: 30292204]

Box 1 |

Field evaporation of non-conductors

The main models of the field evaporation process were developed for metals. In a solid, the electric field is effectively screened by shifting the positive and negative charges (considered collectively) to generate an electric field of opposite direction to and the same magnitude as the external field. This is referred to as the Thomas–Fermi screening length and is typically in the range of <0.1 nm in metals, which is smaller than the interatomic distance and only atoms at the actual surface are subjected to the most intense field[451,452]. For semiconductor materials, this field penetration depth was found to be much larger than for metals (FIG. 2d). For example, Tsong[453] reported a depth of approximatively 2 nm in the near-surface layers of silicon. This is because the number density of electrons for semiconductors (10^{16} cm^{-3} (REF.[451])) is much lower than that for metals (10^{23} cm^{-3} (REF.[454])) and, as a result, the screening is weakened. The field penetrates into the semiconducting surface, causing the electron band structure to bend upwards, an effect known as band bending[455,456]. For insulators, these effects can be even more prominent as the penetration is deeper[61]. In addition, atom probe tomography (APT) using high-voltage pulsing was not typically leading to appropriate experimental conditions for analysing semiconducting and insulating materials[457], which became more routine with the implementation of laser pulsing capabilities. However, additional complexities arise from the interaction between the laser pulse and the electric field, in particular because the specimen has dimensions that are smaller or comparable in size with the illuminating wavelength, which makes its absorption properties non-trivial[34,458,459]. Compared with metals, the field evaporation of semiconductors must involve additional factors such as carrier diffusion, carrier recombination, thermal diffusion, field screening effect and band bending[459,460]. As the specimen is kept at a low temperature, some of these effects may be minimized.

The combination of a higher field evaporation temperature and a deeper penetration of the electrostatic field has consequences on the APT analysis. A deeper penetration of the field means that the bond-breaking between surface atoms will not take place exclusively for atoms on the topmost surface, but also slightly subsurface[461]. A larger population of atoms under a high electrostatic field means that not only the most protruding atoms can be field evaporated. This prevents controlled sequential removal of atoms, which lowers the spatial resolution[194]. This also facilitates the field evaporation of molecular ions[457,462]. The detection of a high proportion of molecular ions is common in compound semiconductors such as chalcogenides[463,464], nitrides[389] and oxides[465], but less often observed in monoatomic semiconductors such as silicon and germanium. Upon emission from the surface, these metastable molecular ions can undergo dissociative fragmentation[64,65,389,465,466] that can cause species-specific losses and degrade the spatial resolution[389].

Box 2 |

Practical considerations

The rate at which ions are emitted by the specimen is controlled both by the electric field and the temperature via an Arrhenius-type relationship[467]. To a first approximation, and in agreement with experiments[47], the electric field required to cause the emission of ions at a given rate φ varies linearly with temperature close to the zero-barrier evaporation field (summarized in the figure, part **a**). The region coloured blue corresponds to a continuous network of curves for increasing evaporation rates φ.

For a specific experiment, the user can set the base temperature, T_{base}, the direct current field, F_{DC}, and the desired rates at which ions are detected, which are directly related to the evaporation rate φ. These are the main experimental parameters that can be adjusted to control the field evaporation process. Let us assume a thought experiment performed in conditions corresponding to the large green circle. The pulsing mechanisms are such that either the field is temporarily increased at a constant temperature or the temperature is pulsed at a constant field. Both pulsing modes are now commonly available by using high-voltage or laser pulses, respectively[458,468,469].

An important difference between the pulsing modes is that the amplitude and duration of the thermal pulse depend on the geometry of the specimen and the thermophysical properties of the material[35,459,468]. This can affect the accuracy of the measured mass, that is, the mass peak width; see, for instance, the blue versus red mass peaks in the cartoon view of a typical section of a mass spectrum (see the figure, part **b**). Such differences in width can also be observed between an instrument with a straight flight path and one fitted with a reflectron (see Fig. 2). The spatial distribution of the thermal pulse across the specimen is also responsible for a change in the specimen's shape[470] that is associated with additional compositional inaccuracies[471,472].

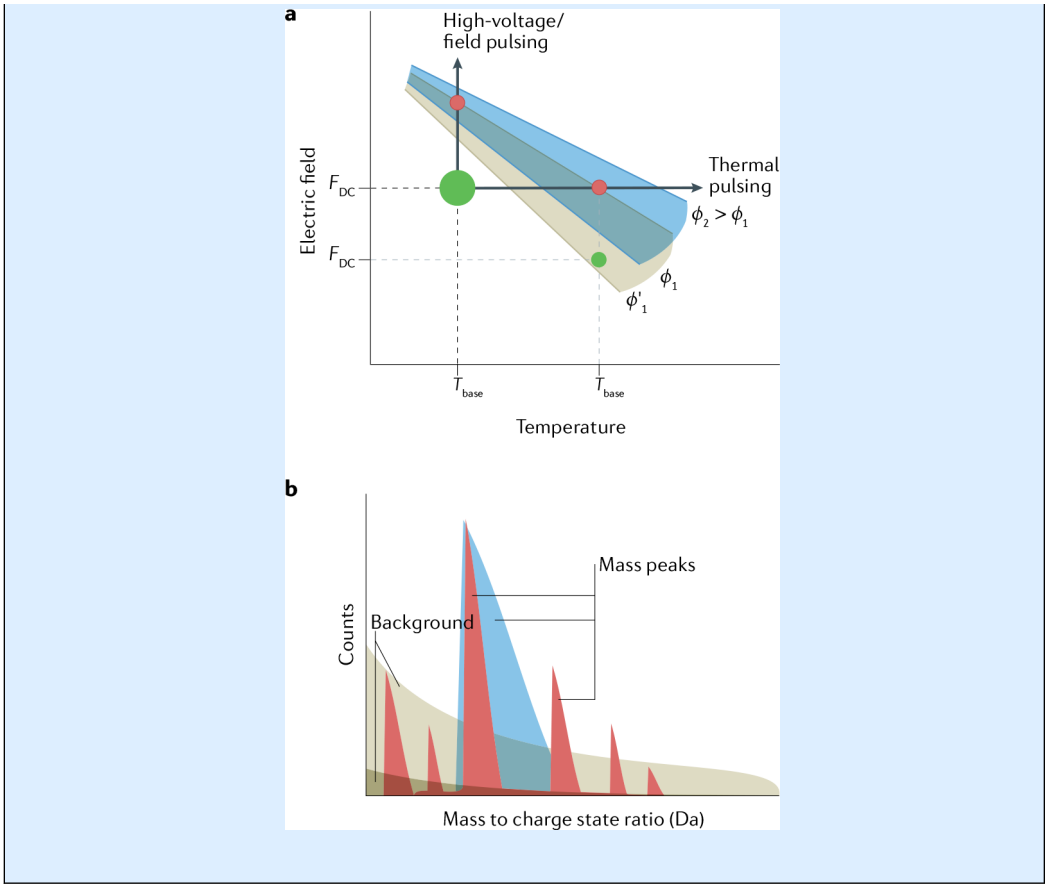

Box 3 |

Correlative microscopy

Common correlative microscopy experimental workflows involve ex situ experiments, using, for instance, X-rays, electron microscopes or scanning probe techniques. These often analyse a separate but representative sample of the same material, and then combine these data together in the interpretation of the material behaviour. Ongoing efforts aim to directly perform atom probe tomography (APT) on specimens analysed by other techniques in situ or nearly in situ, or use such techniques directly on an APT specimen.

Although limited in resolution, the scanning electron microscopy (SEM) part of focused ion beam (FIB)/SEM systems allows easy access, prior to the lift-out, to perform backscattered electron imaging, electron backscattered diffraction or electron-channelling contrast imaging to guide site-specific preparation. Transmission Kikuchi diffraction (TKD) to provide crystal orientation during or at the end of the specimen preparation has also become popular[223,473–475]. High-resolution SEM imaging can provide valuable information on the geometry of the final specimen[53], and more precise information can be gathered by using scanning transmission electron microscopy (TEM). The correlation of TEM with APT has long been undertaken[75,476,477], often to obtain information on the specimen's outer shape that is beneficial to guide the data reconstruction process. Nowadays, TEM is also used to obtain an accurate composition and atomic-scale crystallographic information from the same region of interest in the material under investigation.

The figure showcases the application of three different electron microscopy techniques to APT specimens. Note that the specimens were cleaned using low-voltage (2–5 kV) ion milling to remove the electron beam damage and carbon build-up prior to performing APT. The figure (see part **a**) shows the image quality (IQ) and colour map from TKD on specimens prepared from a grain boundary region in a chalcopyrite, a promising sulfide candidate material for solar cell applications[3]. The two grains are represented by two colours with different crystallographic orientations sharing a high-angle grain boundary (blue line) with a misorientation of 26.4° about the [110] direction. In the figure (part **b**), APT reveals co-segregation of sodium and carbon along the grain boundary. Nanoscale sodium-rich and carbon-rich clusters are also imaged. These segregations influence the local optoelectronic properties; hence, APT measurements are critical to establish structure–property relationships[224,226].

With respect to TEM, the figure (part **c**) shows a dark-field transmitted electron micrograph from a twinning diffraction spot, which highlights a twinned region in a needle specimen prepared from an $L1_0$-ordered ferromagnetic MnAl alloy[269,270]. The corresponding distribution of aluminium atoms from APT is shown (see the figure, part **d**), along with a set of the iso-surfaces. A two-dimensional (2D) compositional map further shows the manganese segregation confined to the twin boundary and depletion outside the twinned region. These segregations and twinned structure are expected to directly influence the local magnetic domain structure.

Finally, a bright-field image of a needle specimen from a creep-deformed CoNi-based superalloy is displayed (see the figure, part **e**). The dark contrast indicates the presence of stacking faults. A high-resolution, high-angle, annular dark-field image from the stacking fault region reveals a change in atomic structure at the fault with respect to the surrounding lattice[5]. The figure (see part **f**) shows the corresponding distribution of cobalt and a confined linear region highlighted by an iso-surface highlighting segregation of chromium to a partial dislocation[261]. The 2D elemental composition map of aluminium (atomic per cent) further shows a confined depletion of aluminium along a plane that terminates exactly at the partial dislocation. This plane corresponds to the SF plane, which is chemically distinct from the associated partial dislocation. The compositional profiles along the SF plane indicate an in-plane diffusion mechanism.

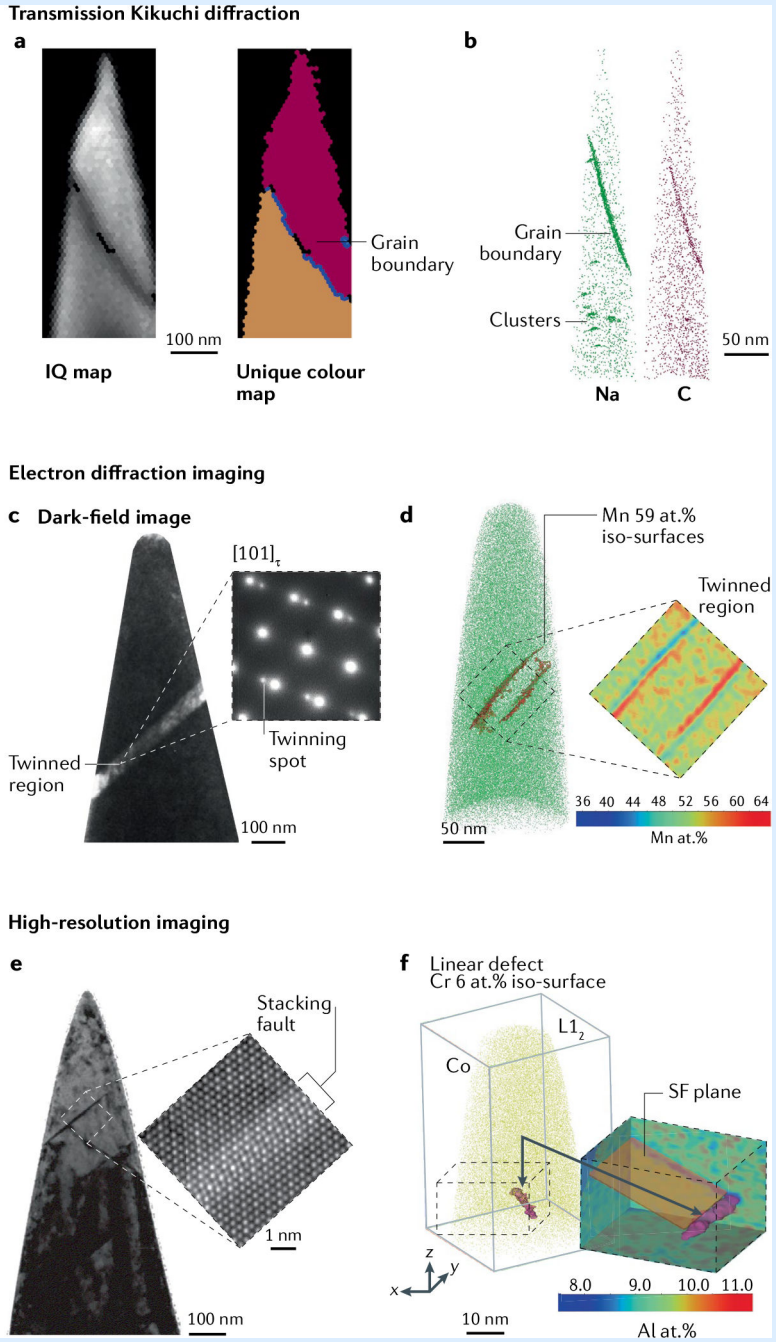

Part **f** adapted with permission from REF.[261], Elsevier.

Box 4 |

Calibration

Numerous parameters involved in the reconstruction process, such as the image compression factor, ξ, are required to further refine the spatial accuracy of the image. In many cases, this optimization of reconstruction parameters is grounded by ensuring that the reconstruction accurately reflects one or more known physical prominent characteristic of the specimen across a range of length scales. This includes partial crystallographic information such as lattice planes that are sometimes available in the reconstructed data[142], as shown in FIG. 6. It also includes specific microstructural features such as interfaces or precipitates, the morphology of which has been previously confirmed by complementary or correlative electron microscopy[478,479] (see BOX 3) or the overall shape of the specimen before and/or after the atom probe tomography (APT) experiment, usually measured by electron microscopy[434,480]. Other approaches, for example atomic force microscopy, have also been used[433]. Not all of these approaches are applicable in every instance, and each has their own strengths and limitations.

Box 5 |

Limitations to species detection

There are several factors that can limit the detection of a species. First, there is a certain level of background, as shown in BOX 3 (see the figure, part **b**, red or green). This background is related to the dark current of the microchannel plates that leads to a few counts per second per square centimetre. Additionally, ions can be created at the electrostatic field and not correlated to a time pulse, either resulting from field ionization of residual gas atoms or field emitted from the specimen's surface, as illustrated in BOX 3 (see the figure, part **a** and associated discussion). These uncorrelated counts form a random uniform background in the time-of-flight spectrum. Owing to the conversion from time of flight into mass to charge, this appears as a decaying signal in the mass spectrum, with the background at lower masses relatively more prominent than that at higher masses. The level of background depends on the analysis conditions such as vacuum level, intensity of the electrostatic field and so on.

Second, the number of peaks for a specific element depends on its isotopic distribution and the different charge states in which it is detected, and hence on its ionization energies and on the analysis conditions. The width of the peaks is related to the precision of the measurement of the time of flight, voltage and flight distance, but also to the precision of the spread in the energy of the ions in voltage pulsing mode or of delays in the time the ion forms during the pulse in laser pulsing mode. The latter effect significantly depends on the specimen geometry and thermal conductivity[459,468].

Third, the single-particle detector is imperfect. In principle, it is operated in a mode where incoming ions of all energies above a certain threshold (typically 2 keV) will trigger a signal of similar amplitude. This enables the detection of light and heavy ions with the same efficiency and, as the microchannel plates have a limited open area (approximately 50–90%), the probability to detect an ion depends only on where it lands on the detector. Yet these settings make it impossible to use the current generation of detectors for assessing charge states, which causes overlap between ions of different elements but with the same mass to charge ratio, for example, $^{14}N^{+}$ and $^{28}Si^{2+}$, $^{27}Al^{+}$ and $^{54}Fe^{2+}$, $^{14}N_2{}^{+}$,$^{28}Si^{+}$, $^{56}Fe^{2+}$ and so on. In measurement of the composition, these overlaps can be deconvoluted based on the relative isotopic abundances[136], but the specific position of ions of each species with the same mass to charge ratio cannot be determined.

In addition, if in theory the efficiency is not dependent on the element, some elements are more prone to be detected as part of multiple events[57]. This makes their loss more likely owing to pile-up effects — two ions with very close times of flight land nearly at the same detector position, making it impossible for the second ion to trigger a signal high enough to be detected. This occurrence is, in part, caused by the response time of the microchannel plates, but also by the processing of the electric signals of the delay-line detector[44,481]. Additional losses can originate from the dissociation of molecular ions that lead to the formation of low-energy ions or neutral atoms or molecules. Depending on where the dissociative event occurs along the ion flight, the daughter ions may

not be accelerated sufficiently to trigger a detectable signal[389]. Daughter ions may not acquire the energy that is necessary to make the time of flight of these ions close enough to other ions from the same species, making it impossible to associate them with a specific range. These aspects are typically revealed using Saxey's approach of a correlation histogram[58]. Species-specific losses have been well documented in the case of carbon[60,482,483], boron[219,484], nitrogen[68,389] and oxygen[65,465,485], for instance.

These aspects make the balancing act between peak height and background level rather subtle. Numerous statistical criteria can be used to assess whether a detected peak is statistically significantly above the level of background, locally in a range of mass to charge ratios. The best thought-through criteria have been introduced in REFS[23,366.] Estimates of the sensitivity will vary from analysis to analysis and from element to element, but those reported in the literature are typically in the range of atomic parts per million[41,366].

Box 6 |

Advances in atom probe detectors

The demands on an atom probe detector are stringent, and further developments will be required to demonstrate fast read-out speed, sufficient field of view and reliable discrimination of multiple hits and isobaric overlaps. Different approaches are currently under investigation to solve or improve these problems. For example, Bacchi et al.[416] used secondary electron generation by ions crossing a thin carbon foil of 20 μm (REF.[486]) to generate a kinetic energy proportional signal. By carefully monitoring the signal amplitude generated by the electron cloud impinging on the subsequent microchannel plate, the system was able to distinguish overlapping signals at 32 Da in the case of zinc and oxygen. A second approach pursued by the company Steam Instruments was to adapt a superconducting detector to the requirements of atom probe tomography (APT)[487,488]. The concept behind a superconducting detector is rather similar to a delay-line detector[489]. The detector is cooled such that electrons are coupled in Cooper pairs, which underpin superconductivity in solids. The localized heating associated with the impact of the ions emitted by the APT specimen can break these pairs and generate electrons that are collected at the end of the delay line. These approaches bear great potential to reach 100% detection efficiency, even if substantial technical obstacles must still be solved to increase the surface area and lower dead time, which is the time during which the detector is not operational following the detection of one or more ions.

Box 7 |

Theory

Beyond new models for field ion microscopy (FIM) contrast interpretation, new forays are being made in the theoretical understanding of the field evaporation process. An aspect of experimental sciences that can sometimes get overlooked is their underpinning theoretical aspects. This is particularly true in atom probe tomography (APT). Field evaporation mechanisms were theorized early[45,490,491] with some advances in the following decades[46,467,492,493], but focused almost exclusively on metals, whereas the field has now fast expanded into the analysis of non-conductors. Although numerical simulations have been conducted to better understand some of the artefacts observed in APT[382], the simulations are concerned with the ion trajectories rather than the field evaporation process itself.

Ab initio calculations have been proposed as a tool to study field evaporation effects[65,494–496], and there are current efforts to revive this activity. The initial forays are very promising with true modelling of the field evaporation process[384], including the small roll-up-type motion that had been predicted and confirmed experimentally[497]. In combination with molecular dynamics, ab initio approaches have also been used to estimate the stability of molecular ions[288,389] and complete energetics during ion flight to identify dissociation channels under the influence of the electrostatic field[59,65,498,499].

Much theory remains to be developed, in particular in connection with experimental observations. This handshake is crucial to guide the optimization of the experimental conditions in order to maximize data quality. As already mentioned, the ideal APT detector would detect all ions, yet as long as low-energy neutrals atoms and molecules originating from the dissociations of molecular ions are created, there will be species-specific losses that make reconstructing 100% of the data impossible. Better predictions of the stability of field-evaporated species are necessary, and so are, for instance, insights into surface migrations and roll-ups that limit the spatial resolution.

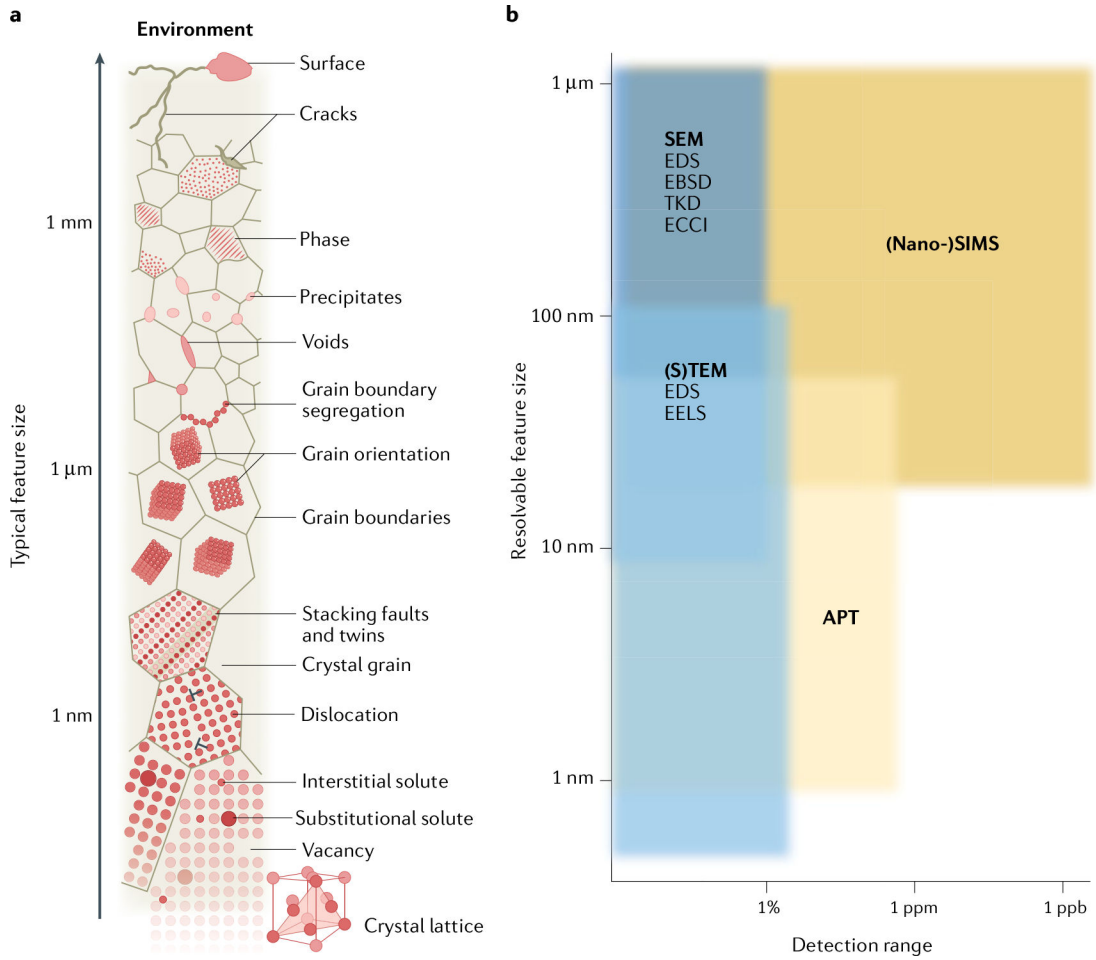

Fig. 1 |. Microstructural features with their typical size and some analytical techniques used to analyse them.

a | Typical microstructural features of an engineering material, from the atomic arrangement of a crystal lattice, through a range of crystalline defects, phases and grains, to imperfections at the surface. The presence and quantification of hydrogen, specifically at these features, is a crucial challenge. **b** | Sensitivity and analysable feature size for some materials analysis techniques. APT, atom probe tomography; EBSD, electron backscattered diffraction; ECCI, electron-channelling contrast imaging; EDS, energy-dispersive X-ray spectroscopy; EELS, electron energy loss spectroscopy; SEM, scanning electron microscopy; SIMS, secondary ion mass spectrometry; (S)TEM, (scanning) transmission electron microscopy; TKD, transmission Kikuchi diffraction. Part **a** modified from J. Duarte, Max-Planck-Institut für Eisenforschung (MPIE).

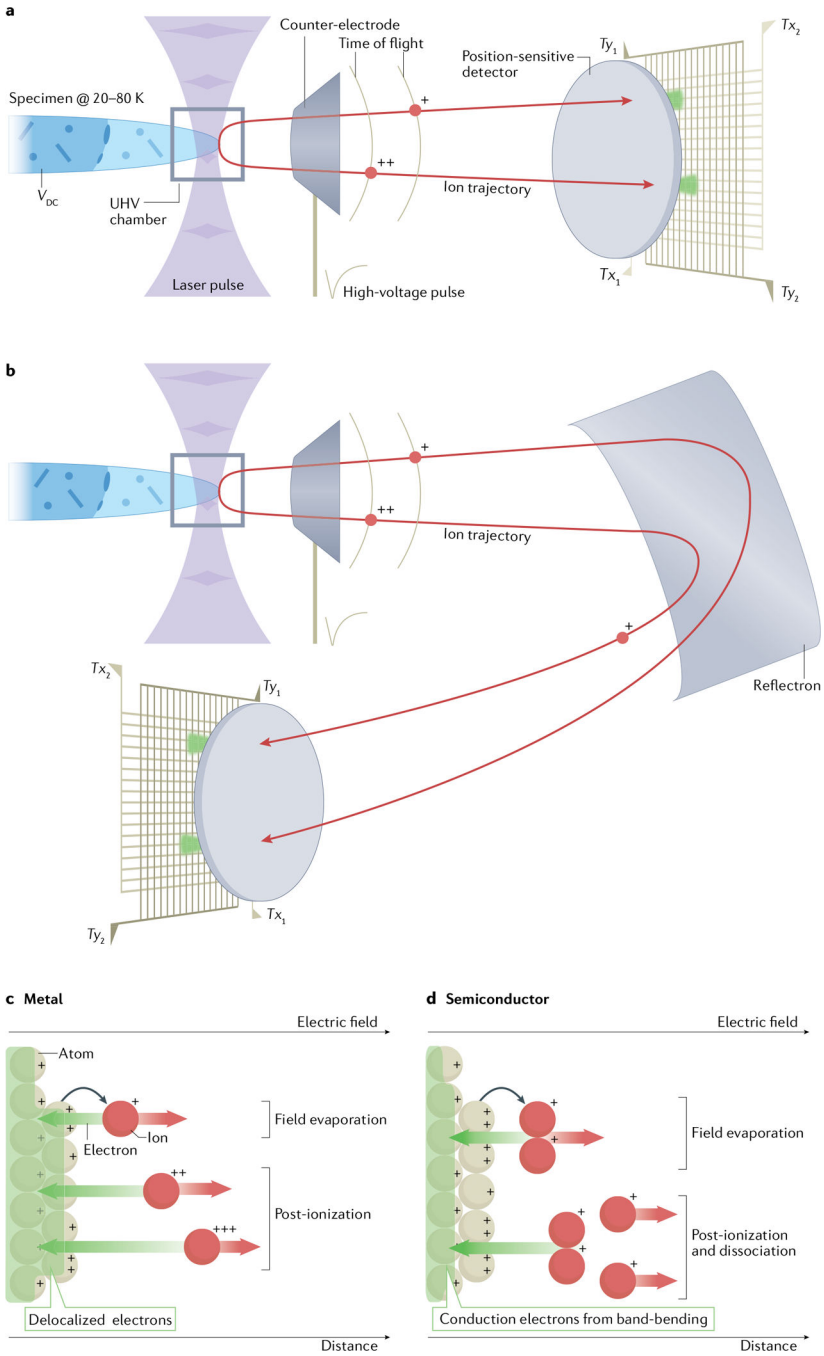

Fig. 2 |. Schematics of the atom probe instrumentation and the field evaporation process. **a**,**b** | View, not to scale, inside an atom probe ultra-high vacuum (UHV) analysis chamber in a straight flight-path instrument (part **a**) and a reflectron-fitted instrument (part **b**). **c**,**d** | Field evaporation and post-ionization/dissociation processes in the case of a metal (part **c**) and less-conducting material (part **d**). Tx and Ty, times obtained from the delay-line detector used to retrieve the ion impact position; V_{DC}, applied standing voltage.

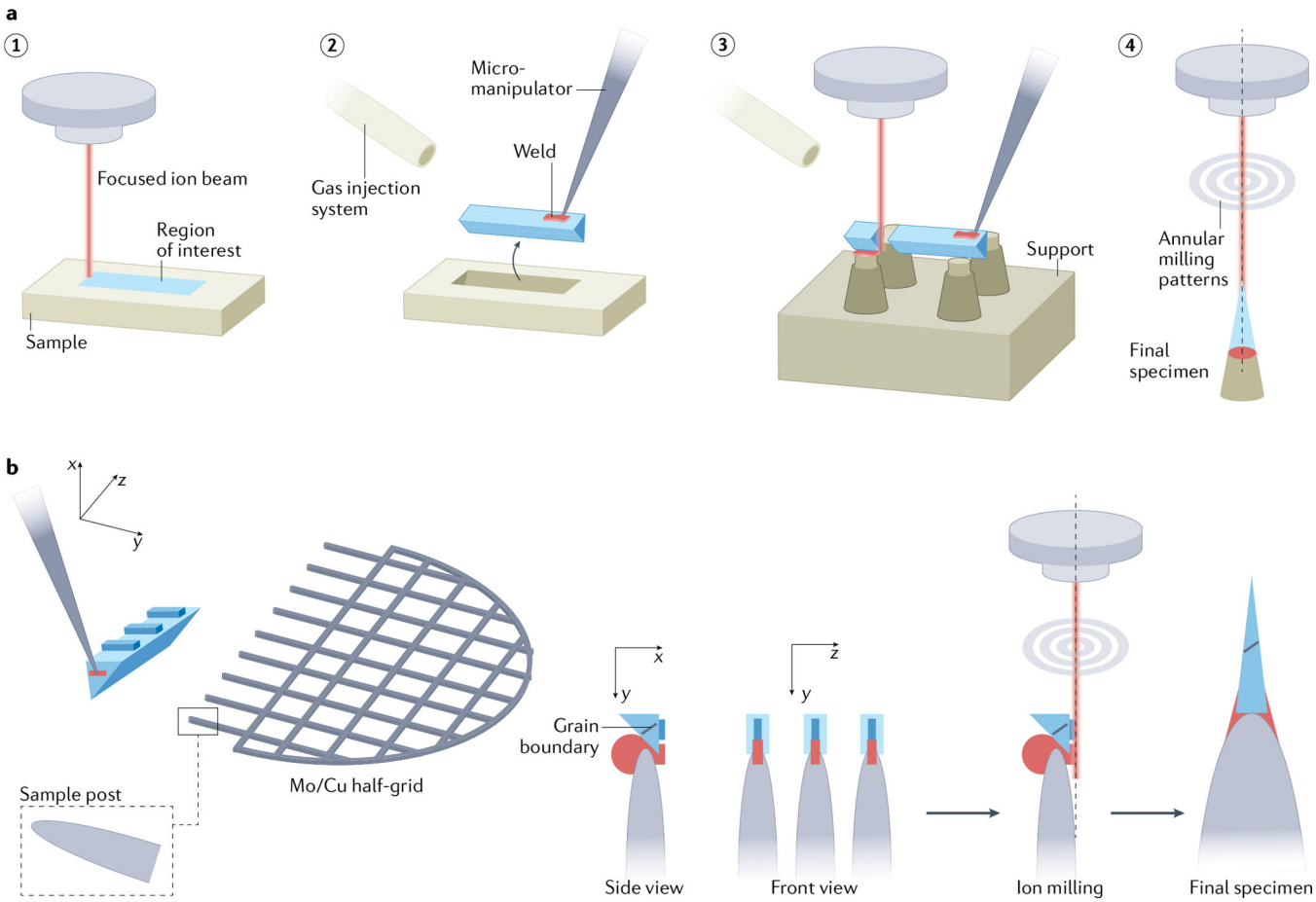

Fig. 3 |. FIB lift-out specimen preparation.

a | Four-step protocol for focused ion beam (FIB) lift-out specimen preparation, with the specimen deposited on a support. **b** | Protocol adapted for in-plane lift-out of targeted features to facilitate correlative analysis by transmission electron microscopy (TEM).

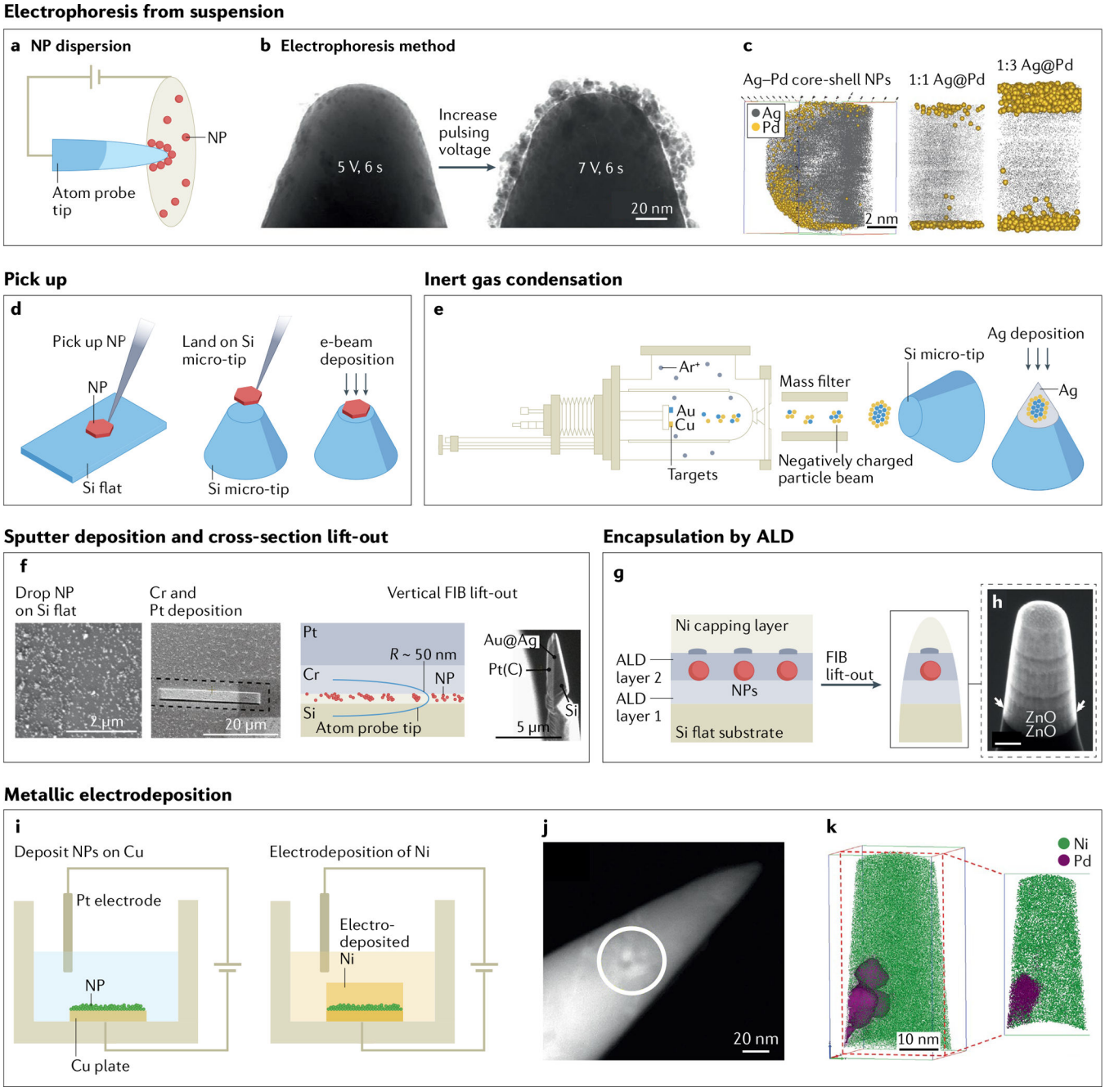

Fig. 4 |. Specimen preparation techniques for non-bulk samples.

a | Electrophoresis of nanoparticles (NPs) on a pre-electropolished platinum–rhenium needle. **b** | Transmission electron microscopy (TEM) images showing two layers of NPs deposited by increasing the pulsed voltage from 5V to 7V for 6 s. **c** | Atom probe tomography (APT) of silver (core)–palladium (shell) NPs with 1:1 and 1:3 ratios[92]. **d** | NP picked up by the micromanipulator, deposited on a silicon micro-tip and protected by electron-beam-assisted deposition[101]. **e** | Inert gas condensation formation and deposition of gold–copper NPs on silicon micro-tips, followed by metal film deposition and focused ion beam (FIB) milling[106]. **f** | Diluted NP solution dropped on a scanning electron

microscopy (SEM) stub and then covered by chromium film and electron-beam-assisted deposited platinum, and a rotated image of the wedge[89]. **g** | NPs encapsulated using atomic layer deposition (ALD), followed by FIB lift-out. **h** | TEM image of an APT specimen containing platinum NPs sandwiched between atomically deposited layers of ZnO[115]. **i** | Electrophoresis of NPs on a copper plate and electrodeposition of nickel (insets are the copper plate after electrophoresis and electrodeposition, respectively). **j,k** | TEM image of the APT specimen reveals palladium NPs (dotted circle) capped in the nickel matrix (part **j**) and corresponding APT analysis (part **k**)[447]. Parts **b** and **c** reprinted from REF.[92], Springer Nature Limited. Part **d** adapted from REF.[101], CC BY 4.0 (https://creativecommons.org/licenses/by/4.0/). Part **e** adapted with permission from REF.[106], ACS. Part **f** adapted with permission from REF.[89], Elsevier. Part **h** adapted with permission from REF.[115], Elsevier. Parts **j** and **k** adapted with permission from REF.[447], Elsevier.

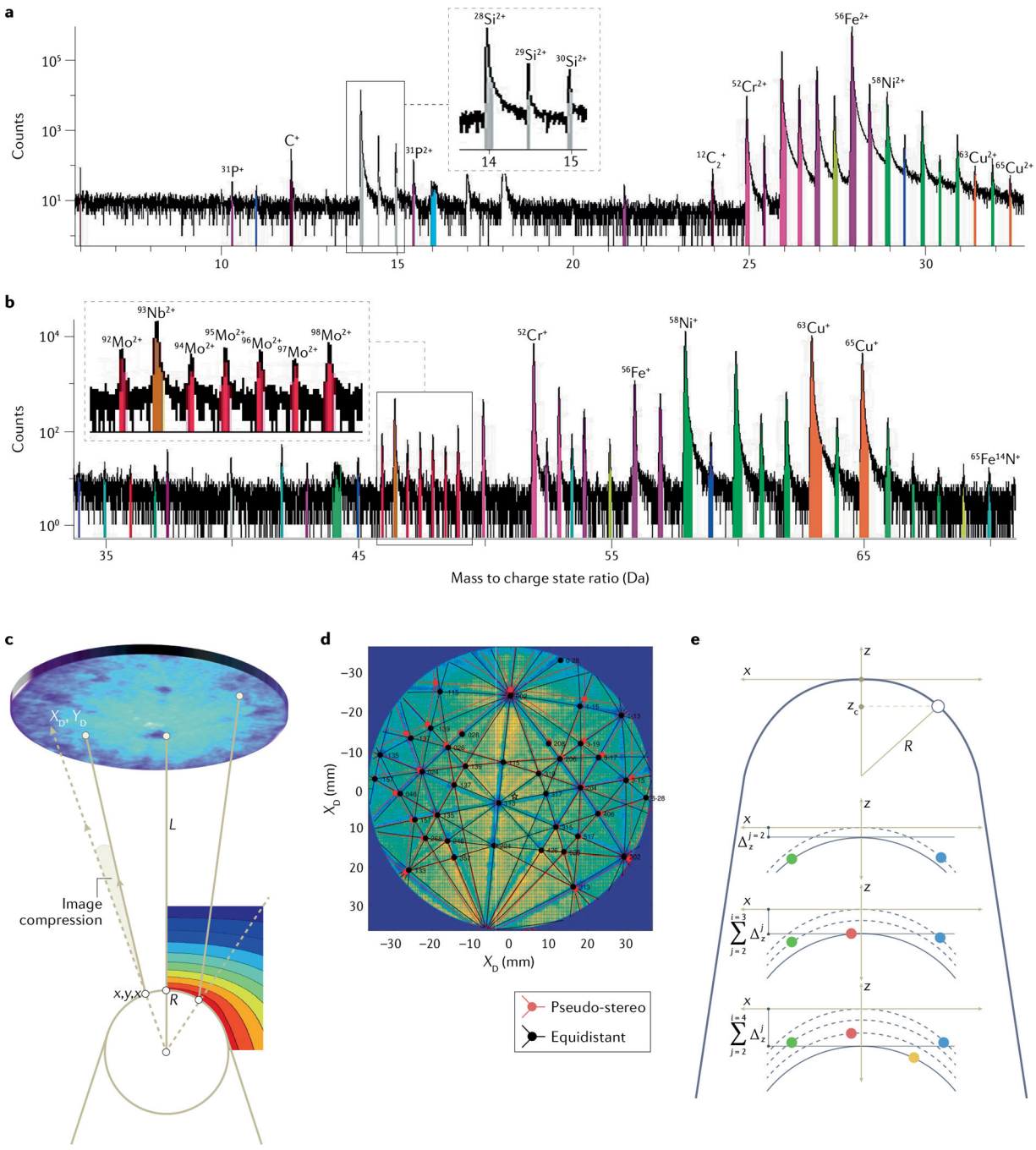

Fig. 5 |. Ranged mass spectrum and reconstruction protocol.

a,**b** | Segments of an atom probe tomography (APT) mass spectrum from the analysis of a 17–4PH steel sample. Mass spectrum highlights the detection of different charge states, resolution of elemental isotopes and field evaporation of molecular ions. **c** | Schematic of ion projection from the specimen to detector in a straight flight-path atom probe instrument. Colour map corresponds to typical iso-potential estimated from two-dimensional (2D) finite element methods calculations, used as an illustration. **d** | Comparison between projection models on an experimental pure-aluminium data set. **e** | Schematic of procedure

to reconstruct real-space depth, that is z coordinate, from top to bottom: detected ion assumed to be projected from a hemispherical surface, and for each subsequently detected ion an additional increment is added to the z-coordinate calculation to account for all preceding ions. L, distance to detector; R, specimen radius; X_D, Y_D, detector coordinates. Parts **a** and **b** data courtesy of G. Yeli. Part **d** adapted with permission from REF.[139], Cambridge University Press.

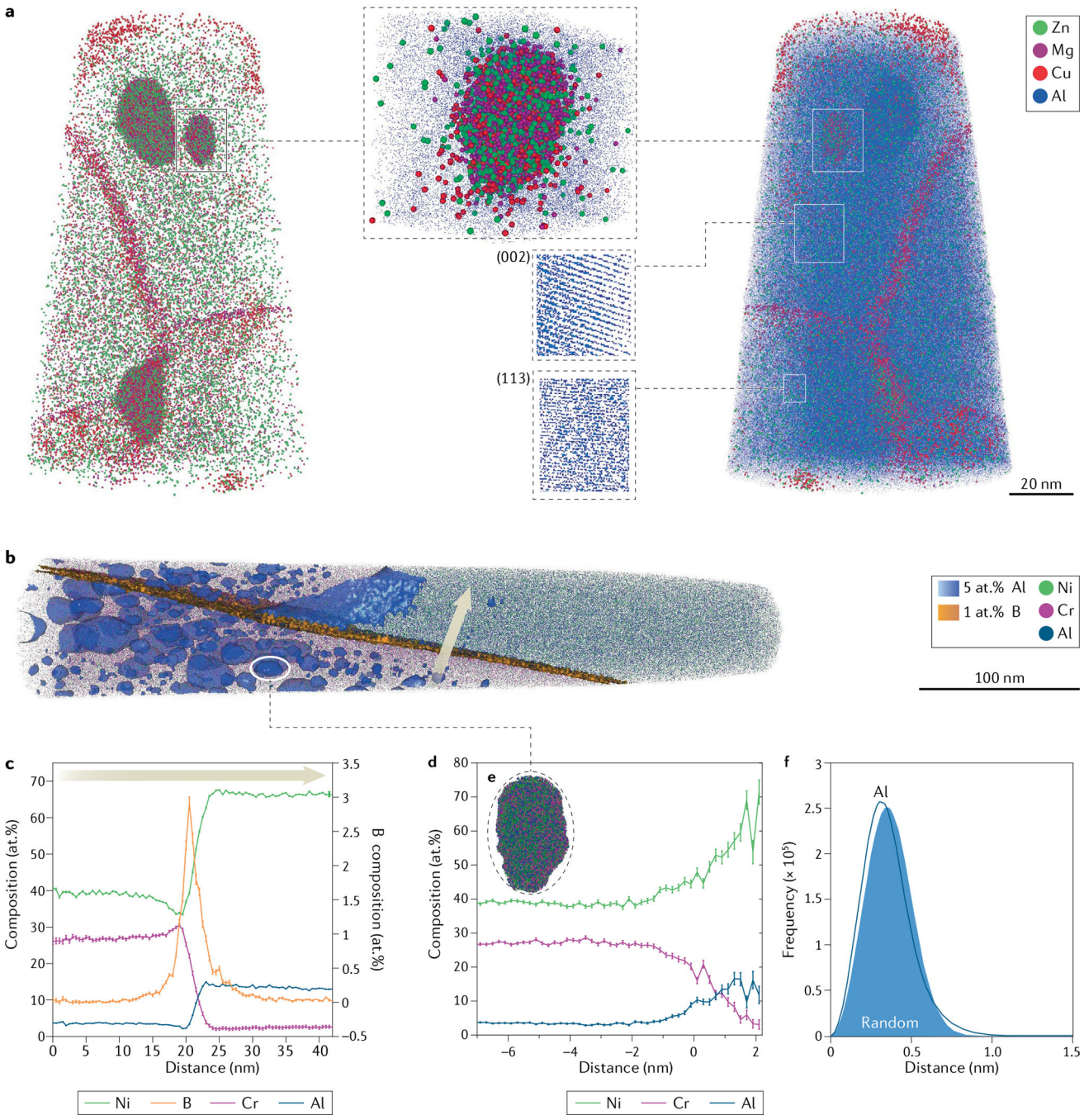

Fig. 6 |. Examples of reconstruction and data visualization and analysis from engineering alloys.

a | Reconstructed point cloud showing elemental distribution within a nanocrystalline aluminium alloy containing both precipitates and segregation of solutes to the grain boundaries[448], with close-ups of a single precipitate and different families of atomic planes. **b**–**f** | Reconstruction and analysis from an additively manufactured nickel-based alloy[449]: point cloud and iso-concentration surfaces highlighting the interfaces between γ and γ' phases (blue) and a grain boundary where boron strongly segregates (orange) (part **b**); composition in a cylinder 20 nm in diameter across the grain boundary calculated along the

beige arrow, enabling quantification of boron segregation and γ and γ' phase compositions (part **c**); individual γ' precipitate isolated from within the point cloud, highlighted by the beige ellipse in part **b** (part **d**); composition profile in the form of a proximity histogram from the iso-surface delineating the precipitate shown in part **d** (part **e**); and first nearest-neighbour distribution for aluminium showing a deviation from the random distribution indicative of the clustering/precipitation tendency readily visible from the atom map (part **f**).

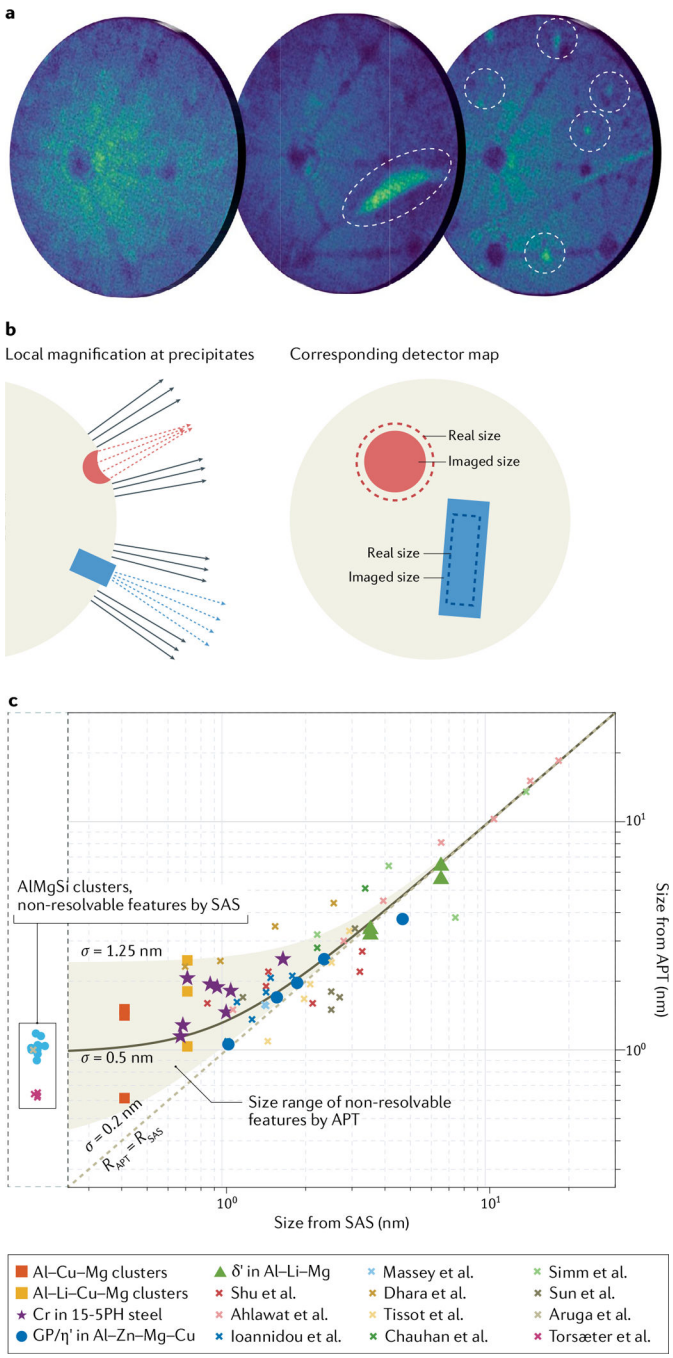

Fig. 7 |. Spatial resolution of APT in the analysis of precipitates.

a | Successive detection ion maps obtained for 10^6 detected ions during analysis of a model 7XXX-series aluminium alloy; more details on materials can be found in REF.[450]. **b** | Schematic view of compression or divergence of trajectories associated with the presence of precipitates, and associated imaging error. **c** | Size of precipitates reported by atom probe tomography (APT) versus small-angle scattering (SAS), highlighting the presence of an effective spatial resolution limit below which microstructural features are detected but their size and composition can no longer be directly accurately measured. For the references

in part **c**, please refer to REF.[1]. *R*, specimen radius; σ_i, precision. Part **c** adapted with permission from REF.[1], Elsevier.